PRODUCTION OF INJECTION MOLDING TOOLING WITH CONFORMAL COOLING CHANNELS USING THE THREE DIMENSIONAL PRINTING PROCESS

by

EDWARD M. WYLONIS, III

B.S., Mechanical Engineering
Massachusetts Institute of Technology, 1993

Submitted to the Department of Mechanical Engineering
in Partial Fulfillment of the
Requirements for the Degree of

MASTER OF SCIENCE

at the

Massachusetts Institute of Technology

May 1995

Signature of Author . . . .
Department of Mechanical Engineering
May 23, 1995

Certified by . . . .
Emanuel M. Sachs
Associate Professor of Mechanical Engineering
Thesis Supervisor

Accepted by . . . .
Ain A. Sonin
Chairman, Graduate Committee

PRODUCTION OF INJECTION MOLDING TOOLING WITH CONFORMAL COOLING CHANNELS USING THE THREE DIMENSIONAL PRINTING PROCESS

by

Edward M. Wylonis III

Submitted to the Department of Mechanical Engineering
on May 23, 1995, in partial fulfillment of the
requirements for the Degree of Master of Science

Abstract

Three Dimensional Printing is a desktop manufacturing process in which powdered materials are deposited in layers and selectively joined with binder from an ink-jet style printhead. Unbound powder is removed upon process completion, leaving a three dimensional part. Stainless steel injection molding inserts have been created from metal powder with the 3DP process.

The freedom to create internal geometry by the use of the 3D-Printing process allows for the fabrication of molds with complex internal cooling passages. Tooling was developed with cooling channels designed to be conformal to the molding cavity. A finite difference simulation was constructed to study conformal channel design.

A direct comparison of the mold surface temperature during the injection cycle of a 3D Printed mold with conformal channels and a mold machined with conventional straight channels was completed. The conformal passages produced with the 3DP process provide the ability to accurately control the temperature of the molding cavity throughout the process cycle. Surface temperature measurements demonstrated that the inserts with conformal cooling channels exhibited a more uniform surface temperature than the inserts machined with straight channels.

The molding cavity surface temperature of the 3D Printed core insert with conformal channels is more uniform than the surface temperature of the core insert with straight channels. At the beginning of the cooling stage of the cycle there is a 4 °C variation in temperature along the mold surface of the 3D Printed core insert. This compares to a 7 °C temperature variation for the core insert machined with conventional straight channels. The mold surface temperature was measured over approximately 30 cycles. An upward drift in the initial mold surface temperature in each cycle throughout the injection molding run was observed using the inserts with straight channels. The magnitude of this drift reached as high as 30 °C. No drift was observed using the 3D Printed inserts with conformal cooling channels.

Issues such as powder removal and post processing of green parts with small cooling channels were also investigated.

Thesis Supervisor: Dr. Emanuel Sachs
Title: Associate Professor of Mechanical Engineering

Dedication

To my family
for all of their love and support.

Acknowledgments

The National Science Foundation under the Strategic Manufacturing Initiative (contract number 9215728-DDM), the Technology Re-Investment Project, Cooperative Agreement (DMI - 9420964) and the members of the Three Dimensional Printing Industrial Consortium have supported the project with valuable suggestions and resources.

I would like to acknowledge the support of the staff and students in the 3D Printing project:

> Ely Sachs for believing in my abilities and giving me the opportunity, encouragement and direction to develop as a researcher.
>
> Professors Michael Cima and Samuel Allen for various insightful and helpful suggestions.
>
> Steve Michaels, thanks for always answering my seemingly endless barrage of questions and giving me suggestions on new research paths to follow.
>
> Earl Sun, thanks for being a great friend and co-researcher.
>
> Thank you, Chris Shutts, Gail Thornton, Tara Arthur, Hon Tang, Honglin Guo, Jain Charnnarong, Dave Brancazio, Jim Serdy, Mike Rynerson, Alain Curodeau, Tailin Fan, John Lee and Jim Bredt for your friendship and for going out of your way to help me.

Specific work incorporated in this thesis:

> Earl Sun is responsible for half of the work associated with insert - mold assembly design and machining, determination of the thermal conductivity of 3D Printed bronze infiltrated 316L stainless steel material and work done on the characterization of the part distortion.
>
> Jim Serdy and Dave Brancazio are responsible for the 3D Printing of large tooling inserts.
>
> Jim Beals of UTRC executed many furnace runs that eventually led to the successful infiltration of the final 3D Printed tooling.

I appreciate the support of the staffs of the machine shop and administrative offices at the Lab for Manufacturing and Productivity. Thank you Fred Cote, Gerry Wentworth, Bob Kane and Kevin Baron for helping me with various machining projects and problems.

Contents

List of Figures

List of Tables

Introduction

1.1 Motivation

The injection molding process is one of the most widely used methods of manufacturing polymer plastic products. It is estimated that in the U.S. alone consumption of injection-molded polyethylene, polypropylene and polystyrene will rise to 11 billion pounds by 1997 [School, 1994]. The products of injection molding are many and varied and range from tiny gears and buttons to large automotive parts.

Many parts that are injection molded today have very rigid tolerance requirements. There is an ever increasing demand for a high quality product. Attempts have been made in recent years to employ the injection molding process in manufacturing optical parts such as compact disks and camera lenses. This sort of venture requires the molding of a part with little or no residual stress.

Proper thermal management of metal injection molding tooling is necessary to increase part quality and production rates. Cooling passages placed in the tooling manage the heat flow out of the plastic. Current fabrication methods place severe limitations on the configuration of the cooling channels used for heat withdrawal.

The freedom to create internal geometry by the use of the 3D-Printing process allows for the fabrication of molds with complex internal cooling passages. These cooling channels can be designed to be conformal to the molding cavity. Conformal passages produced with the 3DP process provide the ability to control more accurately the temperature of the molding cavity throughout the process cycle. Such temperature control has the potential to produce parts with lower residual stresses and to shorten cycle times.

1.2 Fundamentals of Injection Molding

Injection molding is a cyclic process in which a heat-softened material is forced under pressure into a mold. Solidification occurs in the mold causing the material to retain the shape of the cavity. The mold is then opened, the part is ejected and the process is repeated. Although the term injection molding is most often used referring to thermoplastic injection molding, thermosetting materials and ceramic materials with thermoplastic binder can also be processed by injection molding. Throughout this thesis thermoplastic injection molding will be discussed even though many of the concepts presented apply not only to injection molding of other materials but also to many other molding processes such as blow molding and casting.

The most common type of injection molding machine in use today is the reciprocating screw type shown in Figure 1.1. An injection molding process is characterized by four successive stages: plastication, injection of molten polymer, packing, and part cooling. During plastication, polymer pellets are fed by gravity from the hopper to the screw and pushed through the barrel toward the nozzle by the rotating screw. As the plastic is transported along the barrel, heat is generated from the shear work done on the material and heat is conducted into the material from electric heater bands which surround the barrel. The combination of the heat conduction and the heat generation causes the polymer material to melt as it moves along the screw. The screw moves back due to the accumulation of plasticated material in front of the screw until a limit switch is tripped. At this point plastication is complete and the screw stops turning. During injection the screw is pushed forward by a hydraulic ram and the molten polymer is pushed into the mold cavity. A non-return valve near the screw tip limits the polymer back flow so that the screw effectively becomes a plunger. After the mold cavity is filled, continued pressure on the hydraulic ram forces more polymer into the cavity during the packing stage. As the molten polymer in the cavity is trapped due to freezing of the polymer at the mold gate, the screw begins turning, preparing the molten polymer for the next shot while the molten polymer in the cavity solidifies to the shape of the cavity. The mold opens after solidification and the part is ejected. When the mold closes the next injection cycle begins. [Injection molding summary courtesy Byung Hoon Kim]

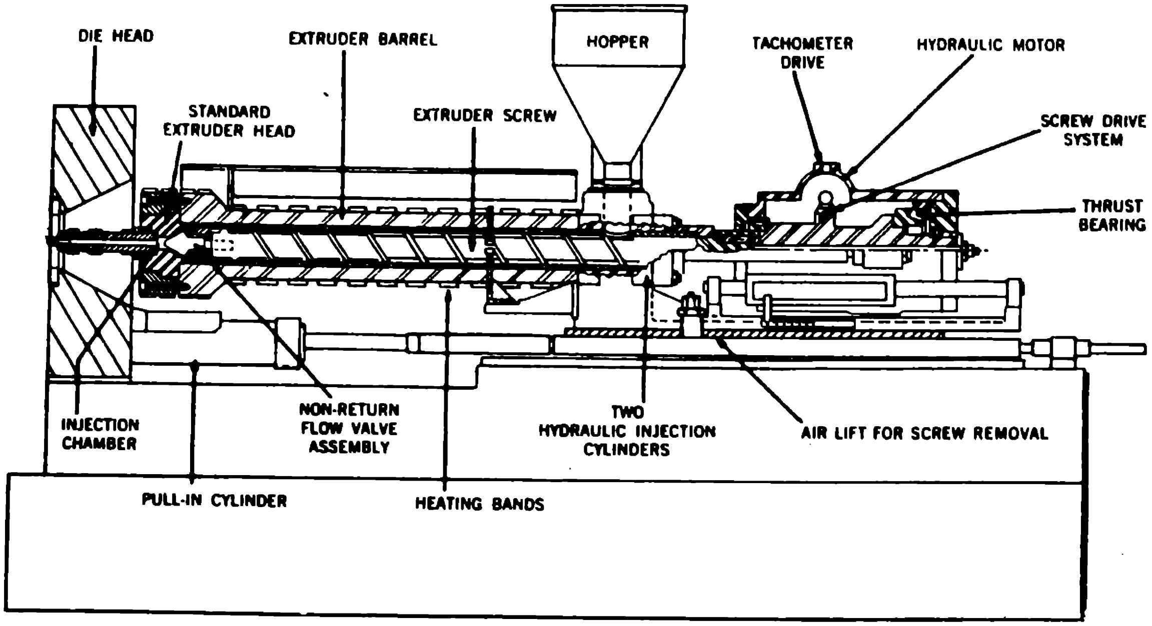

Figure 1.1: Schematic drawing of the injection end of a reciprocating screw machine. (Courtesy Rubin, 1972 and the Van Nostrand Reinhold Company)

1.3 Three Dimensional Printing - Application to Injection Molding Tooling

Three Dimensional Printing (3DP) is a process for the rapid fabrication of three dimensional parts directly from computer models [Sachs et al, 1990]. A solid object is created by printing a sequence of two-dimensional layers. The creation of each layer involves the spreading of a thin layer of powdered material followed by the selective joining of powder in the layer by ink-jet printing of a binder material. A continuous-jet printhead is raster scanned over each layer of powder using a computer controlled stepper motor driven x-y table. Individual lines are stitched together to form 2D layers, and the layers are stitched together to form a 3D part. The printing nozzle has a circular opening 46 μm in diameter. The nozzle is stimulated by a piezoelectric transducer vibrating at 60 kHz to break the stream into droplets 80 μm in diameter. Commands to modulate the binder stream are derived from CAD data. The powder bed is lowered at the completion of each layer by lowering the bottom of the rectangular cylinder which contains the bed. Figure 1.2 depicts the steps involved in creating a part. Unbound powder temporarily supports unconnected portions of the component, allowing overhangs, undercuts and internal volumes to be created. The unbound powder is removed upon process completion, leaving the finished part.

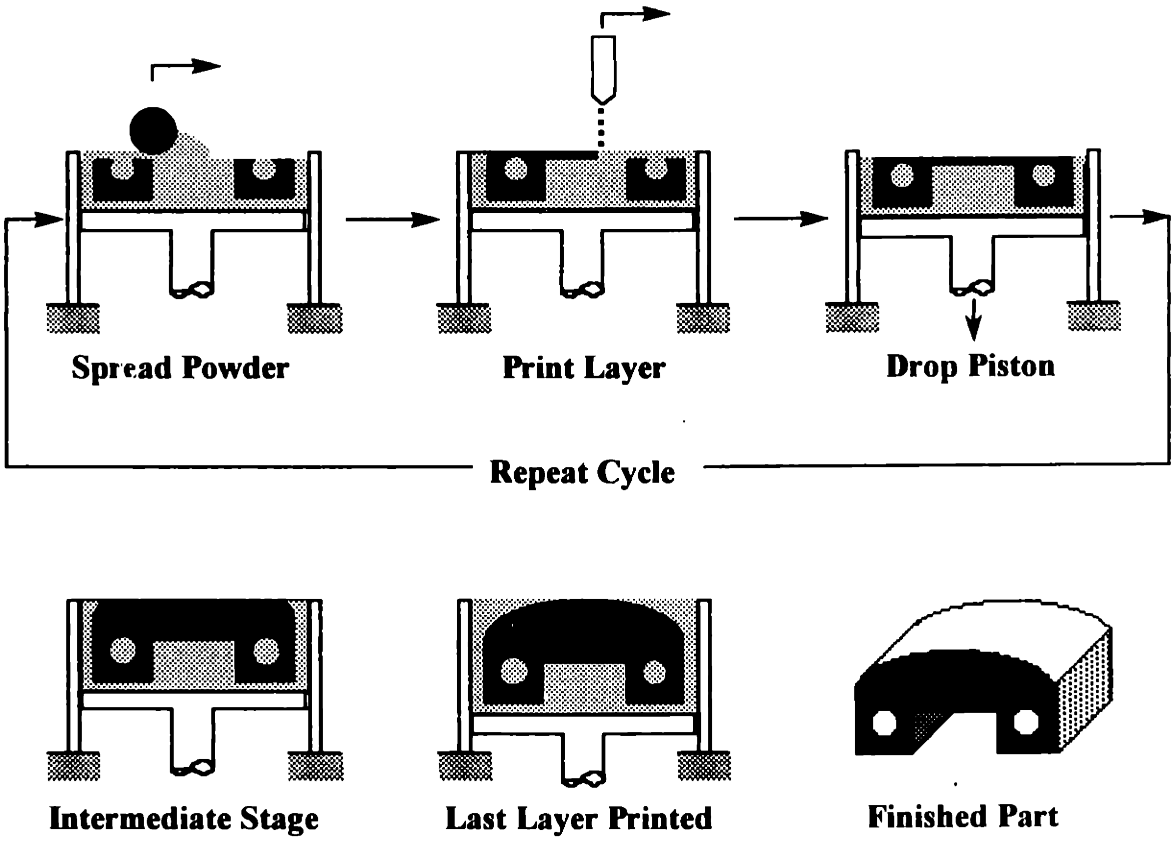

Figure 1.2: The 3D Printing sequence.

This research effort employs the 3D Printing process for the direct fabrication of metal injection molding tooling with conformal cooling channels. Stainless steel (316L) powder is selectively bound with a latex emulsion binder using the 3DP process resulting in a green part. A series of post-processing steps similar to those found in powder metallurgy processing are used to obtain all-metal injection molding tooling with conformal cooling passages.

1.4 Effect of Mold Surface Temperature on Molded Part Properties

There have been many research efforts aimed at determining the effect of the mold surface temperature on the molded part. Han and Villamizar carried out an experimental study to investigate the development of stress birefringence patterns of molten polymer during the mold filling and cooling operation. Their study showed how molding conditions influence the distribution of stress birefringence patterns. They showed that mold temperature influences the amount and distribution of residual stress in the molded part. [Han, 1977]

Fritch studied the effect of mold temperature on impact strength. He concluded that the mold temperature significantly influences molded part properties. He showed that the improvement of impact strength is greatest at low melt temperature and at high mold temperature. [Fritch, 1982] Burke and Newcome made an assessment of the mold temperature influence on molded part quality of semicrystalline polymer. This study showed that mold temperature can directly influence the physical properties of semicrystalline material because it affects the degree of crystallinity. [Burke, 1982]

It is obvious that the processing behavior of a plastic is highly influenced by the mold surface temperature. To produce parts to the correct dimensions and tolerances, the cavity temperature must be controlled during the molding process. With increasing part quality requirements, tighter dimensional tolerance, and reduced rejection rates, tighter temperature control of the mold cavity is paramount. It affects molding cycle rates and the part's physical properties, appearance, and dimensions. Uneven cavity temperatures result in parts with molded-in stresses, warped sections, sink marks, poor surface appearance, and varying part dimensions from cycle to cycle and even cavity to cavity. [Gordon, 1993]

Typically, the cooling system is the last area to be considered when designing and building a mold. As a result, the cooling channels must be routed around the cavity as best they can, and the number and size of the cooling circuits are often limited by the part's ejector system. Often, it is not possible to place cooling channels in the inserts. Channels must be placed in the bolsters or support blocks instead. Too often, cooling is not even considered until it is too late in the tool design stage to change the mold so that it provides the proper temperature control required for the cavity. [Gordon, 1993] This thesis characterizes the impact of cooling channel placement and design on the mold surface temperature. The flexibility of creating conformal channels using the Three Dimensional Printing process invites the mold designer consider cooling channel designs previously impossible to manufacture.

1.5 Goals

The goal of this research is to develop injection molding tooling with conformal cooling channels and to determine whether the conformal passages provide improved mold surface temperature control over conventional straight - drilled channels. This effort will focus on a direct comparison of the mold surface temperature during the injection cycle of a 3D Printed mold with conformal channels and a mold machined with conventional straight channels. An objective of this thesis is to determine the degree to which these conformal cooling channels in injection molding tooling effect surface temperature control and uniformity. Issues such as powder removal and post processing of green parts with small cooling channels are also investigated.

2. Printing Injection Molding Tooling

This chapter describes the process of creating a 3D Printed green injection molding tooling insert with conformal channels. Specific 3D Printing process parameters are discussed as well as powder removal from channels of green metal 3D Printed parts.

2.1 Printing Green Tooling Inserts

The overall process of creating a metal part can be divided into several steps. First, the green part is printed using the 3DP system by using a temporary organic binder. Powder must then be removed from the insert cavities and cooling channels. Finally the green part must be subjected to a series of post processing steps. Figure 2.1 depicts a set of 3D Printed core and cavity inserts with conformal channels in the green state. These inserts will be characterized in detail in later chapters.

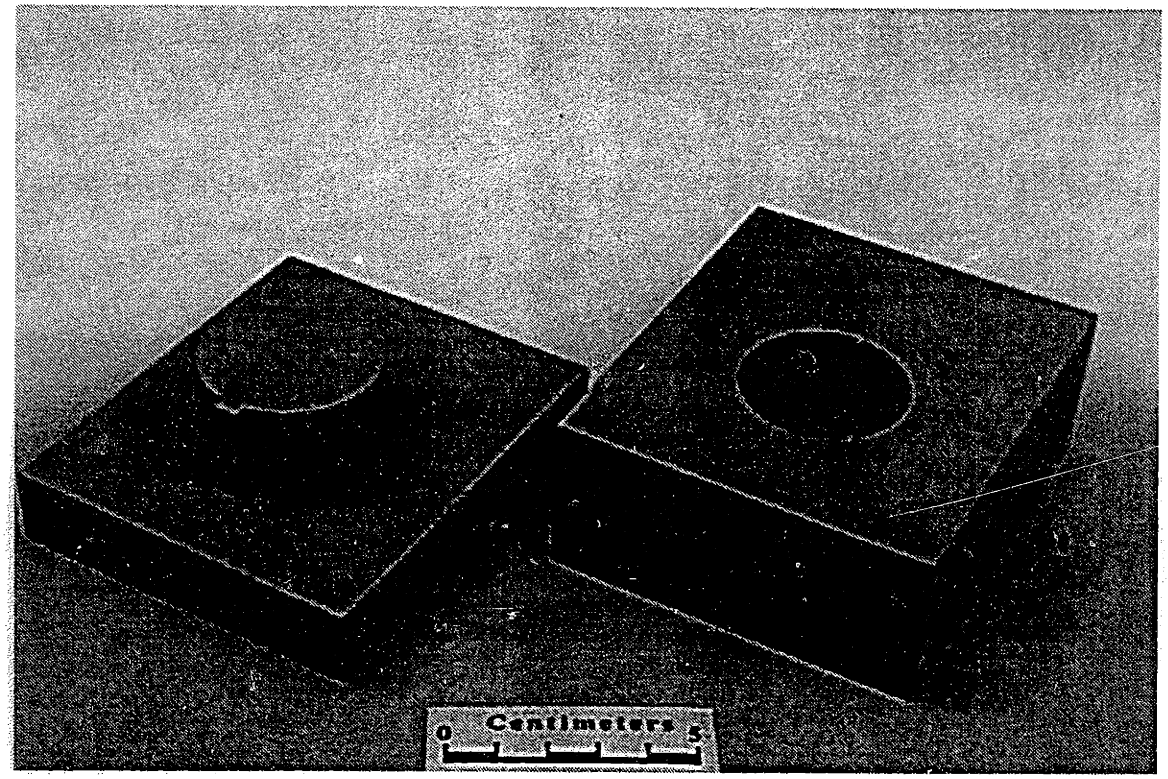

Figure 2.1: 3D Printed green cavity and core inserts.

The powder used in creating green 3D Printed tooling was a 316L spherical stainless steel powder with a size range of 60 μm. [Alcan] Appendix A describes a metal salt powder coating procedure used to prevent ballistic ejection, balling and shifting of the powder during printing. [Michaels, 1993] An aqueous acrylic copolymer emulsion was used as the binder. [Acrysol, Rohm and Haas] This emulsion is self-crosslinking and cures by drying in air to form a high durometer solid. The binder was diluted with water to 20% acrylic solids by weight. Total flow rate was 0.82 cc/minute. The thickness of each layer was 170 μm in all the experiments.

A pair of 3D Printed cavity and core inserts were printed using a single-jet continuous jet printhead. [Brancazio, 1991] The individual printed lines which are stitched together to form each layer were spaced 175 μm apart. The core insert was used to test various infiltration techniques. This core insert was badly eroded and could not be used for experimentation. The cavity insert was successfully infiltrated, machined and used in the mold surface temperature tests.

An eight-jet continuous jet printhead was developed after the printing of the first set of inserts. [Shutts, 1995] The printhead produced parts that exhibited excessive bleeding of binder into the powder. This problem was solved by increasing the line spacing to 185 μm. The final core insert used for experimentation was printed using this eight-jet continuous jet printhead with a line spacing of 185 μm.

Both the core and the cavity inserts were printed oversize (2% in each direction) compared to their final required dimensions to account for shrinkage. A 1.5 mm layer was added to all outer dimensions of the parts for post-machining.

After completion of the printing process the entire powder bed was allowed to air dry for a period of 24 hours. The inserts were then placed in an oven at 100°C for one to two hours to completely cure the acrylic binder. The green part was then removed from the powder bed. The remaining attached powder on the exterior of the insert was easily blown off with compressed air.

2.2 Powder Removal from Conformal Cooling Channels

After printing, complex cavities and cooling channels of the green metal part must be cleared of powder. In order to test the ability to remove powder from complex passages a powder removal test shell was designed. The shell design and powder removal techniques originate from powder removal experiments on 3D Printed ceramic parts conducted by Mark Grodzinsky. [Grodzinsky, 1994] This experiment was devised to evaluate the minimum size cooling channel that could be cleared of powder. A thin box shaped shell was designed such that it could be easily split open and the contents of the channels could be viewed. Figure 2.2 is a schematic of the five centimeter long opened test shell containing three straight channels and one zig-zag channel.

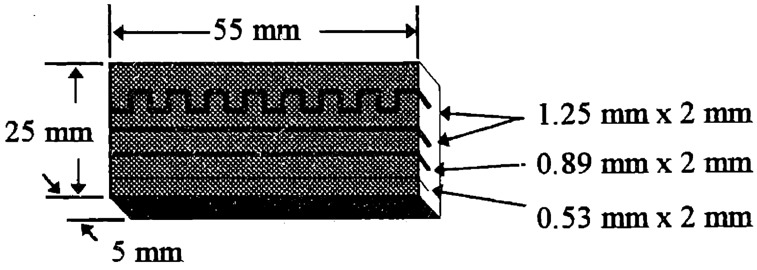

Figure 2.2: Schematic of opened powder removal test shell.

The individual printed lines which were stitched together to form each layer were spaced 175 µm apart. Passages are formed by having the printhead selectively pass over loose powder without printing polymeric binder. Thus, each pass of the printhead creates a line of bound or unbound powder that is 175 µm wide. The smallest channel in the shell is created by not printing during three passes of the printhead, creating a nominal channel width of 525 µm. The middle channel is five passes wide (875 µm), and the largest channel and the zig-zag channel are seven passes wide (1.225 mm). All channels are 2 mm deep.

The test shell was designed such that the top of the shell could be pulled off to reveal the contents and observe the quantity of residual powder. One of the middle layers of the part contains only thin lines that were printed between the channels and around the perimeter of the shell. The lines printed between the channels prevent powder from jumping from one channel to the next during powder removal. The line printed around the perimeter of the part aids in securing the top of the shell to the bottom. Because only these few lines fasten the top of the shell to the bottom, this weak layer acts as a delamination layer providing easy separation of the top of the shell after the powder removal experiment has been conducted. Figure 2.3 is a schematic of the cross section of the shell.

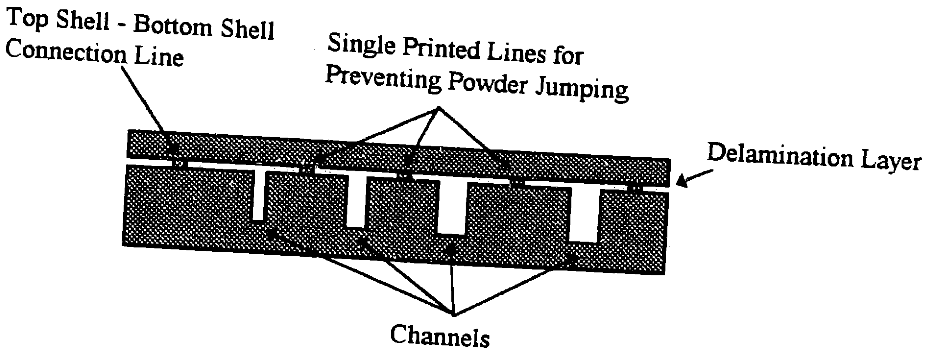

Figure 2.3: Cross - section of powder removal part depicting the channel size and delamination layer

Three methods of powder removal were investigated. Air vacuum, pulsed air and a soda water vacuum powder removal method developed by Mark Grodzinsky. The air vacuum method involved evacuating a large tank to 3 kPa absolute pressure. A small rubber tube was connected to a valve on the tank. The tube end was held to the channel opening and the valve was opened drawing the powder out of the channel.

The pulsed air method employed a small air compressor connected to another small rubber tube. During powder removal the small tube was placed about a centimeter from the opening of the channel to blow the powder out.

A final method used to clear the test shell involved placing the green part in a bath of soda water. This process works by evacuating a large tank to 3 kPa absolute pressure and then instantaneously evacuating a chamber filled with soda water and the part to be cleared. The instantaneous evacuation of the vacuum chamber makes the carbon dioxide less soluble within the soda water and causes it to bubble out vigorously. These bubbles exit the part through the hole and take the loose powder out with them. This powder removal technique adds a requirement that the polymeric binder in the green part be able to withstand water immersion for a period of time without resulting in distortion of the green part. Figure 2.4 describes the setup for the soda water vacuum powder removal procedure.

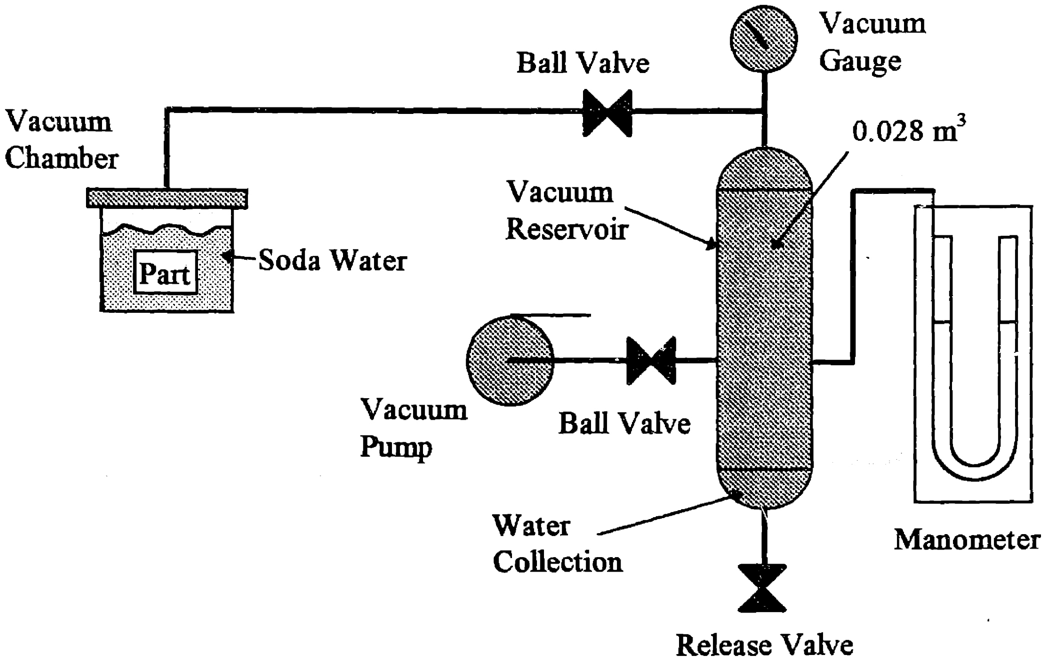

Figure 2.4: Soda water vacuum powder removal setup. [Grodzinsky, 1994]

Four parts were used to test each powder removal procedure. Each part was weighed before and after powder removal to obtain a measure of how much powder can be removed using each procedure. Figure 2.5 and Table 2.1 describe the results of this investigation.

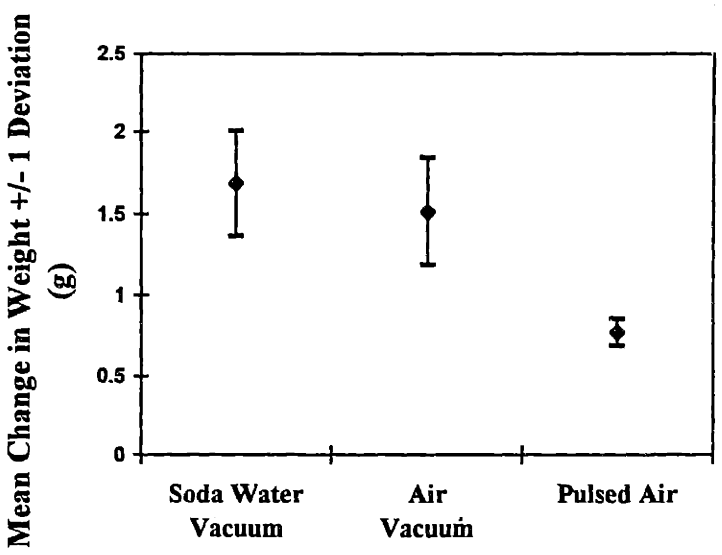

Figure 2.5: Mean change in weight vs. powder removal procedure.

Removal Procedure	Part #	Weight (g)	Cleared Weight (g)	Change in Weight (g)	Mean Change in Weight (g)	Standard Deviation
Soda	Part 1	28.00	26.78	1.21	1.69	0.32
Water	Part 2	28.06	26.17	1.89		
Vacuum	Part 3	27.86	26.11	1.75		
	Part 4	27.75	25.85	1.90		
Vacuum	Part 1	27.52	25.73	1.80	1.51	0.33
	Part 2	27.87	26.78	1.09		
	Part 3	27.74	26.30	1.44		
	Part 4	27.50	25.76	1.74		
Pulsed	Part 1	27.83	27.14	0.70	0.77	0.08
Air	Part 2	27.76	27.00	0.76		
	Part 3	27.61	26.72	0.89		
	Part 4	27.99	27.24	0.75		

Lines placed in connection layer to prevent "jump" effect

Table 2.1: Change in weight results for each powder removal procedure and test part.

Results indicate that the soda water vacuum procedure clears the greatest amount of powder out of the channels. Air vacuum is slightly less effective and pulsed air clears considerably less powder.

After powder removal was completed the test shells were opened at the delamination layer. Inspection of the open channels revealed that the soda water vacuum process cleared all of the passages. The air vacuum treatment cleared all of the passages except the smallest one. The pulsed air treatment cleared only the largest straight passage. Figure 2.6 shows a picture of three powder removal shells cleared by each of the three powder removal procedures.

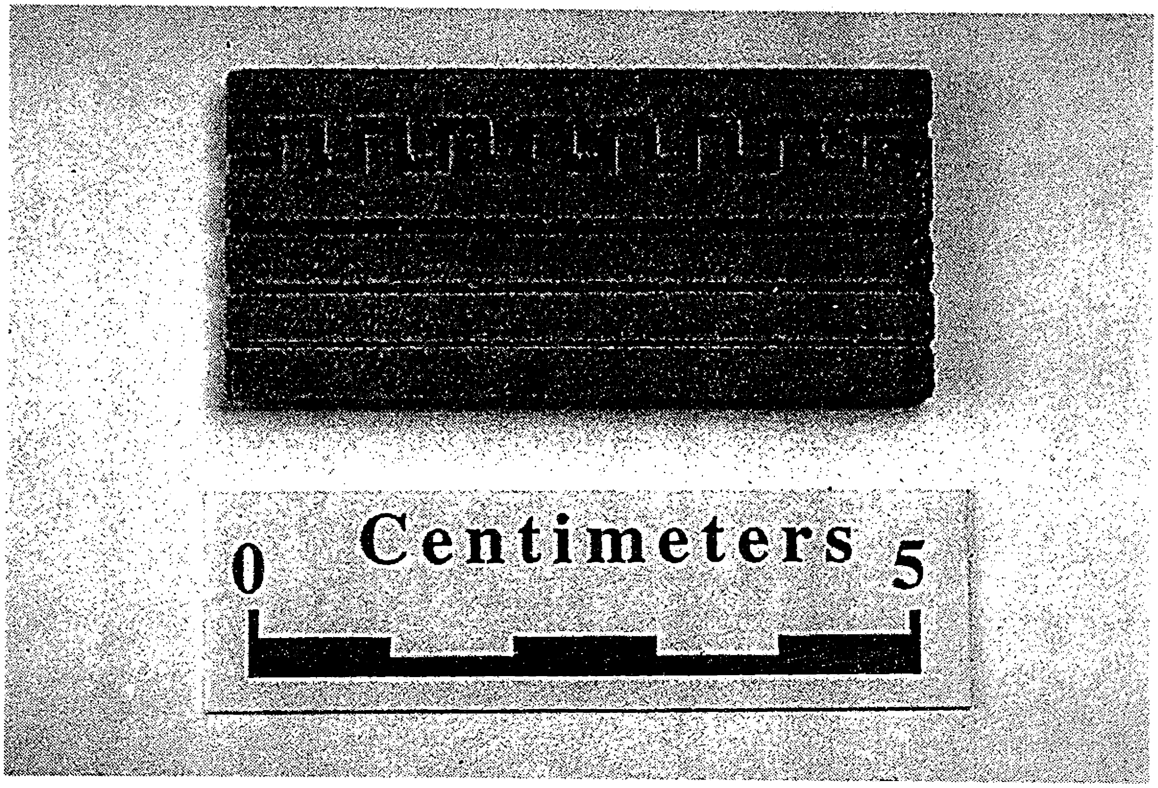

Figure 2.6: Opened powder removal test part cleared with soda water vacuum powder removal procedure.

3. Post-Processing of Green Inserts

After printing and powder removal, the part is processed using techniques similar to those used in metal injection molding (MIM). In debinding, the organic binder used in the 3D Printing process thermally decomposes in an inert gas furnace. Metal skeletons have sufficient strength to be handled after debinding, however, it is advantageous to sinter the part in the same firing schedule at higher temperature to increase its strength. Finally, the part is infiltrated with a lower melting point alloy to 100% density.

3.1 Debinding and Sintering

Binder was removed from the green part by thermal decomposition in an inert gas tube furnace. [Michaels, 1993] The binder polymer chains are broken by heating during thermal decomposition and the binder is evolved as a gaseous product. A typical 3DP green part is 10% by volume binder, leaving approximately 30% open porosity.

Debinding and sintering was executed in an Argon / 5% Hydrogen atmosphere tube furnace A typical debinding and sintering firing schedule is as follows:

1. Ramp up at 5 °C per minute to 200 °C and hold for 20 minutes.
2. Ramp up again at 5 °C per minute to 500 °C.
3. Ramp up immediately at 10 °C per minute to 1350 °C (sintering temperature) and hold for 1 hour.
4. Ramp down at 20 °C per minute to room temperature.

A typical debinding and sintering process requires eight hours. Upon completion of the debinding and sintering process, the cavity insert exhibited dimensional change of approximately -3% along the x, y and z axis. (The x axis is along the printed line, the y axis is across the printed line, and the z axis is across the printed layers.) This shrinkage value is based on the sintering temperature of 1350 °C. Parts have been successfully sintered at a temperature of 1275 °C and yield less shrinkage. The core insert was sintered at 1275 °C and yielded dimensional change of approximately -1.5% shrinkage. Appendix B describes the shrinkage of the core and cavity 3D Printed inserts.

Metal skeletons have sufficient strength to be handled after the debinding and sintering step described above. The firing schedule described above yielded parts with a final density of 64% of theoretical.

3.2 Infiltration

The infiltration of porous metal preforms with a lower melting temperature alloy is a common practice for increasing part strength and removing residual porosity [Michaels, 1993]. This section will describe two methods of infiltration as well as an infiltration process that produces parts with small open channels and channels or voids filled with solid bronze infiltrant.

3.2.1 Infiltration on flat substrates

Earlier attempts were made at infiltrating parts on a simple flat alumina substrate. Bronze infiltrant was placed on top of the part in these firing attempts. The bronze infiltrant did not infiltrate the part and ran off the top of the part to the edges of the crucible. These results indicated a need to force the molten infiltrant in contact with the part.

The porous stainless part was placed in a machined graphite crucible. The crucible consisted of a pocket machined in a block of graphite. This crucible was designed to have shelves around the perimeter of the pocket. Each shelf was slanted at an angle of 11 degrees toward the pocket. The walls of the pocket exhibited a slope of 10 degrees.

Alumina paint was spread on the surface of the crucible to prevent bonding of the part to the graphite crucible. Sintered blocks of a 10% tin bronze shot were positioned on the shelves of the crucible and the sintered part was placed in the pocket. The materials were heated to 1100 °C in an argon/5% hydrogen atmosphere. Once at temperature, the molten infiltrant melts on the shelves and spills into the space surrounding the sintered part. The molten bronze then enters the part through the side wall. The excess infiltrant on the side of the part was machined off after infiltration. The infiltration process is illustrated in Figure 3.1.

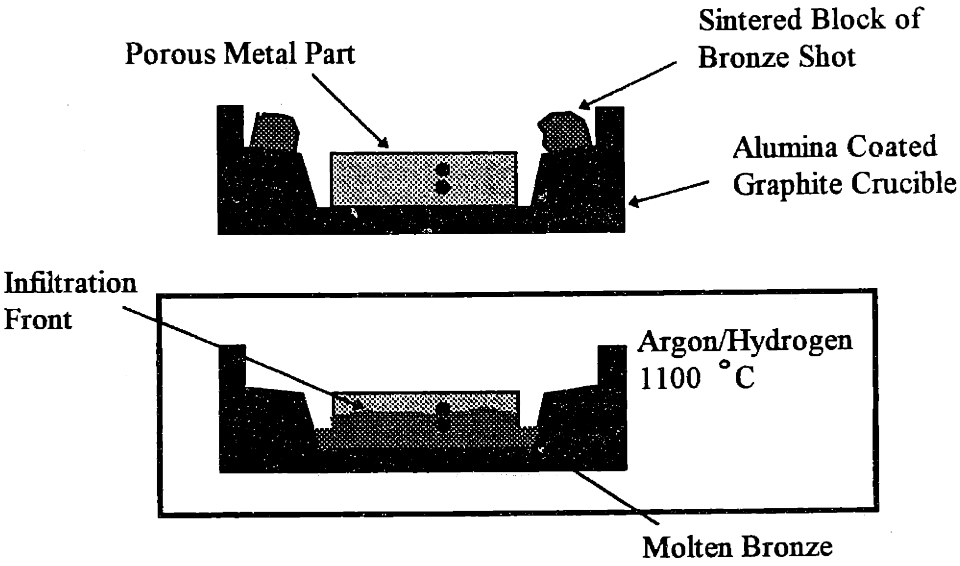

Figure 3.1: Infiltration on a flat substrate.

This method of infiltration was used successfully in infiltrating the 3D Printed cavity insert. However, this process has several drawbacks. A relatively precise amount of bronze infiltrant must be calculated for the part to be infiltrated. There is a definite possibility of under infiltrating the part in this case. If the amount of infiltrant used is greater than is needed, excess bronze must be machined off the part. In tooling inserts with conformal passages there is also a danger of the channels filling with infiltrant.

Another problem with this process is that the bronze infiltrant contacts the part as soon as it is in the molten state due to the fact that it rolls off the shelves. During the period of time in which the infiltrant is molten but is not at the infiltration temperature erosion may be happening. These drawbacks led to a search for an improved infiltration method.

3.2.2 Infiltration on Porous Stilts

A second method of infiltration was born out of the need for an infiltration process that may be used to reliably infiltrate tooling with small cooling channels. A green powder removal part described in Chapter 2 was de-bound and sintered for this experiment. Again, the smallest channel in the shell has a nominal channel width of 525 μm. The middle channel is 875 μm wide, and the largest channel and the zig-zag channel are 1.225 mm wide. All channels are 2 mm deep.

Several cylindrical 40 micron grade porous 316L stainless steel filter elements produced by Mott Metallurgical Company were used in this experiment. A graphite crucible with a deep pocket was machined to tightly fit the dimensions of the powder removal part. Holes were drilled in the bottom of the crucible to support the cylindrical filter elements and the crucible was coated with alumina paint.

The filter elements were first placed in the support holes and the bronze shot was then placed around the porous stilts. Enough bronze was used to infiltrate the stilts and the sintered part and to leave a puddle of molten bronze on the bottom of the crucible. The part was then placed on top of the stilts. Figure 3.2 shows the stilt infiltration process.

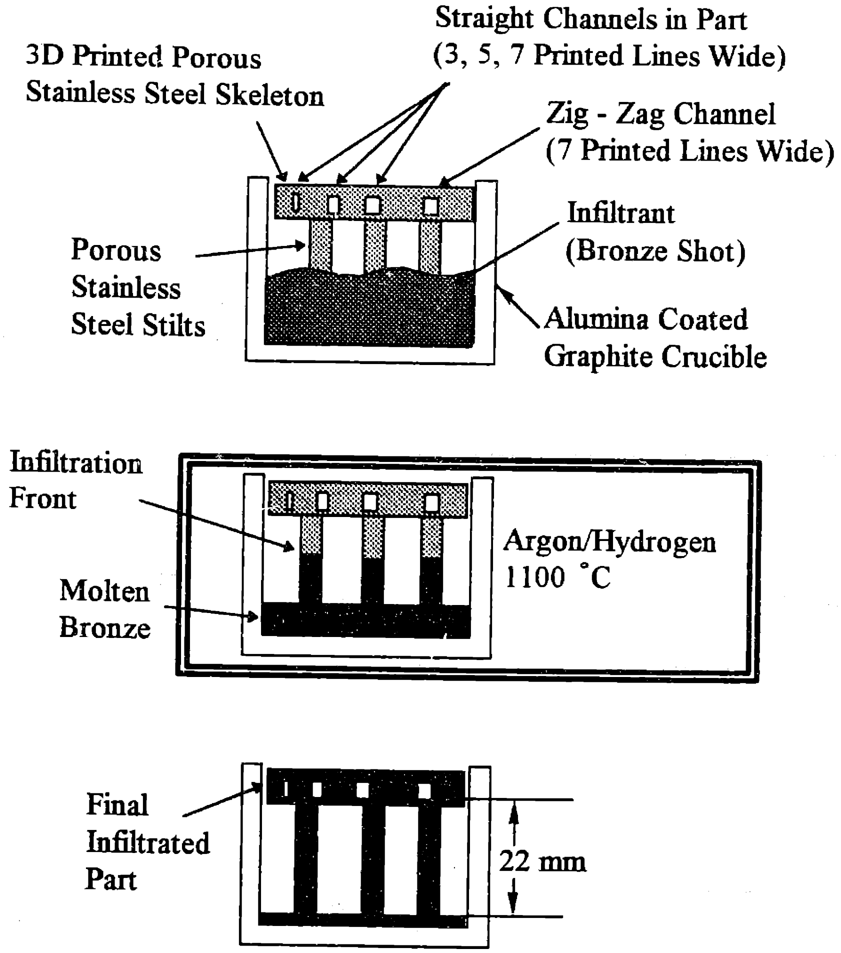

Figure 3.2: Infiltration on porous stilts.

The stilt infiltration process relies on capillary forces to draw the molten bronze infiltrant up the stilts and into the sintered part. The small pores in the sintered part and stilts are interconnected and may be modeled as a vertical "tube" with an open bottom resting in the pool of infiltrant. This vertical tube has a height equal to the maximum height of the stilt - part arrangement. The diameter of the tube is assumed equal to the pore size. An equation relating the capillary force to the weight of the column of infiltrant in the tube yields a value for the maximum rise of infiltrant in the tube. This maximum rise is equal to the maximum height that the infiltrant will reach in the sintered stilt-part assembly. Equations 3.1 and 3.2 describe this relation:

$$2 \pi r \gamma \cos\theta = \rho g h \pi r^2 \; ; \; \theta = 0 \text{ degrees} \tag{3.1}$$

$$h = \frac{2\gamma}{\rho g r} \tag{3.2}$$

where

r = the radius of the column of infiltrant.

$\gamma\cos\theta$ = surface tension force per unit length of liquid bronze infiltrant. (1 N/m) [Semenchenko, 1962]

θ = the wetting angle between the surface and the plane of contact. (for perfectly wetting; $\theta = 0$ degrees)

ρ = density of bronze infiltrant. (8780 kg/m^3) [Lyman, 1961]

g = gravity.

h = height of column of bronze infiltrant.

It is assumed that the bronze infiltrant perfectly wets the stainless steel. This assumption yields a wetting angle of 0 degrees. The average pore size in the 3D Printed sintered stainless steel material is approximately 15μm. Equation 3.2 predicts for this pore size a maximum infiltrant rise of approximately 1.5 meters.

A method of predicting the necessary height of the stilts to ensure that a part with a given size channel will not be over infiltrated (channels clogged with infiltrant) was necessary. A model similar to the one used in equation 3.1 predicts this necessary height. The actual channels in the powder removal part are horizontally positioned. Rather than modeling the channels as a column of liquid, the channels are modeled as capillary rise between two parallel flat walls. Figure 3.3 shows a diagram of this model.

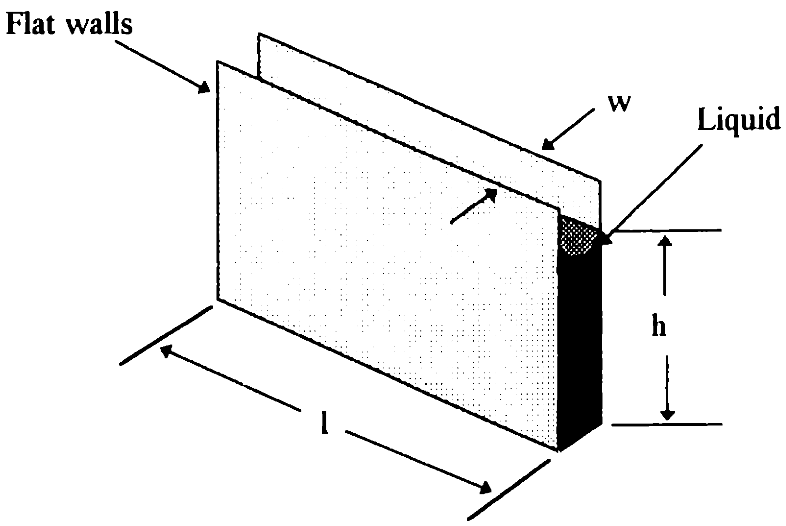

Figure 3.3: Capillary rise between two flat plates.

Again, it is assumed that the bronze infiltrant perfectly wets the stainless steel "walls". Equations 3.3 and 3.4 describe this relation:

$$2 l \gamma \cos\theta = \rho g h (l w) \;;\; \theta = 0 \text{ degrees} \tag{3.3}$$

$$h = \frac{2\gamma}{\rho g w} \tag{3.4}$$

where

l = length of the wall.

w = width of the channel. (distance between the two walls)

$\gamma\cos\theta$ = surface tension force per unit length of liquid bronze infiltrant. (1 N/m) [Semenchenko, 1962]

θ = the wetting angle between the surface and the plane of contact. (for perfectly wetting; $\theta = 0$ degrees)

ρ = density of bronze infiltrant. (8780 kg/m^3) [Lyman, 1961]

g = gravity.

h = height of infiltrant rise.

Employing equation 3.4 a prediction may be made for the height of the stilts needed to ensure that a channel of a given cross - sectional width will not fill with infiltrant.

Table 3.1 shows the predicted maximum capillary rise in the part and a description of the results of the experiment.

Channel Width (mm)	Calculated Maximum Capillary Rise (cm)	Actual Height of Channels from Pool of Bronze (cm)	Experimental Results
0.53	4.39	2.5	Partially Filled with Infiltrant
0.89	2.61	2.5	Partially Filled
1.25	1.88	2.5	Clear

Table 3.1: Results of stilt - infiltration test of powder removal part.

The calculated maximum capillary rise for the largest straight channel is less than the actual height of the channels from the pool of molten bronze infiltrant. This indicates that the infiltrant should not fill the channel. Results support the prediction that the largest straight channel in the powder removal part should remain clear of infiltrant. The calculated maximum capillary rise for the two smaller channels is greater than the actual height of the channels from the pool of molten bronze infiltrant. Appropriately, these channels partially filled with bronze infiltrant.

The top of the infiltrated powder removal part was machined off to reveal the inside of the channels. It was observed that the two smallest channels filled near the openings but remained clear inside. It was proposed that gas could have been trapped in the channels during infiltration. A stilt infiltration experiment in a vacuum furnace was designed to eliminate the possibility of trapped gas in the channels.

A second experiment was executed to determine the effect of furnace atmosphere on stilt height predictions. A new powder removal part was printed with five straight channels. The part had identical outside dimensions as the powder removal part. The channels were rectangular in cross section having channel widths of 3, 4, 5, 6, and 8 printed lines. This corresponds to channel widths of 0.53 mm, 0.71 mm, 0.89 mm, 1.07 mm, 1.42 mm. All channels were all 2mm high. These channel sizes reflect the CAD dimensions of the part.

After printing and powder removal, the part was sintered in a tube furnace in an argon/5% hydrogen atmosphere. The part was then infiltrated on stilts in a vacuum furnace (10^{-5} Torr). Stilts providing a molten bronze pool to channel height of 2.5 cm were used. Table 3.2 describes the results of this experiment.

Channel Width (mm) CAD Dimension	Calculated Maximum Capillary Rise (cm)	Actual Height of Channels from Pool of Bronze (cm)	Experimental Results
0.53	4.39	2.5	Filled with Infiltrant
0.71	3.27	2.5	Filled
0.89	2.61	2.5	Filled
1.07	2.17	2.5	Filled
1.42	1.64	2.5	Partially Filled

Table 3.2: Results of second stilt infiltration test part and calculated maximum capillary rise for channel widths (CAD dimensions).

Unfortunately all of the channels in the part at least partially filled. This was an unexpected result based on the calculated maximum capillary rise for the given channel widths. A possible explanation for this occurrence is the high surface roughness on the inside of the channels. When the channels are relatively small, the surface roughness effectively decreases the width of the channel. Figure 3.4 describes this idea.

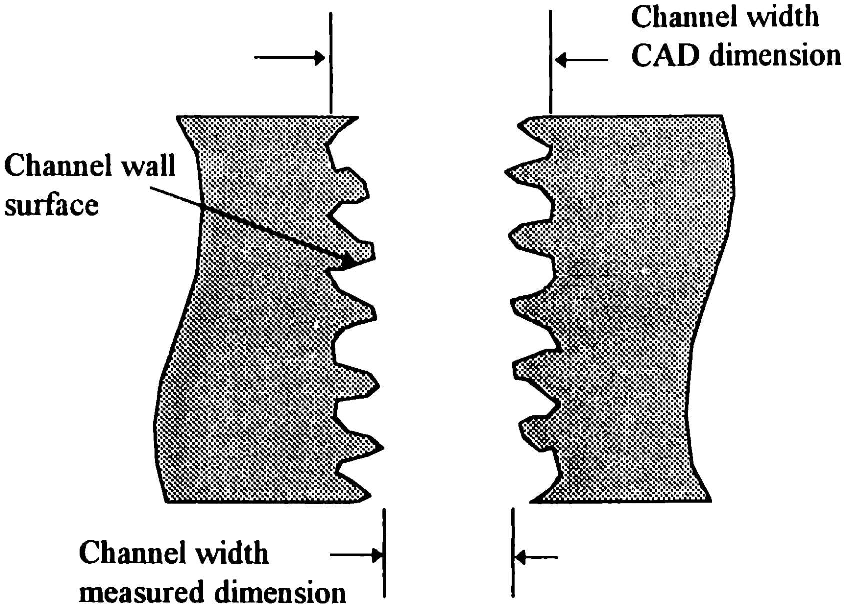

Figure 3.4: Surface roughness on inside of channels.

This effective decrease in channel width increases the maximum capillary rise of the infiltrant. Measurements of the channel widths were made with an optical microscope. Table 3.3 describes the effective (measured) channel widths and the new calculated maximum capillary rise.

Channel Width (mm) Measured Dimension	Calculated Maximum Capillary Rise (cm)	Actual Height of Channels from Pool of Bronze (cm)	Experimental Results
0.13	17.9	2.5	Filled with Infiltrant
0.28	8.3	2.5	Filled
0.46	5.1	2.5	Filled
0.64	3.6	2.5	Filled
1.02	2.3	2.5	Partially Filled

Table 3.3: Results of second stilt infiltration test part and calculated maximum capillary rise for effective (measured) channel widths.

The results presented in table 3.3 indicate that the measured channel widths are considerably smaller than the CAD dimensions. This effective decrease in channel width increases the maximum capillary rise. Using this measured channel width the calculated capillary rise correctly predicts the results of this experiment.

A final experiment was conducted to determine whether the relation for the maximum capillary rise is accurate for a 3D Printed part with a smooth channel surface. Six holes having varying diameters were drilled in a block of green 3D Printed material. The holes drilled in the green 3D Printed material exhibited a relatively smooth surface finish.

The 3D Printed block measured 9 x 25 x 38 mm. The drilled channels have diameters of 0.81 mm, 1.27 mm, 1.60 mm, 1.96 mm, 2.26 mm, 2.46 mm. Figure 3.5 depicts a schematic of this test part. After sintered in a tube furnace in an argon/5% hydrogen atmosphere the part was infiltrated on stilts in a vacuum furnace. Stilts providing a molten bronze pool to channel height of 2.7 cm were utilized. Table 3.4 describes the results of this experiment.

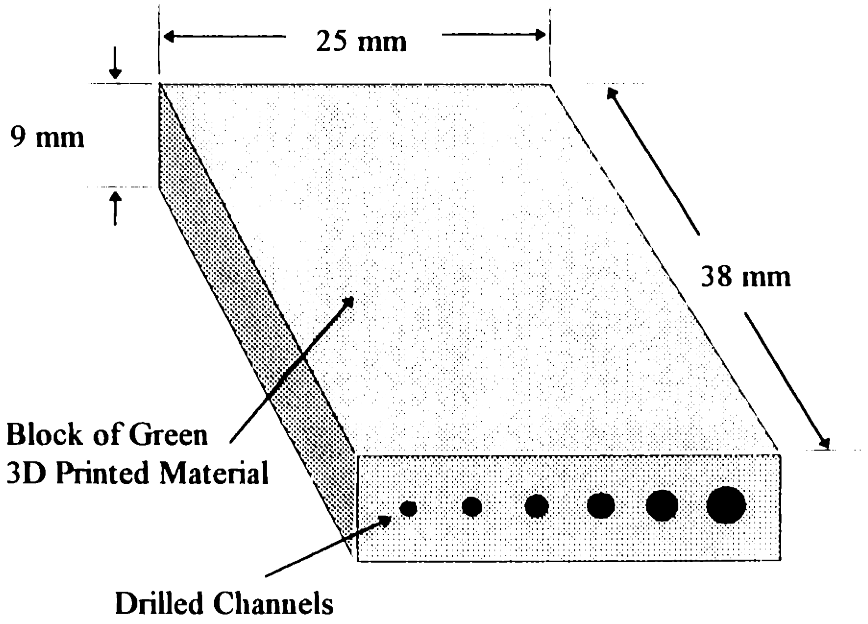

Figure 3.5: Infiltration test part with drilled channels.

Channel Diameter (mm)	Calculated Maximum Capillary Rise (cm)	Actual Height of Channels from Pool of Bronze (cm)	Experimental Results
0.81	2.86	2.7	Filled with Infiltrant
1.27	1.83	2.7	Clear
1.60	1.45	2.7	Clear
1.96	1.19	2.7	Clear
2.26	1.03	2.7	Clear
2.46	0.95	2.7	Clear

Table 3.4: Infiltration results for test part with drilled channels.

The results of this experiment demonstrate accurate agreement with the calculated maximum capillary rise equation. The one (smallest channel) that was predicted to fill with infiltrant did fill. All others remained clear as predicted.

A brief summary of the observations made in the above experiments is as follows.

1. Utilizing the stilt infiltration process the parts with small channels may be successfully infiltrated without danger of filling the channels with infiltrant.
2. The equation for the maximum capillary rise between two flat plates is fairly accurate for predicting necessary stilt height for infiltration of parts with small channels.
3. High channel surface roughness significantly effects the prediction of the maximum capillary rise. The surface roughness effectively decreases the width of the channel. This decrease in width increases the predicted maximum capillary rise. Thus, for channels with a high surface roughness the channel width should be measured as the distance between the highest points on each wall surface.
4. The stilt infiltration process offers a significantly reduced risk of under-infiltration due to the fact that the pool of molten bronze on the bottom of the crucible feeds the open porosity in the part.
5. Reduced erosion of the part may be possible using the stilt infiltration method. The molten bronze infiltrant makes contact with the stainless steel stilts before it reaches the part. This reduced erosion was exhibited in several part infiltrations. However, erosion was evident on the bottom of a large stilt infiltrated 3D Printed cavity insert printed for 3M. It is unclear why this erosion occurred.

3.2.3 Creation of Tooling with Clear and Infiltrant Filled Channels

The purpose of cooling channels in injection molding tooling is to control the mold surface temperature. Depending on the mold geometry and the thermal conductivity of the metal powder used in the 3D Printing process it may be necessary to place channels very close to the mold surface. The placement of the channels just below the mold surface is limited by the high pressures in the molding cavity. A possible solution to this problem is to create a mold made of a functionally gradient material.

The bronze infiltrant has a thermal conductivity value of 50 W/m-°C. [Lyman, 1961] This value is almost twice as high as that of the 3D Printed material. (26.3 W/m-°C) The ability to place regions of pure bronze infiltrant just below the mold surface is a method of increasing the heat transfer in the tooling while providing support to the molding surface.

The general method of creating regions of bronze along with clear channels is summarized as follows:

1. Design a part with a channel or empty region such that the powder may be removed after printing and the openings to the channel may subsequently be blocked to create a void space in the part. Create cooling channels designed to be clear of infiltrant. Leave the openings to these channels unblocked.
2. Print the part, remove powder from the channels and block the openings of the channels designed to fill with infiltrant with a powder/binder paste.
3. Debind and sinter the part.
4. Fully embed the part in infiltrant ***under vacuum***.
5. Subject the part to the infiltration temperature again in a gas atmosphere furnace. The part must be placed on stilts high enough to allow the open channels to drain of infiltrant.

This procedure provides a part with open channels and channels (originally void space in part) that are filled with infiltrant. The open channels drain through the stilts in the final furnace run. The void spaces designed in the part retain infiltrant because the part material surrounding the void space remains infiltrated during the draining process described above (step 5) and no gas can get in the void space to allow the melt to drain.

An experiment was conducted to determine the feasibility of this infiltration procedure. A part was designed with six channels as shown in figure 3.6.

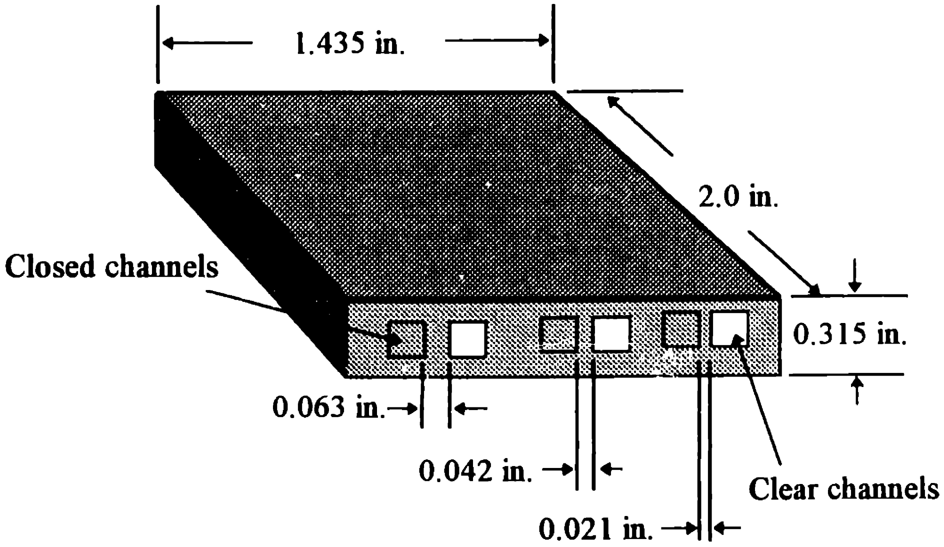

Figure 3.6: Experimental test part designed to have clear and infiltrant filled channels.

This test part was 3D Printed having three pairs of channels positioned side by side. One of the channels in each pair was printed blind on one end of the part. Each channel was square in cross-section having a side length of 0.125 inches. Each individual pair of channels was placed 3, 6 and 9 printed layers (0.021 in., 0.042 in., 0.063 in.) from the part surface and from each other. The pairs were placed at varying distances from the part surface to determine the sensitivity of the process to the wall thickness between the void space and the atmosphere.

After the part was printed the powder was removed from the channels. The open end of the blind channels were blocked with a pasty mixture of stainless steel powder and binder. The part was then sintered in an argon/5% hydrogen atmosphere furnace using the typical sintering schedule described in section 3.1.

The sintered part was then embedded in bronze infiltrant under vacuum. [Vacuum furnace work done at Materials Research Furnaces, Inc., Suncook, NH] The following firing schedule was used:

1. Ramp up at 10 °C per minute to 1100 °C (under vacuum)
2. Hold at 1100 °C for 15 minutes. (under vacuum)
3. Bleed Argon back to 1 atmosphere while at 1100 °C and hold for 10 minutes.
4. Ramp down at 10 °C per minute in Argon at 1 atmosphere.

Finally, the part was drained of the excess infiltrant by firing the part on stilts in a argon/5% hydrogen atmosphere tube furnace. The final step of this infiltration procedure requires that the large open channels drain of infiltrant while the pores in the stainless steel part remain filled with infiltrant. Figure 3.7 describes the steps involved in this infiltration procedure.

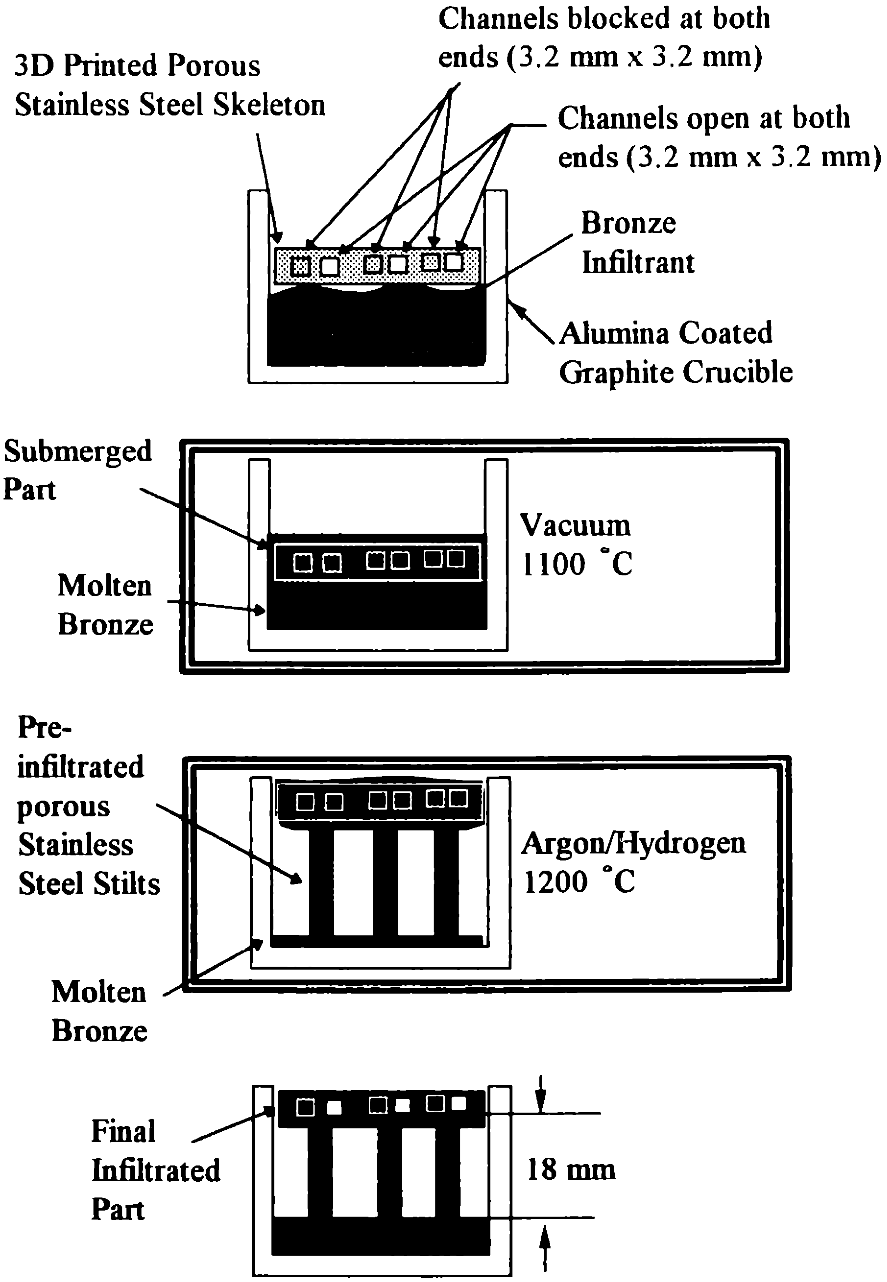

Figure 3.7: Infiltration process for the creation of parts with clear and infiltrant filled channels.

Figure 3.8 shows a schematic and a photograph depicting the results of this experiment. Each of the channels designed to remain clear of infiltrant successfully cleared. All of the channels designed to trap infiltrant did so. The part was sectioned and polished to show the bronze infiltrant filled channels and the clear channels side by side.

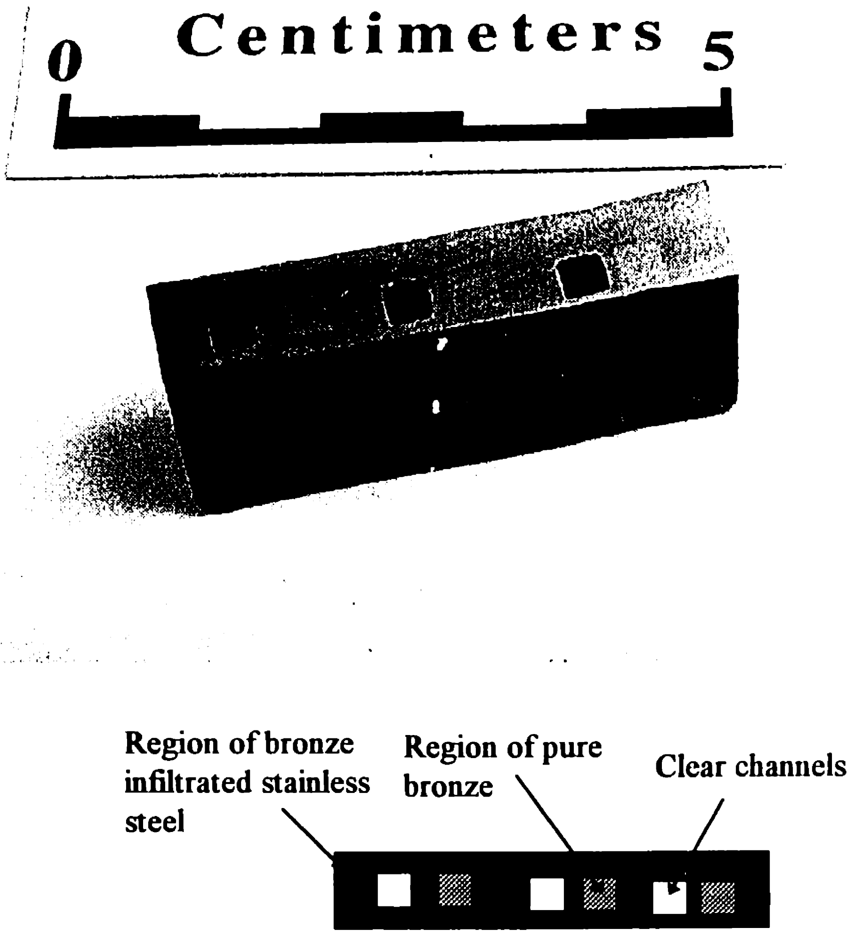

Figure 3.8: Results of bronze filled channel experiment.

4. Development of Injection Molding Tooling

This chapter describes the test part geometry chosen and the mold design used to create this geometry. A description of injection molding tooling inserts with straight channels and 3D Printed inserts with conformal channels is presented.

4.1 Plastic Part Geometry

A description of the goals of the plastic part geometry design is presented. The actual design chosen is illustrated and discussed in the following sections.

4.1.1 Goal

Determination of an optimal test part geometry was based on several required characteristics. A geometry was sought that contained the following features:

1. The geometry of the part should have some degree of curvature to exploit the ability to create conformal channels.
2. The part geometry should be sensitive (in terms of distortion) to the mold surface temperature.
3. The geometry should have characteristic features that can be easily measured to distinguish the amount of distortion that may exist. In this case "distortion" refers to the deviation of the plastic part dimensions from the mold cavity shape.
4. The part should naturally lend itself to a mold design requiring a core and cavity design.

4.1.2 Plastic Part Geometry Design

A ring shaped geometry was chosen for the plastic part design. A gap in the ring was designed to demonstrate clearly any distortion in the part. It was hoped that residual stress buildup in the part would exhibit itself in the form of the ring gap opening or closing. The width of the rib on the core insert that creates the gap in the ring measures 0.085 inches. A core and cavity design was chosen to mold the ring. A draft angle of 1.5 degrees was used to allow easy separation from the core insert side in ejection. A schematic drawing of the simple ring geometry is shown in figure 4.1 below.

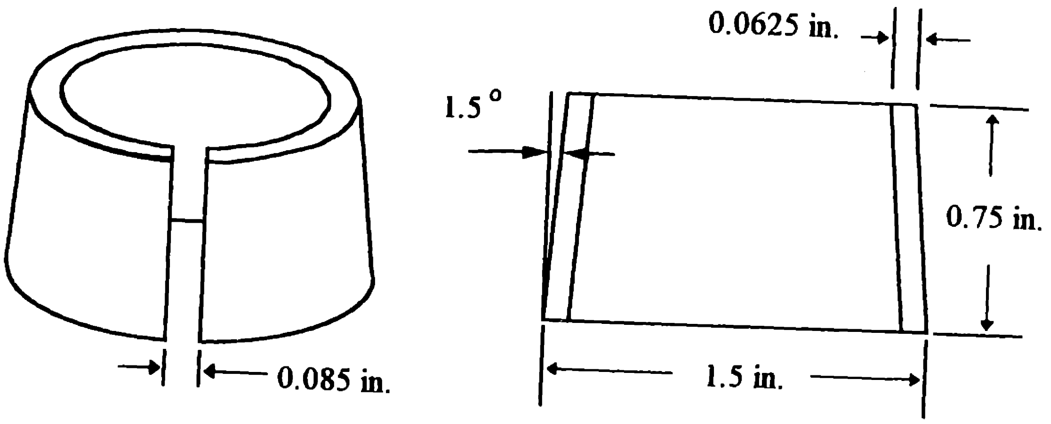

(A)

(B)

Figure 4.1: Isometric (A) and cross-section (B) schematics of polystyrene part geometry

A ring height of 0.75 inches and a ring thickness of 0.0625 inches were chosen. These dimensions were selected with the hope that residual stress buildup would manifest itself in the form of curling, sink marks or other forms of distortion along the height of the ring.

4.2 Mold Design

This section will provide a brief overview of the mold system used to produce parts with both the 303 stainless steel inserts with straight channels and the 3D Printed inserts with conformal channels. A description of the features associated with the cavity insert, core insert and overall mold assembly is presented. Cooling channel placement in each insert set is discussed.

4.2.1 Cavity Insert Design

The cavity insert is a rectangular block having a length of 3.5 inches, width of 3.0 inches and height of 1.5 inches. Figure 4.2 describes the basic features of this insert. The cavity insert was designed to fit in a slot milled in a M.U.D. frame bolster. The insert is fastened to the bolster with two 1/4 inch pins and two machine screws. A circular cavity is milled in the top face of the block. The diameter at the top of the block is 1.5 inches and the depth of the cavity is 0.75 inches. A 1.5° tapered end mill was used to apply draft to the cavity wall for easy part release. The sprue hole was also reamed with a 1.5° taper. A simple runner was milled in the top face of the insert with a 1/8 inch ball end mill. This runner was milled approximately 0.1 inches deep. The gate connects the runner to the actual mold cavity. The gate machined in the top face of the insert was 0.032 inches wide and 0.032 inches deep.

Three thermocouple holes were drilled next to the cavity wall for surface temperature measurement. The placement of these holes is discussed in detail in Chapter 5. Machine drawings in Appendix C provide detailed cavity insert dimensions.

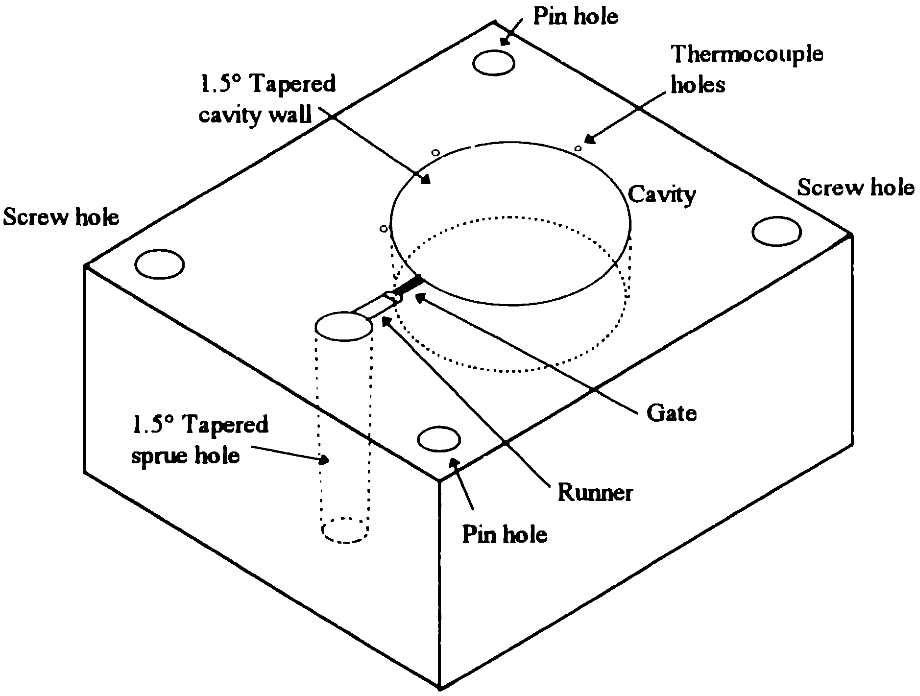

Figure 4.2: Cavity insert design.

4.2.2 Core Insert Design

The core insert consists of a rectangular base with a cylindrical shaped core. The rectangular base has a length of 3.5 inches, width of 3.0 inches and a height of 0.5 inches. Figure 4.3 describes the basic features of this insert. Like the cavity insert the core insert is fastened to a bolster with two 1/4 inch pins and two machine screws. The cylindrical shaped core sticks out of the top of the rectangular base. The core is 1.375 inches in diameter at the base and is 0.75 inches high. The wall of the core has a 1.5° taper matching the draft angle of the cavity wall. Again, this draft angle ensures easy release of the plastic part from the core.

The cylindrical core was designed with a rib to create the gap in the ring geometry. Two flat parallel walls were required for ease of gap width measurement. Thus, the rib on the core insert was machined such that the two walls of the rib were parallel. This machining operation was accomplished by milling with a 1/8 inch flat end mill the rib of the core with the core insert on its end.

Six 1/8 inch ejector pins evenly spaced around the perimeter of the core allow for easy ejection of the part. The core insert was designed with a shallowly tapped sprue puller hole. Polymer fills this hole, solidifies and the internal threads "pull" the polystyrene sprue out of the sprue hole. A 1/4 inch sprue puller pin then forces the sprue out and the part is ejected.

Three thermocouple holes were drilled next to the core wall for surface temperature measurements. Machine drawings in Appendix C provide detailed core insert dimensions.

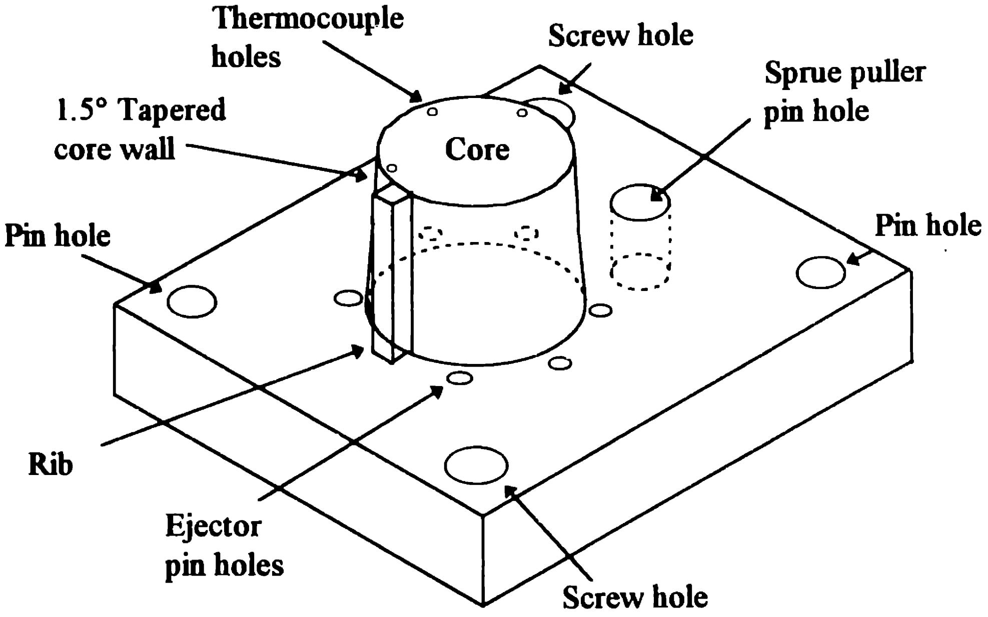

Figure 4.3: Core insert design.

4.2.3 Mold Assembly

The mold assembly utilizes a pair of mild steel assembly blocks in a M.U.D. frame. Recesses were milled in the assembly blocks to accommodate the two inserts. A simple ejector plate assembly was used for the ejector system. This ejector plate contained the six 1/8 inch part ejector pins, the 1/4 inch sprue puller ejector pin and four guide pins with return springs surrounding them. In part ejection a hydraulic ejector rod pushes the plate forward compressing the return springs. When the ejector rod pulls back the springs return the ejector plate to the back position pulling the ejector pins flush with the mold surface.

Figure 4.4 depicts a schematic illustrating the mold assembly and the polystyrene part with attached sprue.

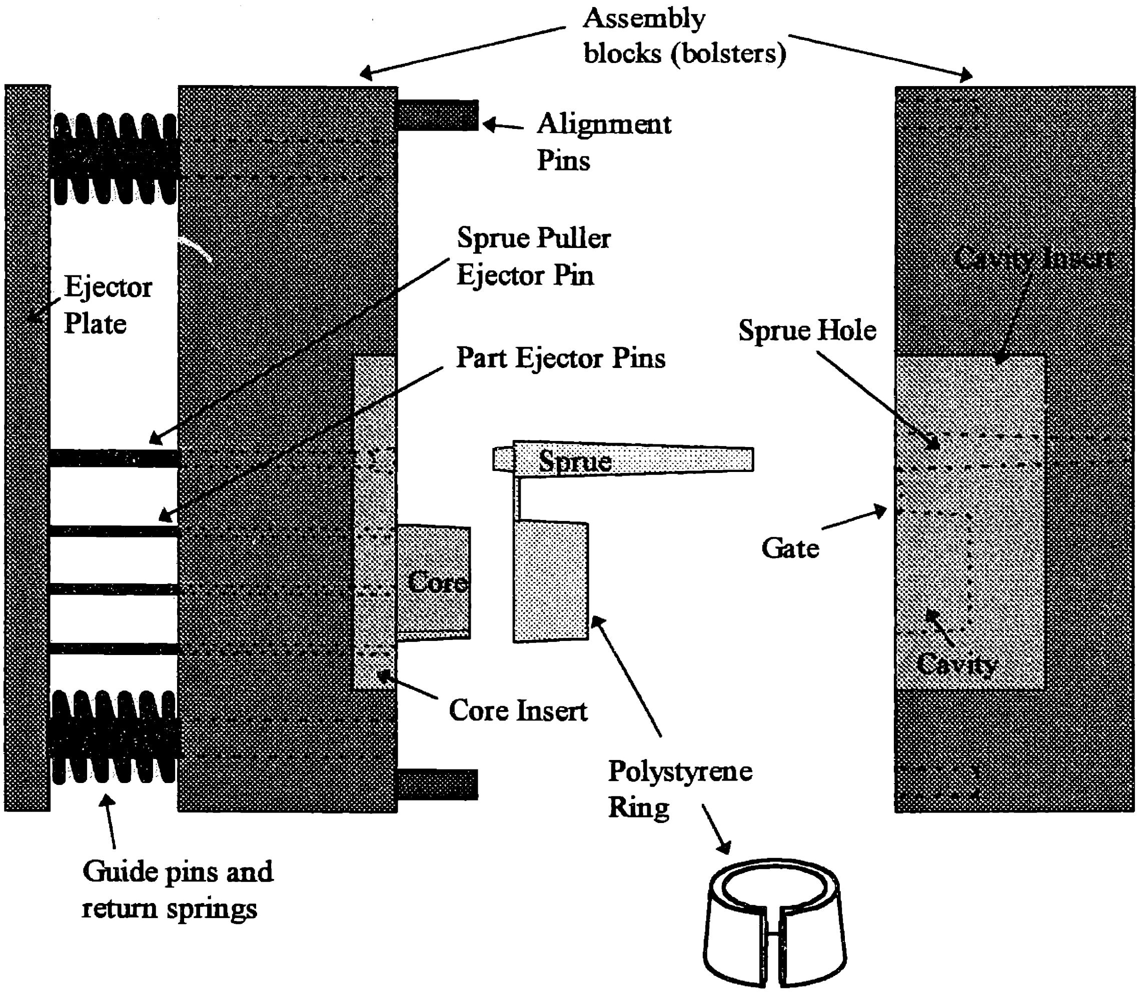

Figure 4.4: Mold assembly and the polystyrene part with attached sprue.

4.3 Straight Channel Design in 303 Stainless Steel Inserts

The first inserts made were created from 303 stainless steel. This material was selected because it offered the best match of thermal conductivity with 3D Printed 316L stainless steel infiltrated with bronze while offering relatively easy machining. The thermal conductivity of the 303 stainless steel is 13.8 W/m-°C and the thermal conductivity of the 3D Printed material is 26.3 W/m-°C. Appendix E describes an experiment conducted to determine the thermal conductivity of the 3D Printed material.

Core and cavity inserts were machined from 303 stainless steel. Conventional straight cooling channels were machined in these inserts for experimental comparison with the 3D Printed inserts. The diameter of the channels drilled in the 303 stainless steel inserts were designed to have the same cross sectional diameter as the conformal channels in the 3D Printed inserts. The diameter of the cooling channels to be used for both the straight and the conformal designs were chosen based on the minimum predicted size of channel that could be successfully cleared of powder in a 3D Printed part. A conservative cooling channel cross sectional diameter of 3/16 inch was chosen.

Two straight channels were drilled in the cavity insert as shown in Figure 4.5(A). These channels were drilled in-between the cavity wall and the sprue. The two channels were spaced evenly along the depth of the cavity. Figure 4.5(B) depicts channel placement in the core insert. Three straight channels were drilled in the rectangular base of the insert below the actual core. Placement of these inserts were limited due to the ejector pin placement. Detailed channel placement in the 303 stainless steel inserts is illustrated in machine drawings in Appendix D.

Simple 1/16 inch NPT to 3/8 inch Swagelock fittings were used to connect 3/8 inch Teflon tubing to the cooling channels in both the cavity and core inserts.

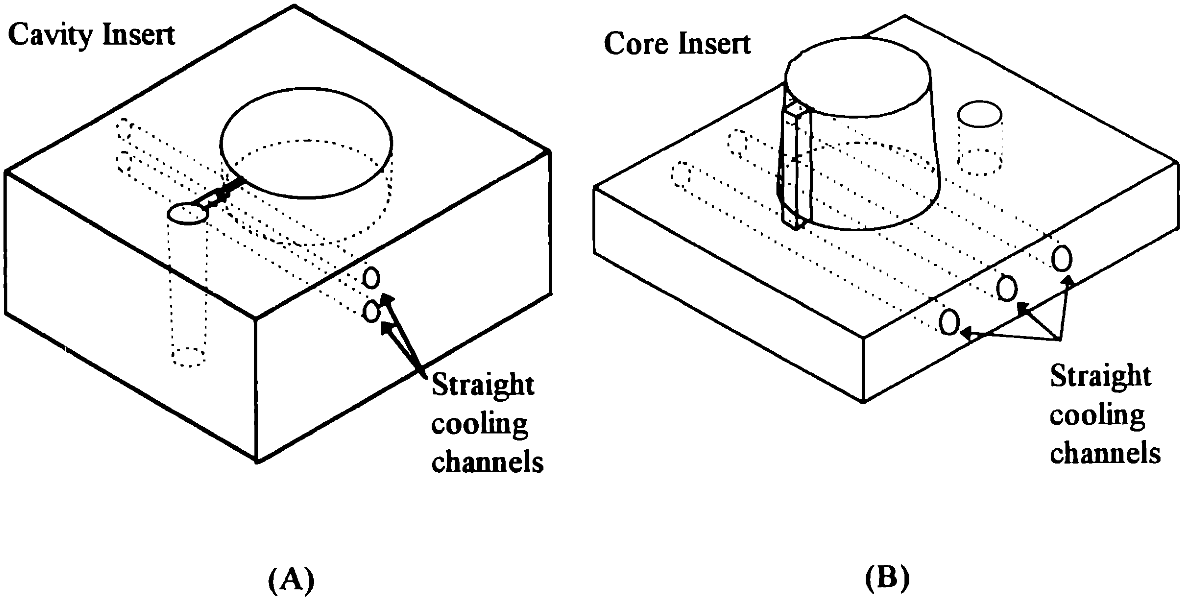

Figure 4.5: Cooling channel placement in the 303 stainless steel cavity (A) and core (B) inserts.

4.4 Conformal Channel Design in 3D Printed Inserts

Figure 4.6 depicts the infiltrated and machined 3D Printed cavity and core inserts with conformal cooling channels. A polystyrene ring molded with these inserts in also shown. Schematics of the cooling channel placement in these inserts are shown in Figure 4.7. Figure 4.8 is a photograph of two 3D Printed infiltrated core inserts. One insert has been cut open to reveal the conformal channels inside.

Two separate conformal channels were designed in the 3D Printed cavity insert. Each separate channel splits 1/8 inch from the cavity wall into two channels. These two channels follow the circular shape of the cavity wall and converge to one exit channel. This channel placement forms a torus shaped passage surrounding the molding cavity. This torus shape keeps the channels 1/8 inch from the molding surface along the entire perimeter of the cavity. All channels are circular in cross-section and have a diameter of

3/16 inch matching the straight channels in the 303 stainless steel inserts. The two torus shaped channels were spaced evenly along the depth of the cavity.

As in the 3D Printed cavity design, two torus shaped channels were horizontally spaced along the height of the core. Again, the torus shape keeps the channels 1/8 inch from the molding surface along the entire perimeter of the core. A single horizontal channel open on the side of the base of the insert connects with a vertical channel underneath the core. This vertical channel intersects the two torus shaped channels. An identical channel path on the opposite side of the core provides a channel exit. A summary of the coolant path is as follows: the coolant enters through one side of the base of the core and flows up to the two torus shaped channels. The coolant then splits four ways moving around the surface of the core. The four channels converge again into one channel that exits on the other side of the core.

Figure 4.7(A) - (B) depicts the printed placement of the cooling channels in the 3D Printed cavity and core inserts. Detailed dimensions of channel placement in the 3D Printed inserts is depicted in machine drawings in Appendix D.

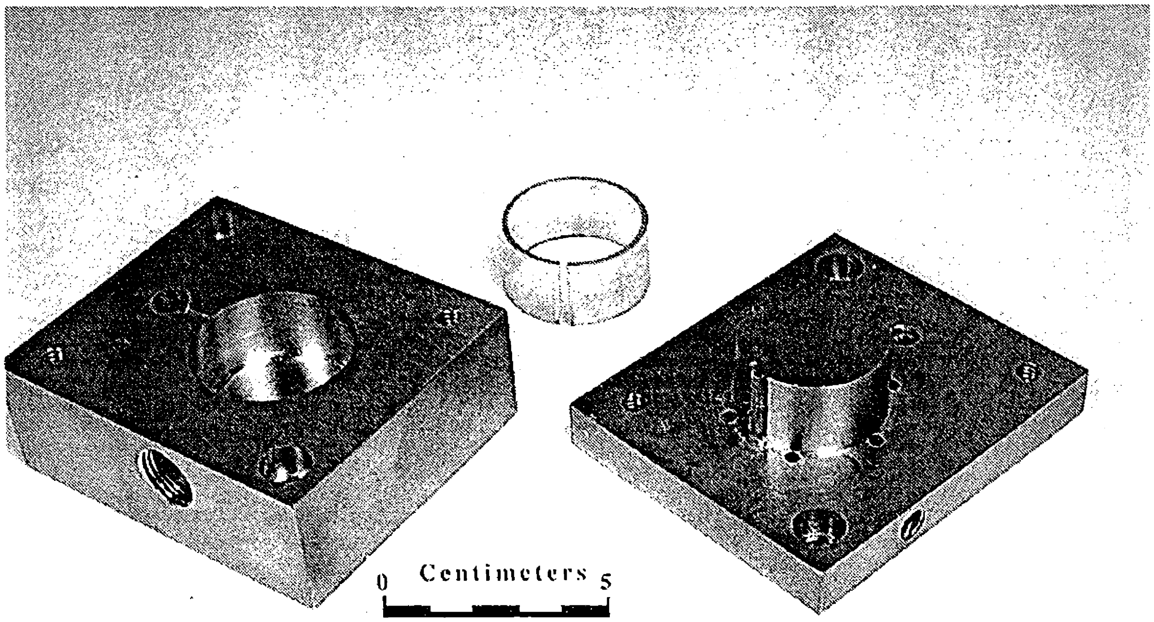

Figure 4.6: Infiltrated and machined 3D Printed cavity and core inserts with conformal cooling channels.

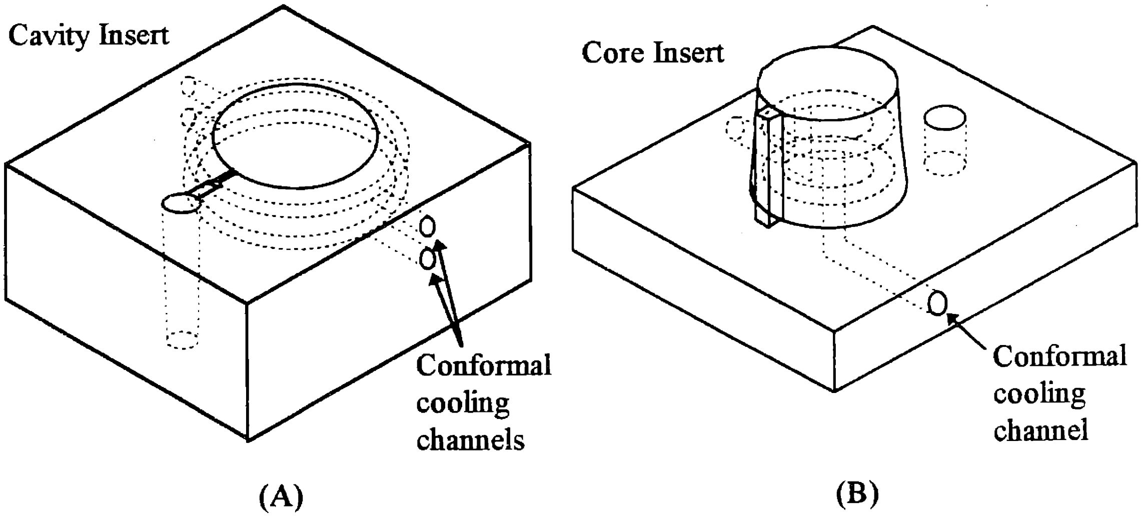

Figure 4.7: Cooling channel placement in the 3D Printed cavity (A) and core (B) inserts.

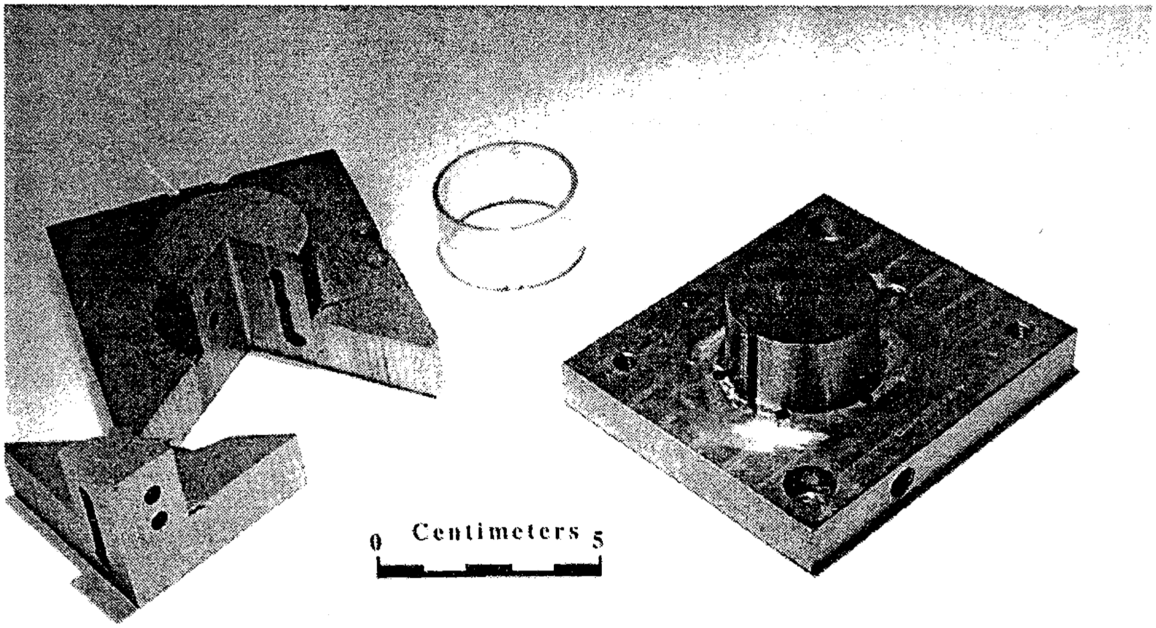

Figure 4.8: Infiltrated and machined 3D Printed core insert (right) and an infiltrated core insert that has been cut open to reveal the conformal cooling channels. (left)

Conformal channel placement in the 3D Printed inserts was designed based on the results of a finite difference simulation to be discussed in Chapter 6. This design simply places the conformal channels a constant distance (1/8 inch) from the molding surface. This distance was chosen to allow thermocouple holes to be drilled between the channels and the molding walls. Figure 4.9 depicts a cross-section of the mating core and cavity inserts at the center of the circular cavity.

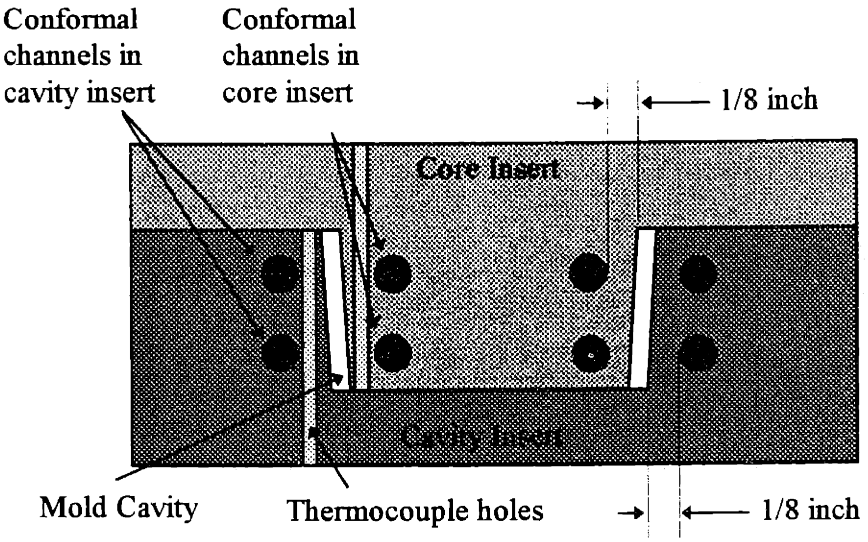

Figure 4.9: Cross-section of the mating 3D Printed core and cavity inserts.

5. Experimental Results

This chapter describes the results of experiments conducted. Experiments designed to characterize the distortion in the plastic rings are explained. Mold surface temperature data collected for the inserts with straight channels and the inserts with conformal channels is then discussed. Finally, the effect of varying relative coolant temperature in the cavity and core inserts is explained.

5.1 Characterization of Distortion in Polystyrene Parts

Polystyrene parts were molded with the stainless steel inserts containing straight cooling channels. It was observed that the rings naturally close to a gap width of approximately 0.6 mm. This value may be compared to the core rib dimension of 2.18 mm. It was hypothesized that the mold surface temperature or thermal properties of the stainless steel material could have an effect on the part gap width. This section will describe two simple experiments conducted to reveal insight on part distortion.

5.1.1 Effect of Mold Surface Temperature on Part Distortion

A simple experiment was conducted to determine the effect on the ring gap width of the relative molding surface temperature difference between the core and cavity insert halves. The stainless steel inserts were used to mold a series of "first shots". The molding surface of the core insert was heated with a heat gun to over 100°C. The molding surface of the cavity insert was left at room temperature. In this case the gap closed completely.

The insert temperatures were then reversed. The molding surface of the core insert was left at room temperature while heat was applied to the molding surface of the cavity insert. In this case the part gap opened to a width of over 1 cm.

A hypothesis was made as to why the gap in the ring parts open or close depending on the relative temperature of the core versus the cavity mold surface temperature. We will consider the case where the mold surface of the core is very hot and the mold surface of the cavity is cool. We will also make an assumption that the thickness of the ring may be divided into two separate regions. One side of the ring is effected by the mold surface temperature of the core and one side of the ring is effected by the mold surface temperature of the cavity. This idea is depicted in Figure 5.1 below.

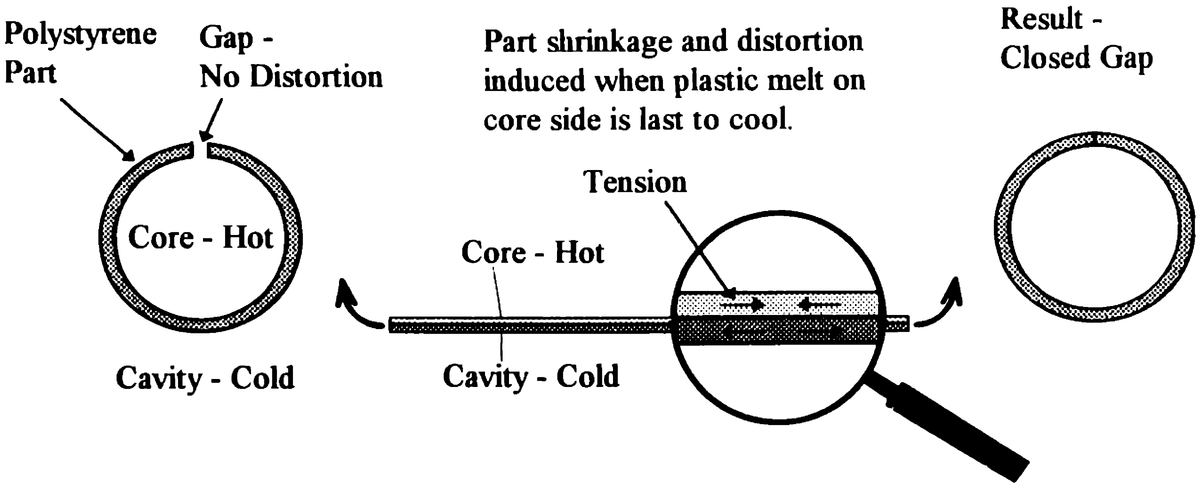

Figure 5.1: Polystyrene ring - gap distortion.

As the plastic flows into the mold, the melt near the cavity surface freezes before the melt near the core surface due to the lower cavity surface temperature. In this scenario the cavity half of the plastic ring has solidified before the core side. The last side to cool (core side) shrinks compared to the already solidified cavity side. This creates a tension on the core side which "pulls" the ring closed.

This hypothesis explains the wider molded part gap resulting from a molding condition in which the cavity insert surface temperature is hotter than the core insert temperature. In this case the cavity plastic part half cools last creating a shrinkage on the outside of the ring resulting in a wider part gap.

5.1.2 Effect of Thermal Properties of Mold Material on Part Distortion

An experiment was conducted to determine whether the thermal properties of the stainless steel material are a possible cause of the rings closing. Inserts were machined out of aluminum that were identical to the stainless steel inserts. A set of experiments was conducted in which polystyrene parts were molded using the core and cavity aluminum inserts, core and cavity steel inserts and combinations of the two. All tests were conducted without cooling to isolate the effect of material on the transfer of heat and buildup of distortion in the ring. Each time a part was collected in these experiments the mold was allowed to cool to room temperature. Every part was a "first shot". This was done to eliminate the possibility of the aluminum insert temperatures drifting upward to a different overall temperature than the stainless steel inserts.

The width of the gap in the polystyrene rings was measured using an optical microscope. The actual rib size is 2.18 mm. Fifteen rings were molded for each combination of the insert pairs tested. Table 5.1 below depicts the results of these experiments.

	Aluminum Core Aluminum Cavity	Steel Core Steel Cavity	Aluminum Core Steel Cavity	Steel Core Aluminum Cavity
Average Gap Width (mm)	0.776	0.673	1.137	Gap Closed
Standard Deviation	0.078	0.057	0.050	Gap Closed

Table 5.1: Gap width measurements for different combinations of aluminum and stainless steel inserts.

The results of these experiments indicate that rings molded with the aluminum inserts do not close as much as those molded with the stainless steel inserts. The rings close significantly less when an aluminum core and a steel cavity is used. When a steel core and an aluminum cavity is used the gap in the ring parts closes completely.

It is hypothesized that the relatively low thermal diffusivity of the stainless steel material as compared to the aluminum material hinders the flow of heat into the mold surface. Table 5.2 is a comparison of thermal properties of stainless steel and aluminum.

Material	Density, ρ (kg/m^3)	Specific Heat, c_p (J/kg-°C)	Thermal Conductivity, k (W/m-°C)	Thermal Diffusivity, α (10-5 m^2/s)
303 Stainless Steel	8000	400	13.8	0.4
Aluminum	2707	905	237	9.61

Table 5.2: Properties of 303 stainless steel and aluminum at 20°C. [Lienhard, 1987]

The thermal diffusivity is a measure of how quickly a material can carry heat away from a hot source. [Lienhard, p. 15, 1987] The results demonstrate that heat is carried away from the ring much faster if the mold surface is aluminum. There is more material volume in the cavity insert than the core insert for heat withdrawal. Figure 5.2 is a cross section of the mating core and cavity mold pair forming the mold cavity. This figure shows lines indicating the heat conduction paths in the cavity and the core inserts.

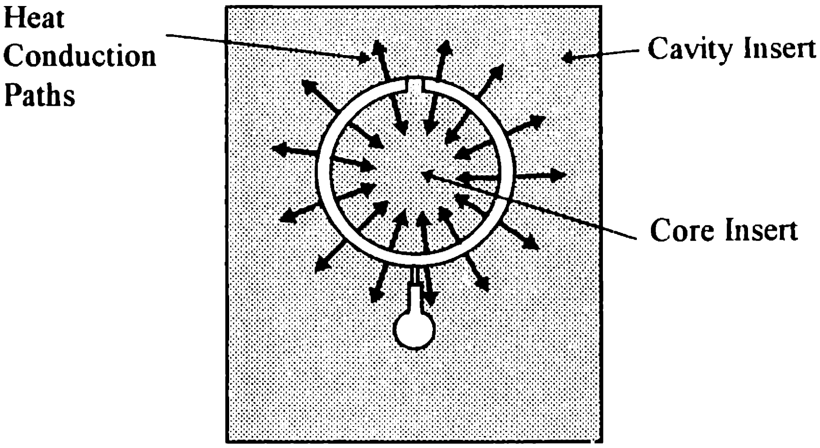

Figure 5.2: Cross section of the core and cavity mold pair forming the mold cavity. Arrows indicate the heat conduction paths in the cavity and the core inserts.

The heat conduction paths in the cavity radiate from the molten plastic heat source while the paths in the core insert converge. Heat is carried away faster in the cavity than the core insert and a temperature difference between the two surfaces during the injection cycle is created.

The "last part half to cool" hypothesis may be used to explain the results of the aluminum vs. steel experiments. When an aluminum core insert and a steel cavity insert are used to mold a ring, heat diffuses more slowly through the cavity than the core insert because of the relatively lower thermal diffusivity of steel compared to aluminum. This causes the cavity part half to cool last inducing shrinkage on that side. Thus, the part gap width is larger than when the part is molded with two insert halves of the same material (Table 5.1). When a steel core insert and an aluminum cavity insert are used to mold a part, the core side part half is the last half to cool and the gap closes completely.

5.2 Mold Surface Temperature

The preceding study of the effect of the mold surface temperature on the ring gap width fostered interest in characterizing the surface temperature of the mold in the injection cycle. The following section describes mold surface temperature measurements made for both the inserts with straight channels and the 3D Printed inserts with conformal cooling channels.

5.2.1 Experimental Setup

An Engel EC88, 30 ton injection molding machine located at MIT was used to mold the polystyrene parts with the stainless steel inserts and the 3D Printed inserts. Melt temperature and injection pressure were 215°C and 1000 psi, respectively in all experiments. Approximately 25 - 30 polystyrene parts were injection molded in a single run.

Two 40 Gallon water heaters were used to hold coolant water. These water heaters included a thermostat that could be set between 125 F and 170 F. The tanks were connected to a pressurized tank of nitrogen. Once the temperature of the coolant water stabilized, the tank could be pressurized as needed to provide a given flow rate. In all experiments the flow rate through each insert side (cavity - core) was 1.3 gal/min. This flow rate was chosen to approximately match the maximum flow rate obtainable from the city water (cold tap water) supply.

A thermocouple was placed in the inlet tube and the outlet tube of the inserts, to accurately measure the temperature of the coolant water entering and exiting the mold. In order to measure the temperature of the molding surface, three thermocouples were placed in the cavity and the core inserts. Thermocouple holes 0.0625 inches in diameter were drilled such that the closest edge of the hole was less than 0.015 inches from the mold surface at the mid point of the height of the ring. One thermocouple was placed near the gate, one near the rib and one in-between the gate and the rib. The thermocouples were placed in the holes with a highly thermally conductive paste. Figure 5.3 describes the thermocouple placement in the core and cavity inserts.

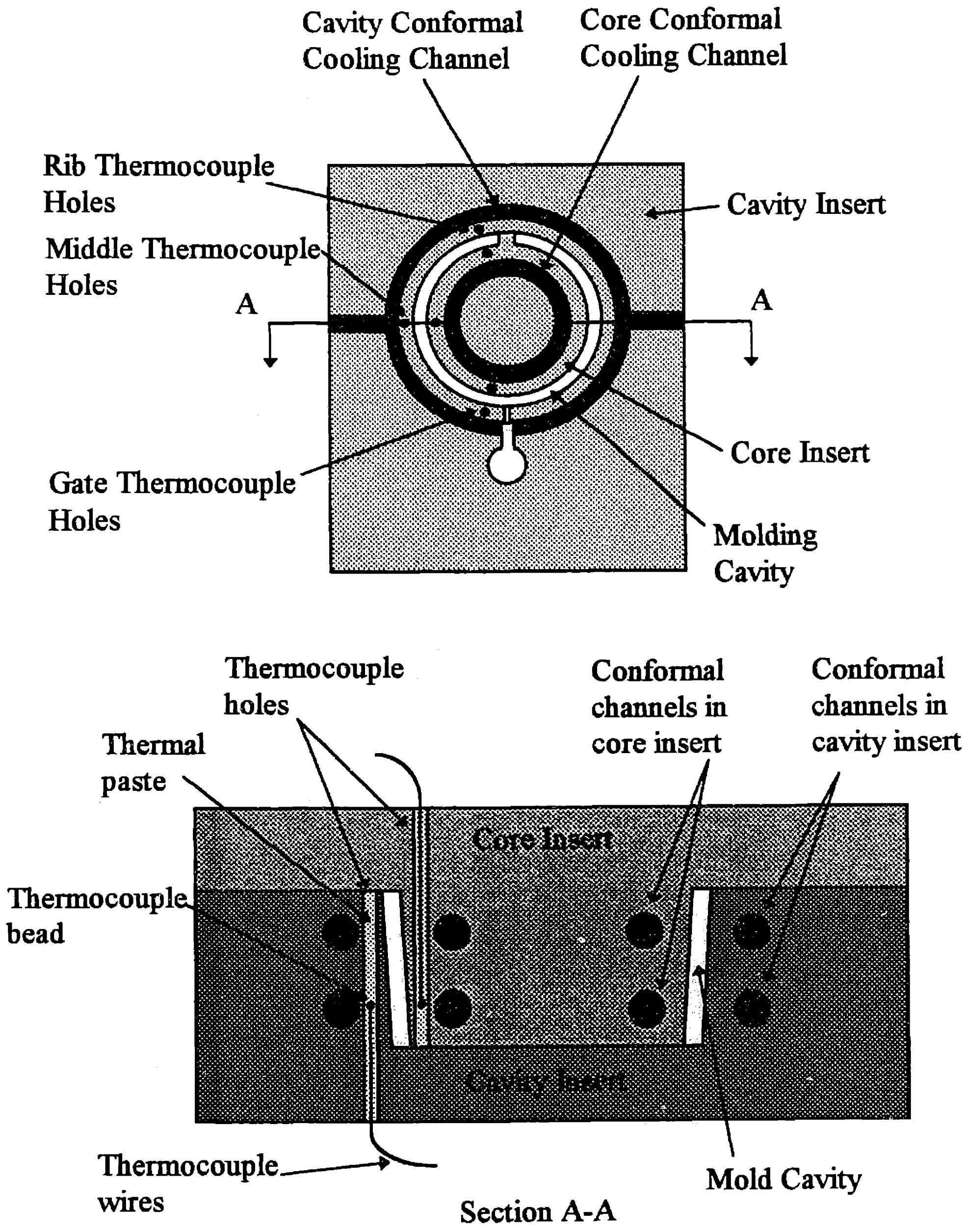

Figure 5.3: Thermocouple placement in cross sections of the core and cavity mold pair forming the mold cavity.

An Apple Macintosh II computer with thermocouple to analog converters (Omega TAC 80J - 1mV/Degree) and a LabView Analog NB data acquisition board was used to collect the temperature data. Figure 5.4 depicts the experimental set-up for mold surface temperature data collection.

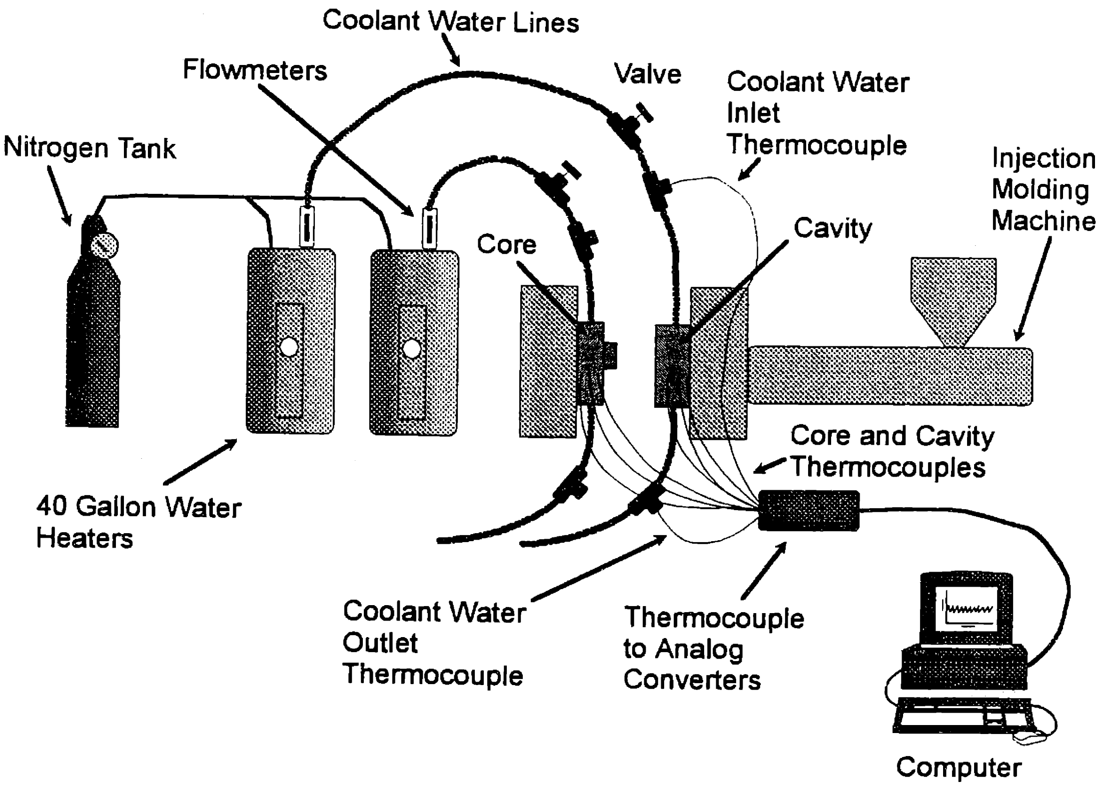

Figure 5.4: Experimental set-up for mold surface temperature measurements.

5.2.2 Mold Surface Temperature Experiments for Inserts with Straight Channels

Mold surface temperature measurements were made for the 303 stainless steel inserts with straight channels. The coolant temperature was approximately 11 °C in both of these injection molding runs. A cycle time of approximately 11 seconds was used for all experiments. Figure 5.5 shows the mold surface temperature near the gate, middle and rib for the core insert.

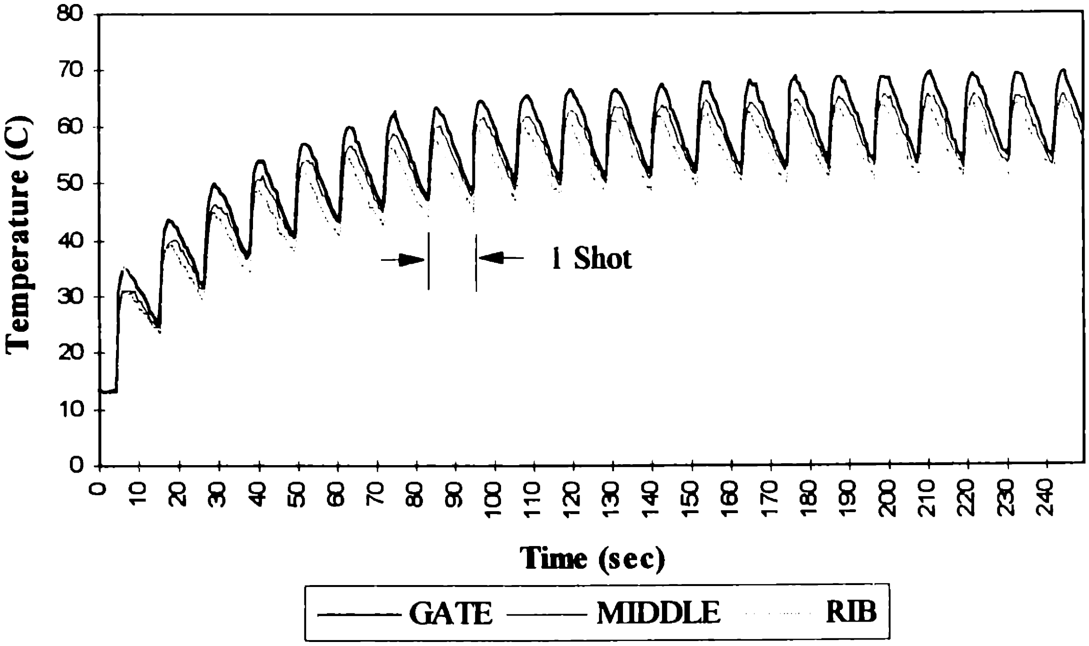

Figure 5.5: Mold surface temperature vs. time for core insert (straight channels) coolant temperature ≈ 11 °C.

Figure 5.5 depicts the core surface temperature of the 303 stainless steel inserts with straight channels during an injection molding run. Notice the cyclic variation in temperature. Each cycle in this temperature profile represents one shot. For each shot the temperature rises quickly during the filling stage because the polystyrene plastic is very hot. This filling stage takes approximately 1.0 second. The mold surface temperature drops during the 6.5 second cooling stage. Finally the mold is opened and the part is ejected. This open stage takes approximately 3.5 seconds. During this stage the mold is still cooling. The mold closes again and the cycle starts over. Figure 5.6 is an enlargement of one injection cycle (after the upward cycle drift has leveled off) in figure 5.5 depicting the timing of the three stages.

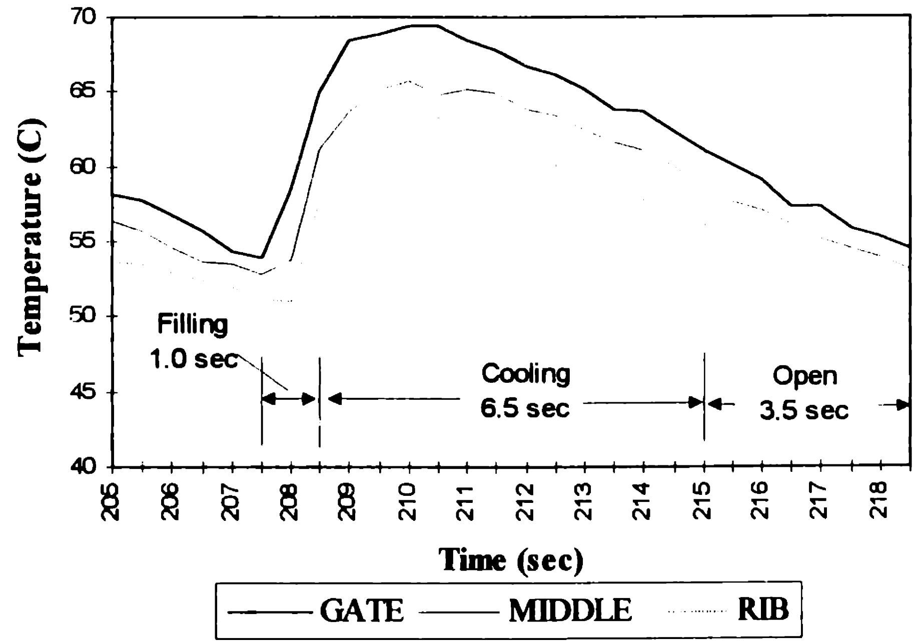

Figure 5.6: Mold surface temperature vs. time for core insert showing timing of filling, cooling and open stages in injection cycle.

There is a significant upward drift in the surface temperature during the injection molding run for the core insert with straight channels. After the first cycle is completed the overall temperature of the mold surface rises. The buildup of heat in the mold surface material cannot be dissipated in the allotted cooling time. The cooling channels are relatively far from the molding surface and cannot remove heat from the molding surface fast enough because of the low thermal diffusivity of the stainless steel material. The observed upward drift in mold surface temperature levels off after 15 - 20 shots.

Another important observation from the mold surface temperature data is the difference in temperature of the surface along the perimeter of the ring. In each cycle at any given moment the temperature of the molding surface at the gate is higher than the surface temperature near the rib. The middle thermocouple shows a surface temperature in between these two temperatures. This occurrence is a result of the molten polymer entering the molding cavity at the gate. The molten polymer is very hot as it enters and cools as it moves along the perimeter of the ring to fill the entire cavity. In addition the plastic melt is in contact with the mold surface near the gate for a longer period of time than it is with the surface near the rib. The combination of these two effects explains the higher mold surface temperature near the gate than the rib.

Figures 5.7 shows the mold surface temperature near the gate, middle and rib for the cavity insert.

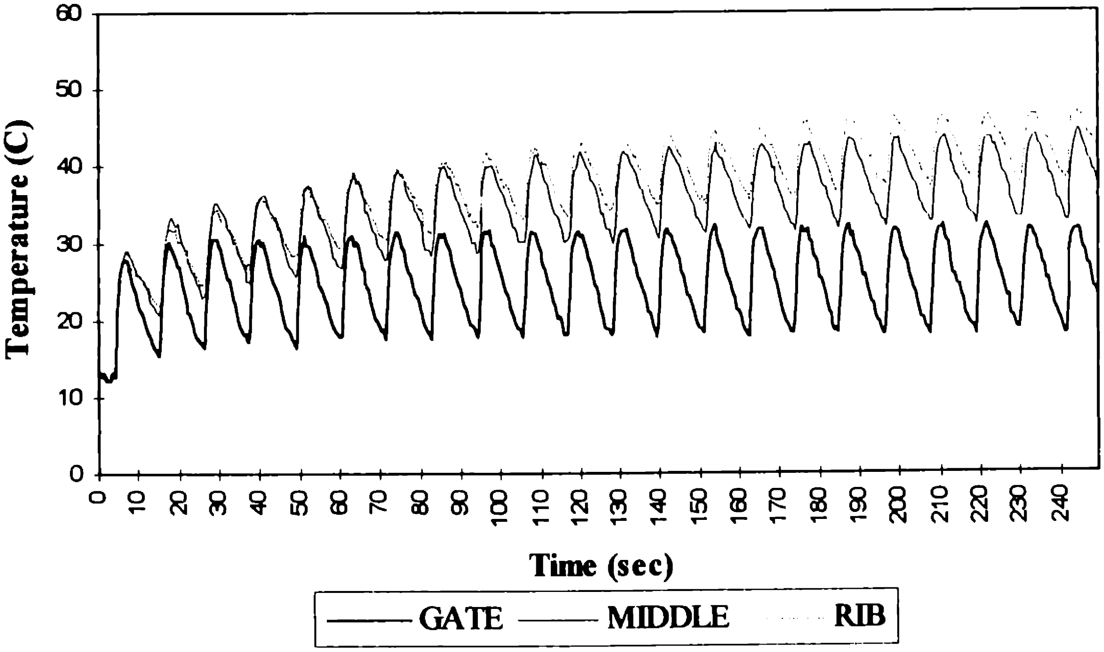

Figure 5.7: Mold surface temperature vs. time for cavity insert (straight channels) coolant temperature ≈ 11 °C.

It is evident in figure 5.7 that the mold surface temperature along the perimeter of the ring is quite non-uniform. There is a significant difference in mold surface temperature at the gate than at the rib. The mold surface temperature in the middle and at the rib end drift upward significantly while the mold surface near the gate end only drifts a little. This fact can be explained by the cooling channel placement in the 303 stainless steel cavity insert. Figure 4.7(A) depicts the placement of the cooling channels in this cavity insert. The straight channels are positioned very close to the mold surface near the gate end of the perimeter of the ring part. This placement creates an extremely non-uniform molding surface as heat is removed much faster near the gate end than the rib end.

Even though a fully conformal channel design is not possible by machining, additional straight channels could have been drilled in the stainless steel cavity insert to improve surface temperature uniformity. The channel design in the cavity insert was chosen to exemplify the potentially large surface temperature variance that is possible when a very simple straight cooling channel design is employed.

5.2.3 Mold Surface Temperature Experiments for Inserts with Conformal Channels

The following surface temperature data was collected using the 3D Printed injection molding inserts with conformal cooling channels. A coolant temperature of approximately 11 °C was used in these experiments. Again, a cycle time of approximately 11 seconds was used for all experiments. Figure 5.8 shows the mold surface temperature near the gate, middle and rib for the 3D Printed core insert.

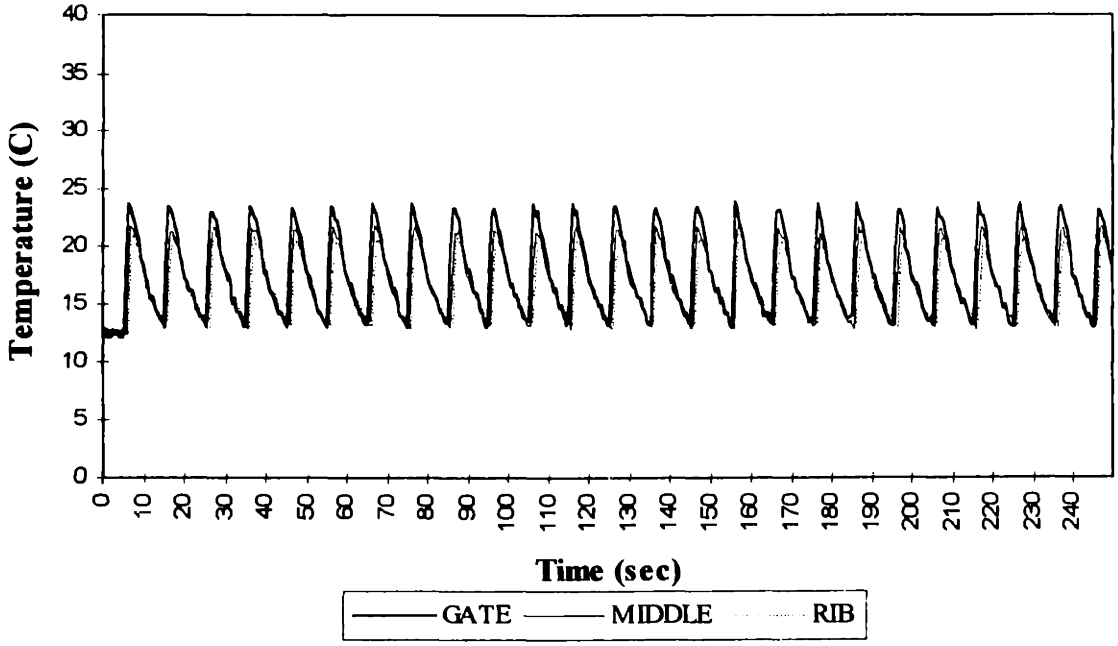

Figure 5.8: Mold surface temperature vs. time for core insert (conformal channels) coolant temperature ≈ 11 °C.

Figure 5.9 below depicts an enlargement of the surface temperature plot for one cycle:

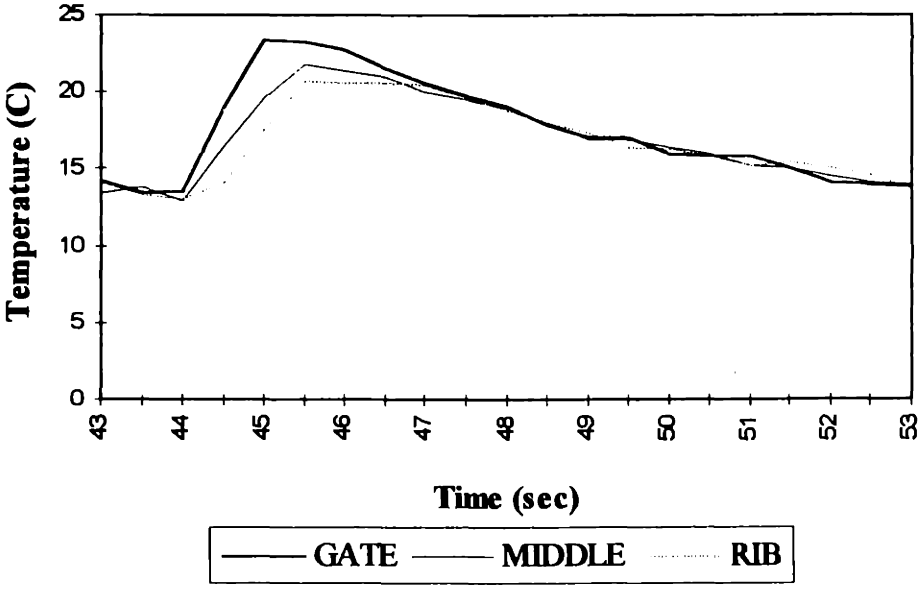

Figure 5.9: Mold surface temperature vs. time for one cycle - core insert (conformal channels)

Several important observations may be made from the surface temperature measurements depicted in figures 5.8 and 5.9. A significant improvement in mold surface temperature control is evidenced by the absolute absence of any drift in temperature from cycle to cycle. Also the temperature of the mold surface along the perimeter of the ring is more uniform. At the beginning of the cooling stage of the cycle there is approximately a 4 degree difference in temperature between the molding surface near the gate end and rib end. This compares to a 7 degree temperature difference in the core insert with straight channels evidenced in figure 5.6.

Figure 5.10 shows the mold surface temperature near the gate, middle and rib for the 3D Printed cavity insert.

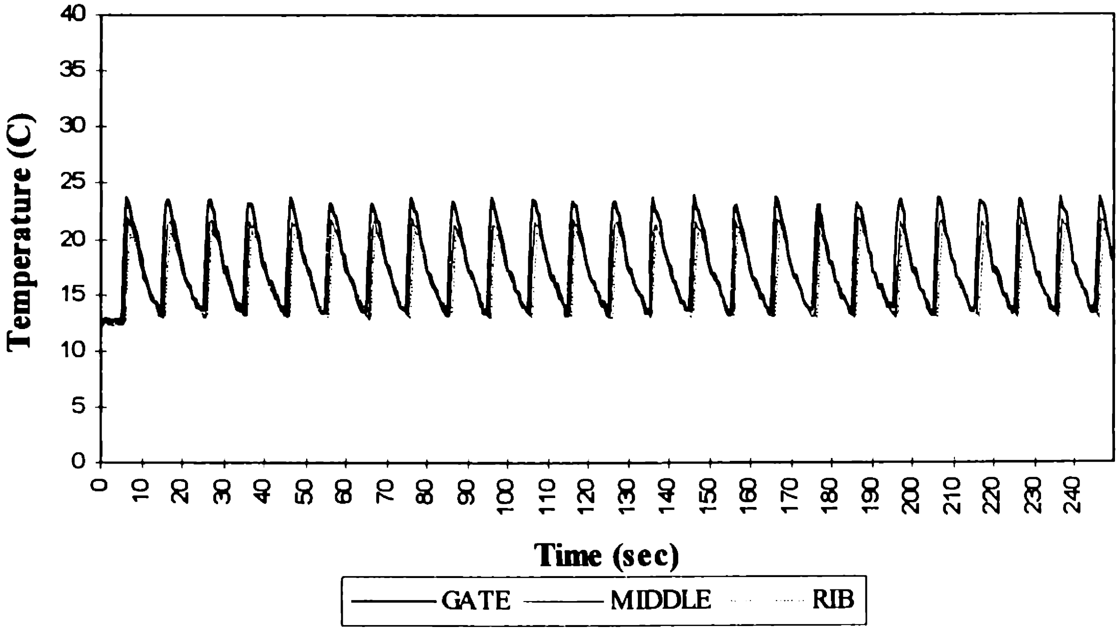

Figure 5.10: Mold surface temperature vs. time for cavity insert (conformal channels) coolant temperature ≈ 11 °C.

Inspecting the 3D Printed cavity mold surface temperature, significant improvement in mold surface temperature control is demonstrated by the absolute absence of any drift in temperature from cycle to cycle. As with the 3D Printed core insert the temperature of the mold surface along the perimeter of the ring is noticeably more uniform. At the beginning of the cooling stage of the cycle there is only a 4 degree difference in temperature between the molding surface near the gate end and rib end. This compares to a 10-15 degree temperature difference in the cavity insert with straight channels evidenced in figure 5.7.

Comparing the surface temperature of the 3D Printed core and cavity inserts (figures 5.8 and 5.10) we observe a similarity of surface temperature throughout the injection molding run. This indicates the core and cavity are approximately at the same temperature at any point in the mold cycle. These facts serve to indicate that the 3D Printed insert surface temperature history of the first shot is the same as that of the 30th shot or 100th shot.

The relative surface temperatures of the 303 stainless steel core and cavity inserts with straight channels start off at the same temperature. However, after 30 shots the surface temperature in the core and cavity inserts drift apart. These large temperature differences between the core and cavity inserts can build residual stresses in the part. The first 20-30 parts in the injection molding run will also have noticeably different dimensional characteristics due to the ever changing surface temperature. In industry these molds would have to be run possibly for an hour or more to ensure dimensional stability from one shot to the next.

General observations made in comparing the mold surface temperature histories for injection molding runs using the 303 stainless steel inserts with straight channels and the 3D Printed inserts with conformal channels are summarized below.

1. A significant upward drift in surface temperature is observed using the stainless steel inserts with straight channels.
2. No noticeable drift in surface temperature is observed throughout the injection molding run using the 3D Printed inserts with conformal channels.

3. The magnitude of the mold surface temperature swing during the injection molding cycle is larger for the inserts with straight channels than the inserts with conformal channels.
4. The difference in temperature along the perimeter of the core or cavity molding surface (difference in temperature at gate end vs. rib end) is lower in magnitude when using the inserts with conformal channels than when using the inserts with straight channels. This difference in magnitude is measured at the beginning of the cooling stage in the molding cycle.

5.2.4 Mold Surface Temperature Experiments with Higher Coolant Temperatures

Experiments were conducted to determine the effect of the coolant water temperature on the mold surface temperature in the stainless steel inserts with straight channels and the 3D Printed inserts with conformal channels. Three temperatures of coolant water were used, 11°C, 25°C and 54°C (± 2 °C). In all experiments the inserts were allowed 15 - 25 min. for the insert temperatures to equilibrate to the new coolant temperatures. Each of the polystyrene parts were collected for later inspection. Mold surface temperature data was obtained for both pairs of inserts and for each temperature of coolant water. Data was obtained for runs in which the cavity insert and core insert coolant temperatures were the same and in which they were different. Nine injection molding runs, using all combinations of the three different coolant temperatures, were completed for each set of inserts (straight channels and conformal channels). Eighteen injection molding runs were executed in all. Figures 5.11 and 5.12 show the mold surface temperature history using 54°C coolant in both insert sides for the core insert with straight channels and the core insert with conformal channels.

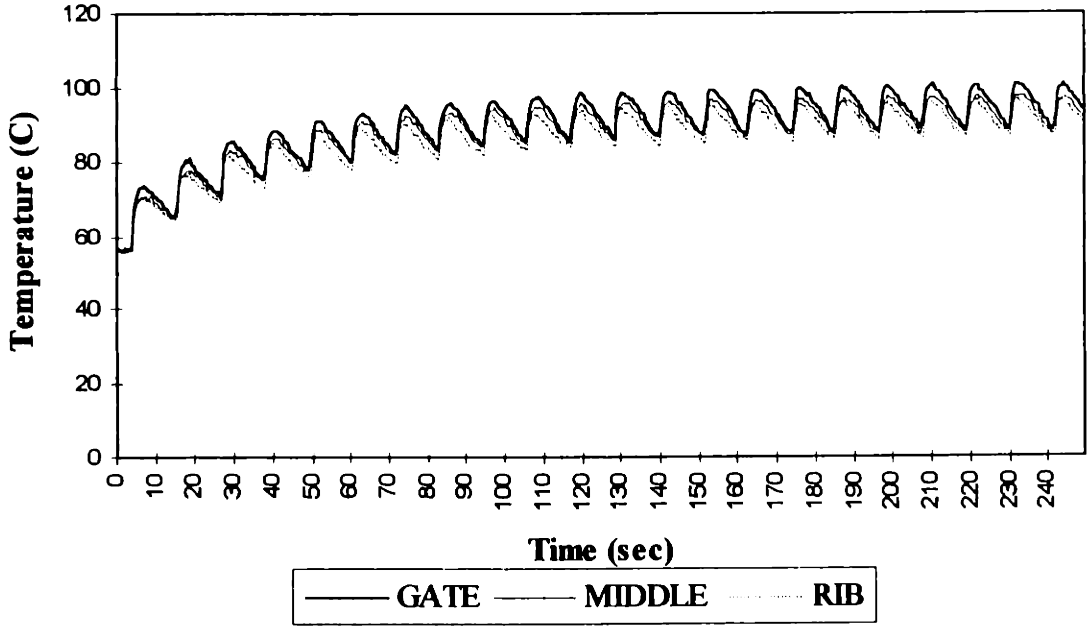

Figure 5.11: Mold surface temperature vs. time for core insert (straight channels) coolant temperature ≈ 54 °C.

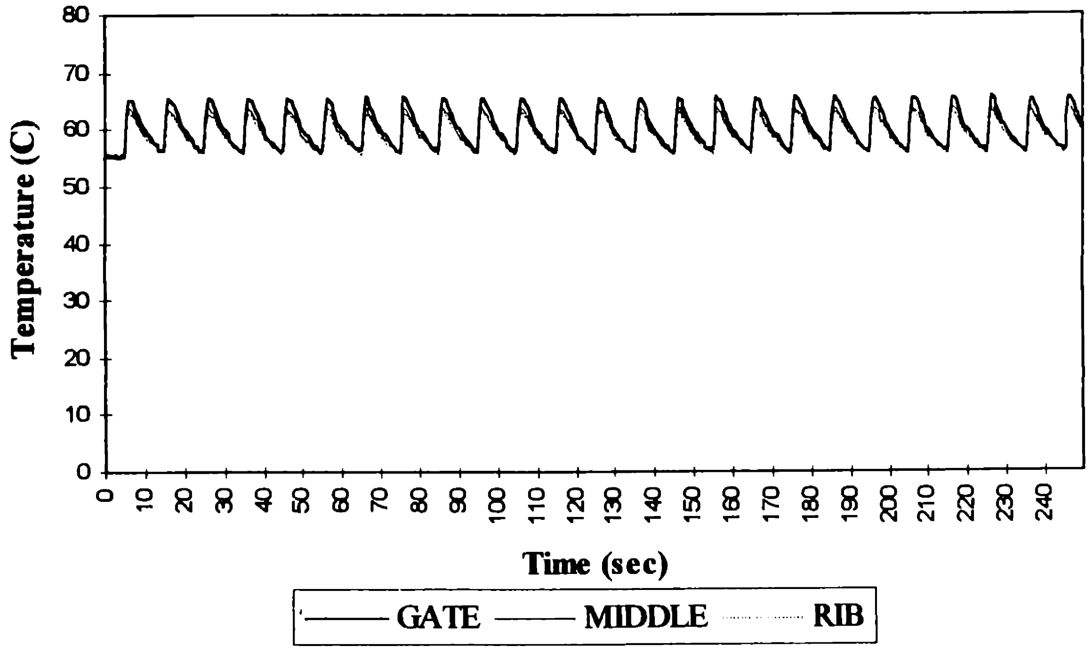

Figure 5.12: Mold surface temperature vs. time for core insert (conformal channels) coolant temperature ≈ 54 °C.

Observations of the mold surface temperature histories for varied coolant temperatures are as follows:

1. An upward temperature drift occurs during the injection molding run using the inserts with straight channels for each coolant temperature (11 °C, 25 °C, and 54 °C).
2. The magnitude of the temperature drift decreases slightly as the coolant temperature used for the injection molding run is increased. For example, a 38 °C core surface temperature drift occurs using a coolant temperature of 11 °C. A 30 °C temperature drift occurs using a coolant temperature of 54 °C.
3. No surface temperature drift is observed for any coolant temperature using the inserts with conformal channels. Increasing the coolant temperature in the inserts with conformal channels simply shifts the overall surface temperature plots upward.
4. The magnitude of the mold surface temperature swing in a cycle is not significantly affected by the coolant temperature. This is observed for both the inserts with straight channels and the inserts with conformal channels.
5. The surface temperature throughout the molding cycle of one insert side (cavity or core) is affected by the temperature of the coolant running through that side. It is not affected by the temperature of the coolant running through the other insert side. For example, when the 3D Printed cavity insert coolant temperature is 25°C and the core is 54°C the cavity insert surface temperature history is approximately the same as if the core insert coolant temperature was 11°C or 25°C.

5.3 Effect of Varying Relative Insert Temperatures on Part Gap Width

As mentioned previously the polystyrene parts in every injection molding run were collected. An investigation into the effect of the relative insert temperatures on the part gap width was conducted after the completion of the injection molding runs. The gap width of the parts was measured using an optical microscope and a micrometer table. Figure 5.13 below describes the results of the gap width measurements for two injection molding runs. One run was made using the stainless steel inserts with straight cooling channels and the other run was made using the 3D Printed inserts with conformal channels. The coolant temperature running through the cavity and core in each case was 11°C. The actual width of the rib on the core inserts is 2.18 mm.

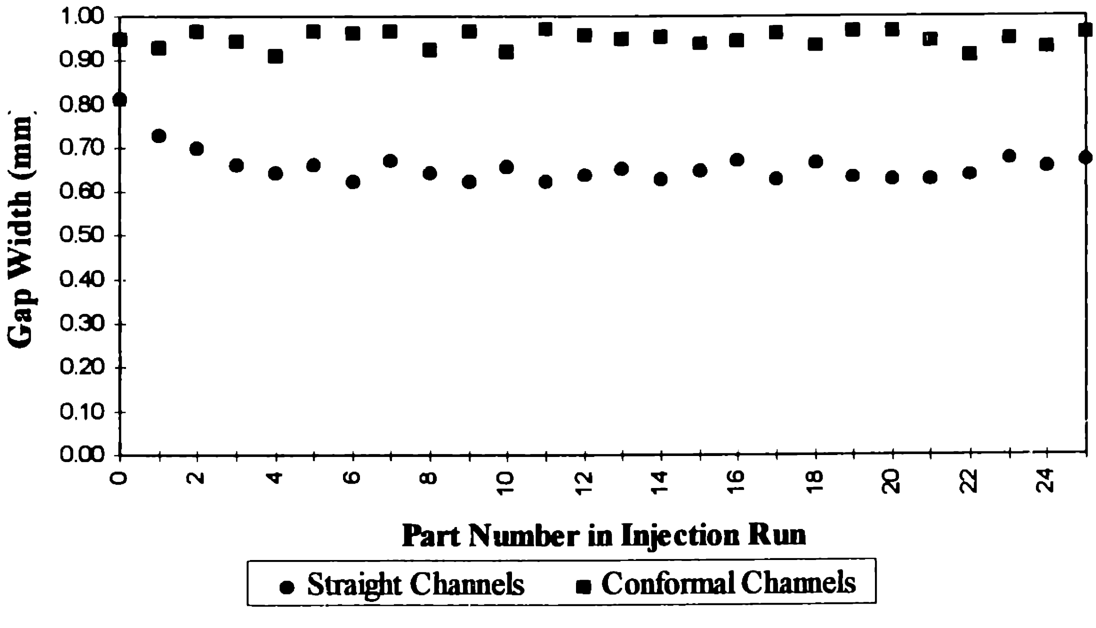

Figure 5.13: Gap width vs. part number in injection run / cavity and core coolant temperature ≈ 11 °C / actual gap width = 2.18 mm.

The results of this study show that the gap width changes during the injection molding run when the stainless steel inserts with straight channels are used. The first 5 or 6 molded parts show a downward drift in gap width. The parts molded with the 3D

Printed inserts show no drift in dimension of the gap width. In both cases the rings do close as compared to the actual rib width of the core.

As discussed in section 5.1.1 the gap width is sensitive to the relative mold surface temperature of the cavity versus the core insert. Figure 5.14 below describes the results of the gap width measurements for two more injection molding runs. Again, one run was made using the stainless steel inserts with straight cooling channels and the other run was made using the 3D Printed inserts with conformal channels. In this experiment the coolant temperature running through the cavity insert was 54 °C while the coolant running through the core insert was 11°C.

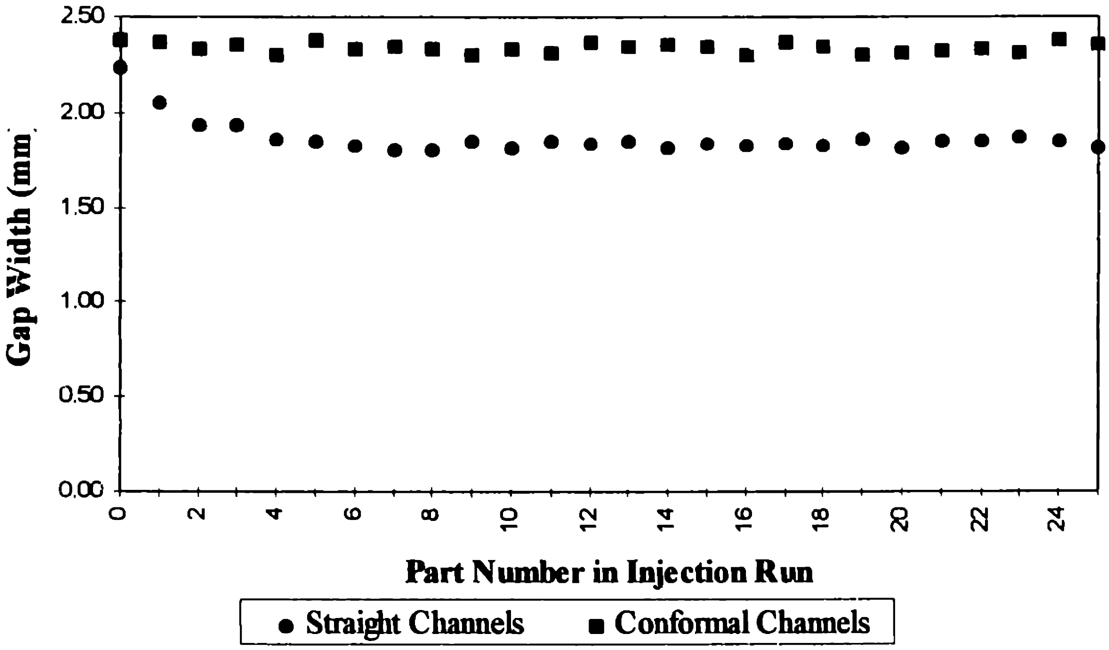

Figure 5.14: Gap width vs. part number in injection run / cavity coolant temperature ≈ 54 °C / core coolant temperature ≈ 11 °C / actual gap width = 2.18 mm.

Again, the gap width changes during the injection molding run when the stainless steel inserts with straight channels are used. The parts molded with the 3D Printed inserts show no drift in dimension of the gap width. The gap width of the parts molded under these conditions remained rather large. This is due to the large difference in overall temperature between the cavity and the core molding surface temperature.

In figure 5.14 the cavity surface temperature was much hotter than the core surface temperature. In this case the cavity side (outer side) of the part was the last to cool. Thus the gap opened. In the injection molding runs in which the core insert coolant temperature was hotter than the cavity insert temperature, the gap in the polystyrene parts closed completely.

Table 5.3 and 5.4 describe the average gap width obtained using the different combinations of coolant temperatures investigated. Twenty six parts were measured for each data set.

		Cavity Insert		
		11 °C	25 °C	54 °C
Core Insert	11 °C	0.66 mm Avg 0.04 mm St. Dev	0.93 mm 0.06 mm	1.86 mm 0.09 mm
	25 °C	0.0 mm -	0. 60 mm 0.05 mm	1.22 mm 0.08 mm
	54 °C	0.0 mm -	0.0 mm -	0.68 mm 0.06 mm

Table 5.3: Average part gap width for different coolant temperatures. (Parts molded using 303 stainless steel inserts with straight channels)

		Cavity Insert		
		11 °C	25 °C	54 °C
Core Insert	11 °C	0.95 mm Avg 0.02 mm St. Dev	1.38 mm 0.03 mm	2.34 mm 0.02 mm
	25 °C	0.0 mm -	1.05 mm 0.03 mm	1.65 mm 0.03 mm
	54 °C	0.0 mm -	0.0 mm -	0.93 mm 0.02 mm

Table 5.4: Average part gap width for different coolant temperatures. (Parts molded using 3D Printed inserts with conformal channels)

A brief summary of the observations made in these experiments follows:

1. The gap width remains constant from the first shot to the next throughout the injection molding run when using the 3D Printed inserts with conformal cooling channels.
2. The gap width drifts to a lower steady state dimension during the injection molding run when using the stainless steel inserts with straight channels.
3. The width of the gap in the polystyrene rings is a function of the relative surface temperature between the core and cavity mold surface. The rings may be made to close or open by varying the relative coolant temperatures running through the two insert sides (core and cavity).
4. When the coolant running through the cavity and core inserts is at the same temperature, the measured ring gap is significantly less than the rib on the core that creates this gap. This is true for the inserts with straight channels and the 3D Printed inserts with conformal channels.
5. When the coolant running through the cavity insert is significantly hotter than the coolant running through the core insert, the measured gap width is increased. When the coolant running through the cavity insert is significantly

colder than the coolant running through the core insert, the measured gap closes.

6. Finite Difference Simulations

A description of the finite difference simulation used to determine optimal placement of conformal channels in the tooling is presented. The overall theory behind the numerical simulation and a brief description of the computer implementation is discussed. Finally, finite difference simulations of the mold surface temperature of the 3D Printed inserts with conformal cooling channels is shown.

6.1 Finite Difference Model

A method of predicting the performance of various conformal cooling channel designs was required to develop the final conformal channel design for the 3D Printed inserts. A numerical approach to this heat transfer problem was taken. This section will describe the finite difference simulation used to develop a design for the conformal passages in the 3D Printed inserts.

6.1.1 Numerical Approach

A method of predicting the thermal behavior of a mold with conformal cooling channels was needed to design the 3D Printed injection molding inserts. Analytical methods may be used to calculate temperatures in certain regular shaped solids under transient heat-flow conditions. However, the transient boundary conditions as well as the geometric shape of the body can be of such form that a mathematical solution is extremely difficult. A model of an injection molding process poses a problem in which the boundary conditions vary with time. In this case, the problem is best handled by a numerical technique.

A 2-Dimensional finite difference approach was chosen. A program was written in the C -Programming language for the IBM PC. The equations and underlying concepts behind the finite difference model will be discussed.

The purpose of the numerical analysis is to study mold surface temperature around the perimeter of the ring. Thus, a model geometry of the top of the ring was chosen. The symmetry of the ring shape was exploited in order to simplify the numerical analysis. Figure 6.1 shows three diagrams depicting the geometric simplifications made. Because of the symmetric shape of the ring it is assumed that there is an imaginary adiabatic wall dividing the core in half. It is therefore necessary to only consider one half of the mold. This half of the mold is highlighted by a dashed box in figure 6.1. A further simplification is that the two sides of the mold corresponding to the core and cavity inserts may simply be modeled as two blocks with plastic melt flowing between them. Finally only one side of the insert pair may be considered in the numerical analysis. All outer sides of the plastic melt and steel mold block are considered insulated for the purposes of this simulation.

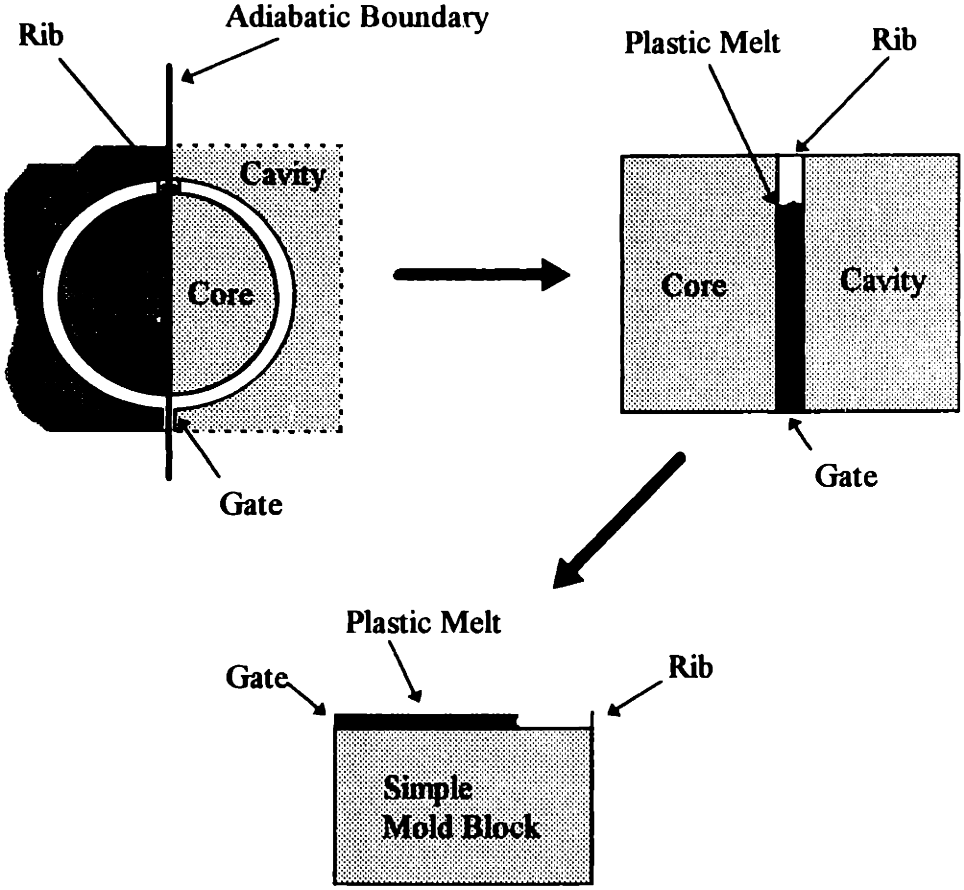

Figure 6.1: Simplification of mold geometry for numerical finite difference simulations.

To develop a numerical finite-difference formulation for unsteady conduction heat transfer in the rectangular mold block shown in figure 6.2, we subdivide the system into Z_s subvolumes with dimensions $\Delta x \Delta y \delta$. The thickness of the block, δ (into the page) is factored out in this 2D simulation. The resulting network of subvolumes is traditionally diagrammed by the use of nodes, with the mass of each subvolume assumed to be concentrated at its node. Each subvolume is treated as a lumped subsystem, with the temperature of a node assumed to represent the mean temperature of its subvolume. The distances between adjacent nodes is Δx or Δy. The x and y location of each node is given by $(m-1)\,\Delta x$ and $(n-1)\Delta y$, respectively: the values of m and n take on integer values with m ranging between 1 and M, and n taking values between 1 and N. The temperature at time t and location x,y is designated by $T_{m,n}^{\tau}$; the time index τ takes on integer values 0,1,2,..., and time t is equal to $\tau\Delta t$. [Thomas, 1980]

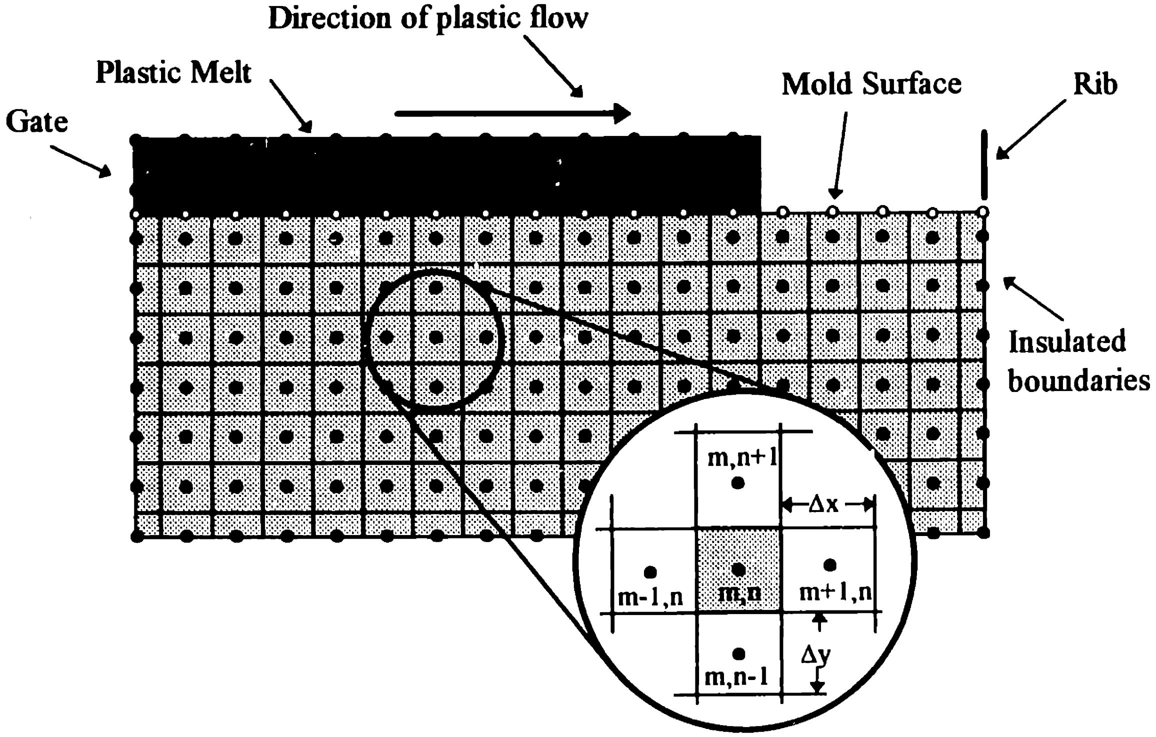

Figure 6.2: Representation of the mold block and plastic melt by network of subvolumes and nodes. Plate thickness is δ.

Once the finite difference grid is established, the numerical finite-difference formulation is developed by merely performing energy balances on each interior and exterior node. This approach will be seen to produce a system of Z_s algebraic equations which represent the energy transfer within the system.

Consider an energy balance on an interior subvolume such as the one shown in Figure 6.3(B). We obtain

$$\Delta q_x + \Delta q_y = \Delta q_{x+\Delta x} + \Delta q_{y+\Delta y} + \frac{\Delta E_s}{\Delta t} \qquad (3.1)$$

Where $\frac{\Delta E_s}{\Delta t}$ is not equal to zero and the heat-transfer rates are specified by the Fourier law of conduction at the instant t.

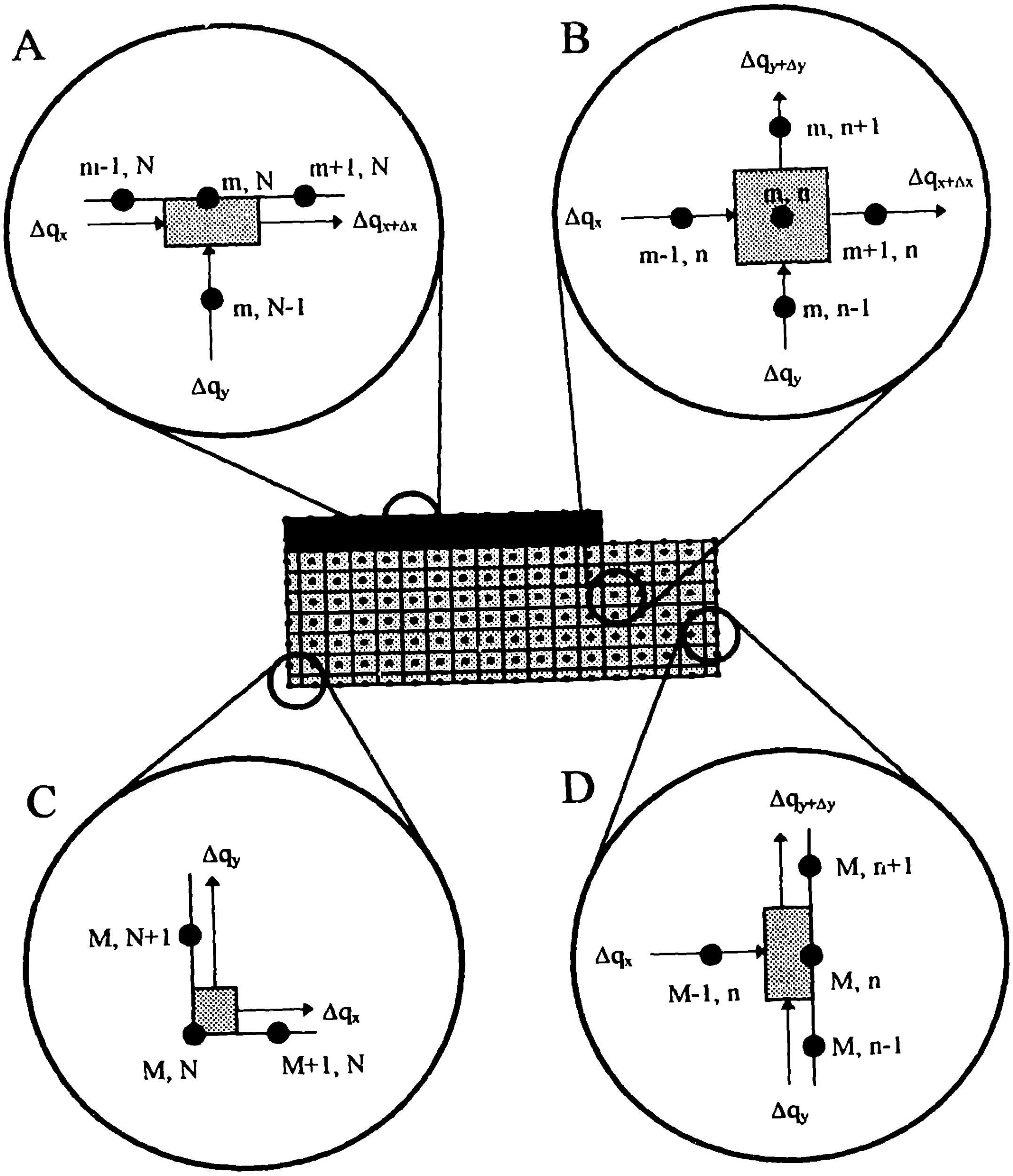

Figure 6.3: Diagrams of representative nodes(homogeneous material). (A) Regular exterior node (m,N). (B) Interior node (m,n). (C) Outer corner node (M, n). (D) Regular exterior node (M, n). [Thomas, 1980]

Based on our previous study, we know that $\frac{\Delta E_s}{\Delta t}$ can be expressed in terms of the specific heat and instantaneous temperature difference by (for uniform properties)

$$\frac{\Delta E_s}{\Delta t} = \frac{\Delta U}{\Delta t} = \rho \Delta V c_v \frac{\Delta T}{\Delta t} \tag{3.2}$$

This relationship for $\frac{\Delta E_s}{\Delta t}$ together with our finite-difference approximation of the Fourier law of conduction are substituted into equation 3.1, to obtain

$$\begin{aligned} &-k\delta\Delta y \frac{T^r_{m,n} - T^r_{m-1,n}}{\Delta x} - k\delta\Delta x \frac{T^r_{m,n} - T^r_{m,n-1}}{\Delta y} \\ &= -k\delta\Delta y \frac{T^r_{m+1,n} - T^r_{m,n}}{\Delta x} - k\delta\Delta x \frac{T^r_{m,n+1} - T^r_{m,n}}{\Delta y} + \rho \Delta V c_v \frac{\Delta T}{\Delta t} \end{aligned} \tag{3.3}$$

With Δy set equal to Δx. This equation can be written as

$$\frac{\Delta T}{\Delta t} = \frac{\alpha}{\Delta x^2}\left(T^r_{m+1,n} + T^r_{m-1,n} + T^r_{m,n+1} + T^r_{m,n-1} - 4T^r_{m,n}\right) \tag{3.4}$$

To complete our formulations, $\frac{\Delta T}{\Delta t}$ is usually expressed in terms of the forward time difference,

$$\frac{\Delta T}{\Delta t} = \frac{T^{r+1}_{m,n} - T^r_{m,n}}{\Delta t} \tag{3.5}$$

Utilizing the forward time difference, equation 3.4 takes the form

$$T^{r+1}_{m,n} - T^r_{m,n} = \frac{\alpha \Delta t}{\Delta x^2}\left(T^r_{m+1,n} + T^r_{m-1,n} + T^r_{m,n+1} + T^r_{m,n-1} - 4T^r_{m,n}\right) \tag{3.6}$$

This forward-time-difference equation expresses the nodal temperature at one instant $T^{r+1}_{m,n}$ in terms of the nodal temperature distribution $T^{r+1}_{m,n}, T^r_{m+1,n}, T^r_{m-1,n}, T^r_{m,n+1}, T^r_{m,n-1}$ at the earlier time τΔt. Because the nodal temperature distribution is known at some initial instant of time, this type of equation is *explicit* in that the unknown temperature at the next instant of time can be calculated directly.

Equation 3.7 below explicitly expresses the temperature at time $(\tau+1)\Delta t$ in terms of the temperature at the earlier instant of time $\tau\Delta t$:

$$\text{(B)}\quad T_{m,n}^{\tau+1} = \frac{\alpha\Delta t}{\Delta x^2}\left(T_{m+1,n}^{\tau} + T_{m-1,n}^{\tau} + T_{m,n+1}^{\tau} + T_{m,n-1}^{\tau}\right) + \left(1 - \frac{4\alpha\Delta t}{\Delta x^2}\right)T_{m,n}^{\tau} \qquad (3.7)$$

This equation solves the energy balance shown in figure 6.3(B) and may be used for the interior nodes of the modeled steel block and the plastic melt. Similar explicit equations can be written for the energy transfer at the exterior nodes figure 6.3 (A), (C), (D). These explicit equations are as follows:

$$\text{(A)}\quad T_{m,N}^{\tau+1} = \frac{\alpha\Delta t}{\Delta x^2}\left(T_{m+1,N}^{\tau} + T_{m-1,N}^{\tau} + 2T_{m,N-1}^{\tau}\right) + \left(1 - \frac{4\alpha\Delta t}{\Delta x^2}\right)T_{m,N}^{\tau} \qquad (3.8)$$

$$\text{(C)}\quad T_{M,N}^{\tau+1} = \frac{2\alpha\Delta t}{\Delta x^2}\left(T_{M+1,N}^{\tau} + T_{M,N+1}^{\tau} - 2T_{M,N}^{\tau}\right) + T_{M,N}^{\tau} \qquad (3.9)$$

$$\text{(D)}\quad T_{M,n}^{\tau+1} = \frac{\alpha\Delta t}{\Delta x^2}\left(2T_{M-1,n}^{\tau} + T_{M,n+1}^{\tau} + T_{M,n-1}^{\tau}\right) + \left(1 - \frac{4\alpha\Delta t}{\Delta x^2}\right)T_{M,n}^{\tau} \qquad (3.10)$$

During the filling stage of the molding cycle the plastic melt is in contact with the stainless steel mold surface near the gate and moves toward the rib. This is modeled in the finite difference simulation by a moving wall of nodes simulating the plastic melt. Figure 6.4 depicts the moving wall. The white circles between the plastic melt nodes and the mold block nodes designate points along the molding surface at which we wish to determine the instantaneous temperature. An addition to finite difference equation 3.7 will allow us to find the temperature at these surface points.

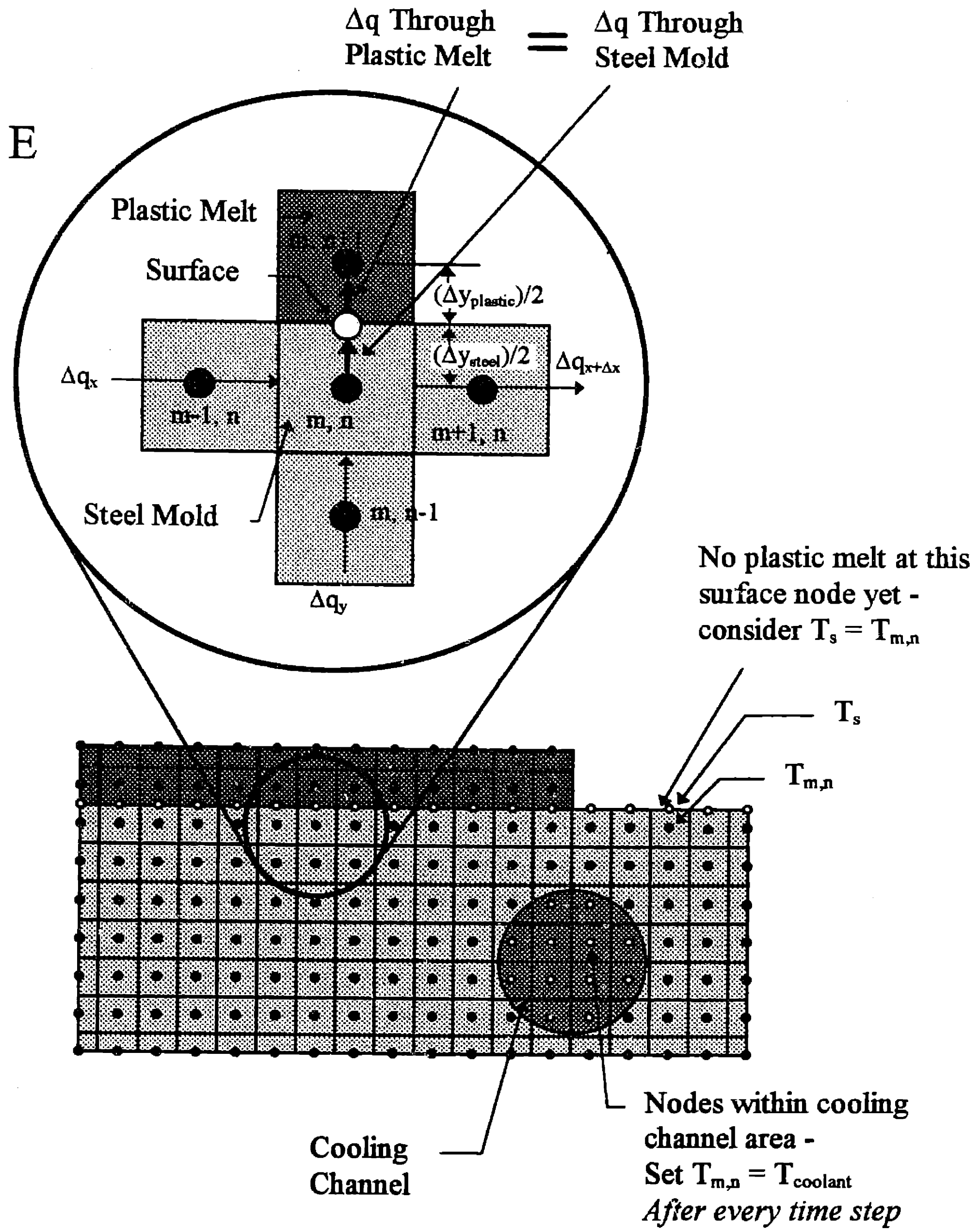

Figure 6.4: Subvolume at molding surface, (E) Molding surface interior node (m,n).

Consider the diagram for the molding surface subvolume described in figure 6.4 (E). At the interface between the steel and the plastic melt the surface temperature may be estimated. We first use the Fourier law to equate the heat flux through the steel to the heat flux through the plastic melt at the interface in order to obtain a surface temperature T_s. Equation 3.11 describes this relation:

$$-k_{plastic}A_y \frac{T^{\tau}_{m,n+1\,(plastic)} - T^{\tau}_s}{\left(\frac{\Delta y_{plastic}}{2}\right)} = -k_{steel}A_y \frac{T^{\tau}_s - T^{\tau}_{m,n\,(steel)}}{\left(\frac{\Delta y_{steel}}{2}\right)} \qquad (3.11)$$

This relation may be simplified to obtain the surface temperature T_s at time index τ.

$$T^{\tau}_s = \frac{\Delta y_{steel}k_{plastic}T^{\tau}_{m,n+1\,(plastic)} + \Delta y_{plastic}k_{steel}T^{\tau}_{m,n\,(steel)}}{\Delta y_{steel}k_{plastic} + \Delta y_{plastic}k_{steel}} \qquad (3.12)$$

If we expand equation 3.7, considering $\Delta x \neq \Delta y$, the following relation is obtained:

$$T^{\tau+1}_{m,n} = \Delta t\left(\left(\frac{\alpha_{steel}\left(T^{\tau}_{m+1,n} - T^{\tau}_{m,n}\right)}{\Delta x^2}\right) + \left(\frac{\alpha_{steel}\left(T^{\tau}_{m-1,n} - T^{\tau}_{m,n}\right)}{\Delta x^2}\right) + \left(\frac{\alpha_{steel}\left(T^{\tau}_{m,n+1} - T^{\tau}_{m,n}\right)}{\Delta y^2}\right) + \left(\frac{\alpha_{steel}\left(T^{\tau}_{m,n-1} - T^{\tau}_{m,n}\right)}{\Delta y^2}\right)\right) + T^{\tau}_{m,n} \qquad (3.13)$$

We consider the subvolumes to have different thermal properties - different plastic melt and stainless steel thermal diffusivities. In order to obtain the temperature at a node in the steel below the plastic melt we simply break the heat flux calculation across the interface into two separate relations across the distances ($\Delta y_{plastic}/2$) and ($\Delta y_{steel}/2$). The plastic melt and steel subvolume widths, $\Delta x_{plastic}$ and Δx_{steel}, are chosen to be equal in the simulations to simplify the nodal calculations. The subvolume width is simply designated as Δx. A final finite difference equation for the nodes of the steel in contact with the plastic melt (Figure 6.4 (E)) is:

$$\text{(E)} \qquad T_{m,n}^{\tau+1} = \Delta t\left(\left(\frac{\alpha_{steel}\left(T_{m+1,n}^{\tau} - T_{m,n}^{\tau}\right)}{\Delta x^2}\right) + \left(\frac{\alpha_{steel}\left(T_{m-1,n}^{\tau} - T_{m,n}^{\tau}\right)}{\Delta x^2}\right)\right. \qquad (3.14)$$

$$\left. + \left(\frac{\alpha_{plastic}\left(T_{m,n+1}^{\tau} - T_{s}^{\tau}\right)}{\left(\frac{\Delta y_{plastic}}{2}\right)^2}\right) + \left(\frac{\alpha_{steel}\left(T_{s}^{\tau} - T_{m,n}^{\tau}\right)}{\left(\frac{\Delta y_{steel}}{2}\right)^2}\right) + \left(\frac{\alpha_{steel}\left(T_{m,n-1}^{\tau} - T_{m,n}^{\tau}\right)}{\Delta y_{steel}^{2}}\right)\right) + T_{m,n}^{\tau}$$

Where T_s can be found from equation 3.12. The same approach is made for determining a finite difference equation for the nodes in the plastic melt in contact with the steel surface.

The surface temperature can only be calculated when a plastic melt node is in contact with a steel surface node. At the stages during the modeled injection molding cycle when there is no plastic in contact with the steel surface, the surface temperature T_s is assumed to be equal to that of the steel mold subvolume closest to the surface. Appendix F lists all of the nodal equations for the finite difference simulation.

Cooling channels are simulated in the mold block by first determining all of the nodes that lie in the cooling channel area. Figure 6.4 depicts a simple circular cross-sectional cooling channel (channel is orthogonal to the two dimensional mold block) and the nodes within this geometry. In order to simulate coolant flowing through the channel the temperature of all the nodes within the cooling channel geometry are set and re-set to the coolant temperature after *every* time step.

With the initial temperature distribution specified, the explicit interior and exterior nodal equations provide the means by which the temperature distribution can be obtained at the next increment of time, 1Δt. The temperature distribution at 1Δt can then be used as an input to calculate the distribution at 2Δt. This calculation procedure can be continued to obtain the temperature distribution over the number of time increments desired. Hence, future nodal temperatures can be calculated directly by the use of this explicit numerical finite-difference approach. [Thomas, 1980]

In regard to the mechanics of building a solution for $T_{m,n}^{r+1}$, the increments Δt and Δx (and Δy, which has been set equal to Δx) must be selected such that the coefficients associated with the $T_{m,n}^{r}$ term for each nodal equation must be equal to or greater than zero. If $\frac{\alpha\Delta t}{\Delta x^2}$ does not satisfy this criterion, our finite-difference "solution" will be unstable. The instability occurs because a mathematical condition is produced that violates the second law of thermodynamics. [Thomas, 1980] For unsteady three-dimensions (t,x,y) systems, this criterion takes the form:

$$\frac{\alpha\Delta t}{\Delta x^2} \leq \frac{1}{4} \tag{3.15}$$

Appropriate time steps and subvolume increments were chosen to ensure stability in all simulations.

6.1.2 Modeling an Injection Molding Cycle

The unsteady finite difference equations developed in the previous section can be used to develop a full simulation of an injection molding process. An important aspect of the model is that the boundary conditions on the surface of the steel mold block are changing. The simulation of the injection cycle is broken into three distinct stages; the filling stage, the cooling stage and the open stage. A given increment of time is set for each stage based on the actual time each stage takes in the experimental injection molding run being simulated.

During the "filling" stage plastic melt moves along the surface of the model steel block. The plastic melt cools as it moves along the mold surface. This is modeled in the simulation by "shifting" the plastic melt subvolumes along the model steel block. The entire heat transfer between the steel and the plastic melt is assumed to be through conduction. Every time a plastic melt subvolume enters at the gate (left side in figure 6.2) the simulation starts this new subvolume temperature at the plastic melt temperature of 220°C. This subvolume is shifted to the right in figure 6.2 after a given time increment equal to the filling time divided by the number of subvolumes along the length of the molding surface. As the subvolume is shifted it retains its previous temperature and continues to cool as it loses energy to the steel mold subvolumes. This filling stage simulation thus models the plastic melt cooling as it moves along the mold surface.

The "cooling" stage simply retains the mold and plastic melt temperatures at the end of the filling stage and continues the simulation. Because the plastic melt has "filled" the cavity the plastic melt subvolumes are no longer shifted. They continue to lose energy to the steel mold surface subvolumes during this stage. This simulates the plastic cooling.

The final stage of the injection molding cycle is the "open" stage in which the mold is open as a part is ejected from the mold surface. This stage is modeled by removing the plastic melt subvolumes from the surface of the mold block. Again, the starting temperatures of the steel mold subvolumes are set to the final temperatures of the cooling stage.

This procedure describes a single injection molding cycle. Multiple cycles are modeled by using the mold block nodal temperatures at the end of one cycle as the initial nodal temperatures for the next cycle. Figure 6.5 and 6.6 show flowcharts describing the finite difference algorithm for the injection molding simulation.

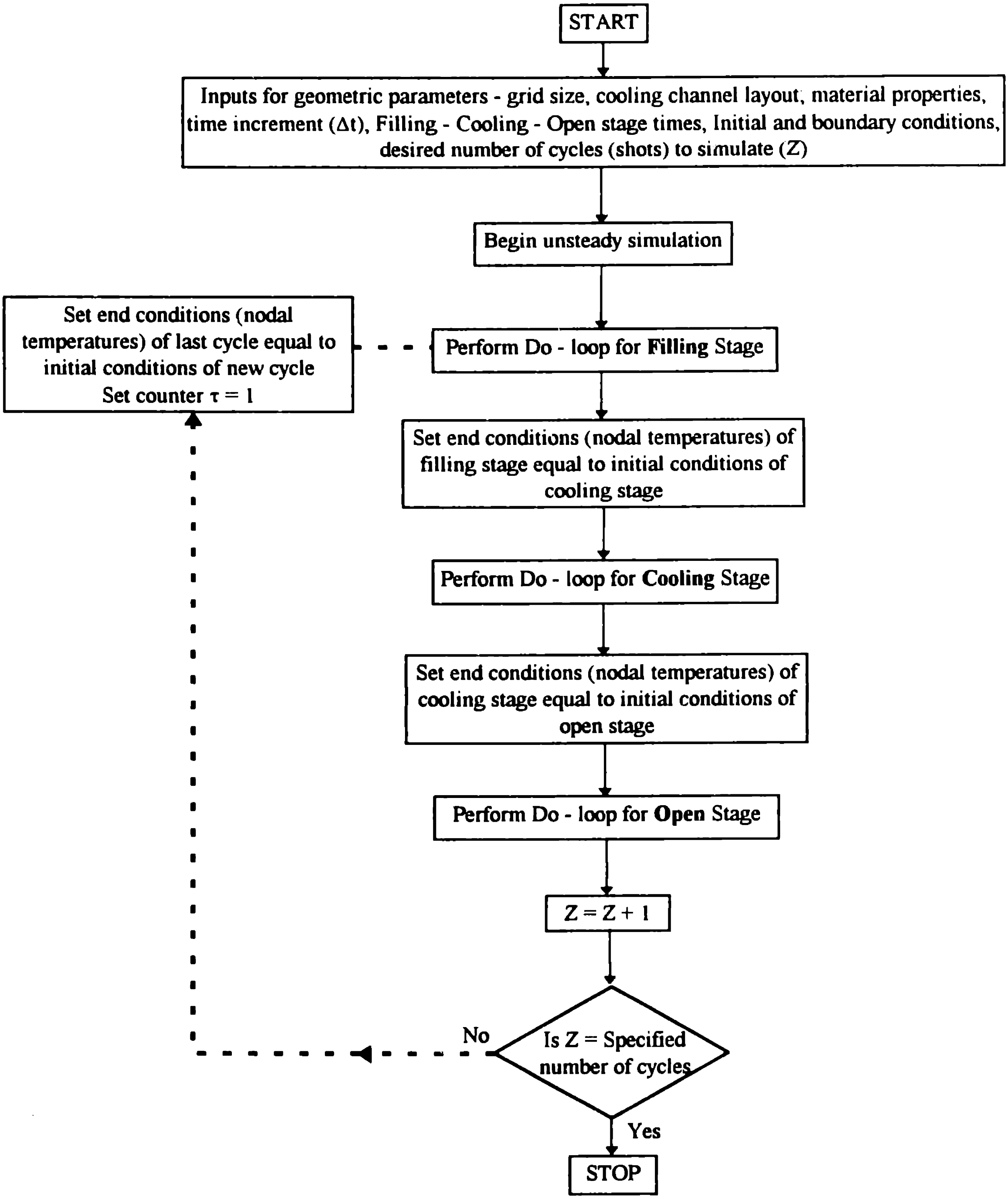

Figure 6.5: Flowchart of finite difference algorithm.

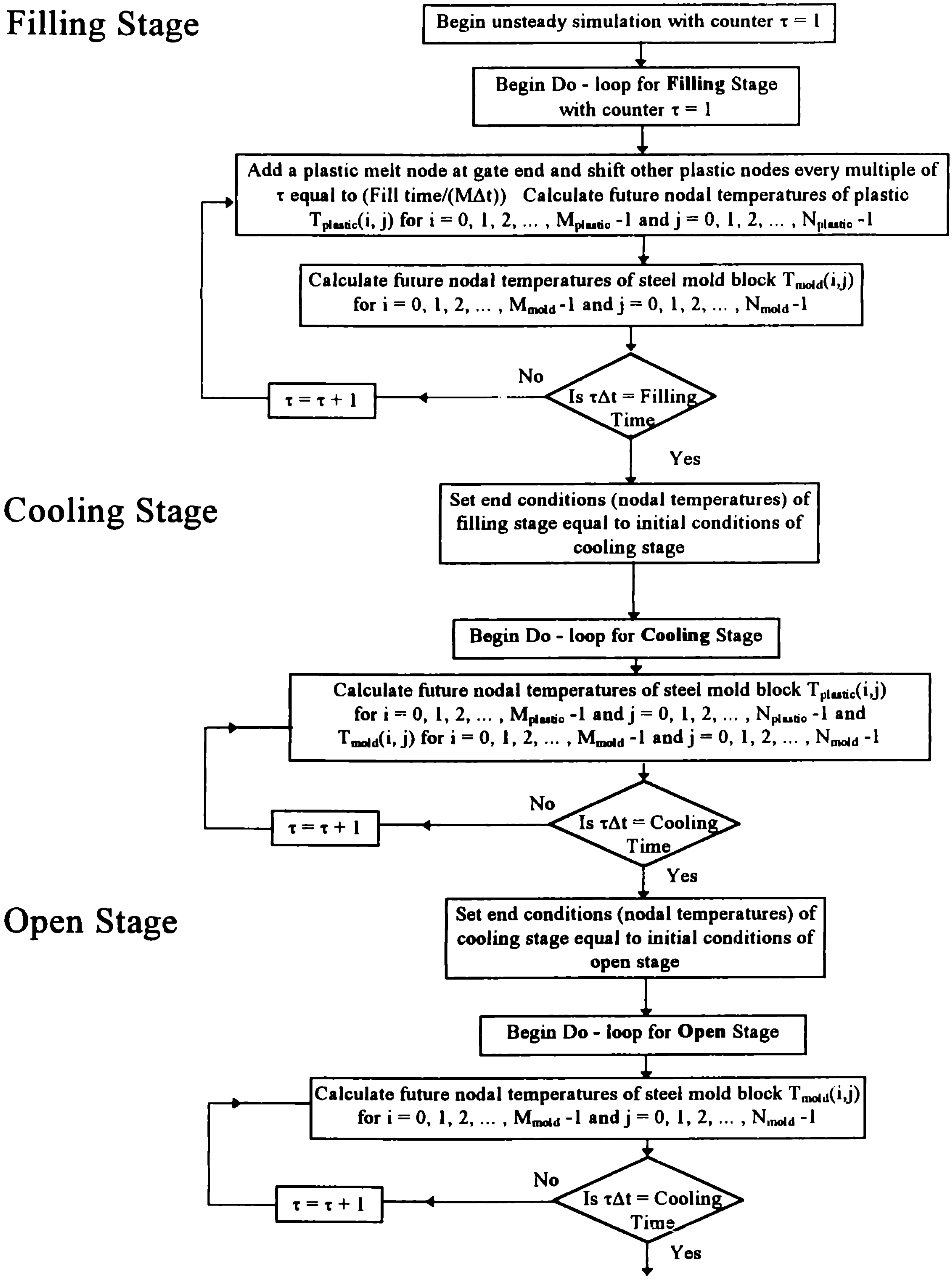

Figure 6.6: Flowchart detailing the filling, cooling and open stages.

6.1.3 Computer Implementation

The 2D finite difference model of the heat transfer within a mold during an injection molding cycle was created to discern the effect of changes in cooling passage placement and shape on the mold surface temperature. This model presents a graphical representation of the temperature gradients within the mold as well as a simulation of the surface temperature variation with time. The program was written in the C-programming language using a Borland C++ 3.1 Dos-Windows compiler on an IBM PC.

The mold block was divided into a finite difference grid size of 64 x 32 nodes. The plastic melt was divided into a finite difference grid size of 64 x 2 nodes (1.5 subvolumes - See Figure 6.2). An identical subvolume width (Δx = 0.86 mm) was used for the mold block and the plastic melt for simplicity of simulation. Different subvolume heights (Δy_{steel} = 0.86 mm, $\Delta y_{plastic}$ = 0.53 mm) were used for the plastic melt and the steel block. The plastic subvolume height was chosen to allow for a simulation plastic melt thickness equal to the half thickness of the experimental plastic ring. This thickness is 0.79 mm (1.5 subvolumes x 0.53 mm / subvolume). Cooling channel shape and size was set using a simple set-up bit-map that was edited using the Windows Paint-brush program. The Paint-brush program employs useful drawing features for creating different 2D channel shapes and sizes. Figure 6.7 depicts a representative set-up bitmap.

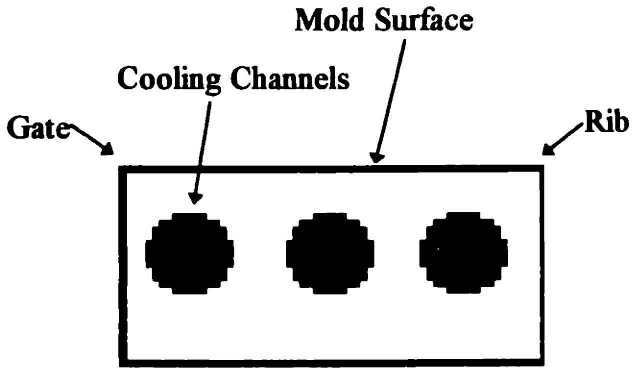

Figure 6.7: A representative set-up bitmap.

This set-up bitmap contains exactly 2048 (64 x 32) pixels. The area within the mold block that is designated as a cooling channel is set by using a specific color. A color bitmap to hexadecimal number converter was used to transform the graphical (bitmap) representation of the mold to a text (hexadecimal) representation. This hexadecimal representation could be conveniently used to set cooling channel areas and coolant temperatures in the model steel block of the finite difference simulation.

Figure 6.8 shows a snap-shot of the running simulation. This snap-shot shows the gradients in the steel mold after the completion of the filling stage. Circular cooling channels have been implemented in this simulation.

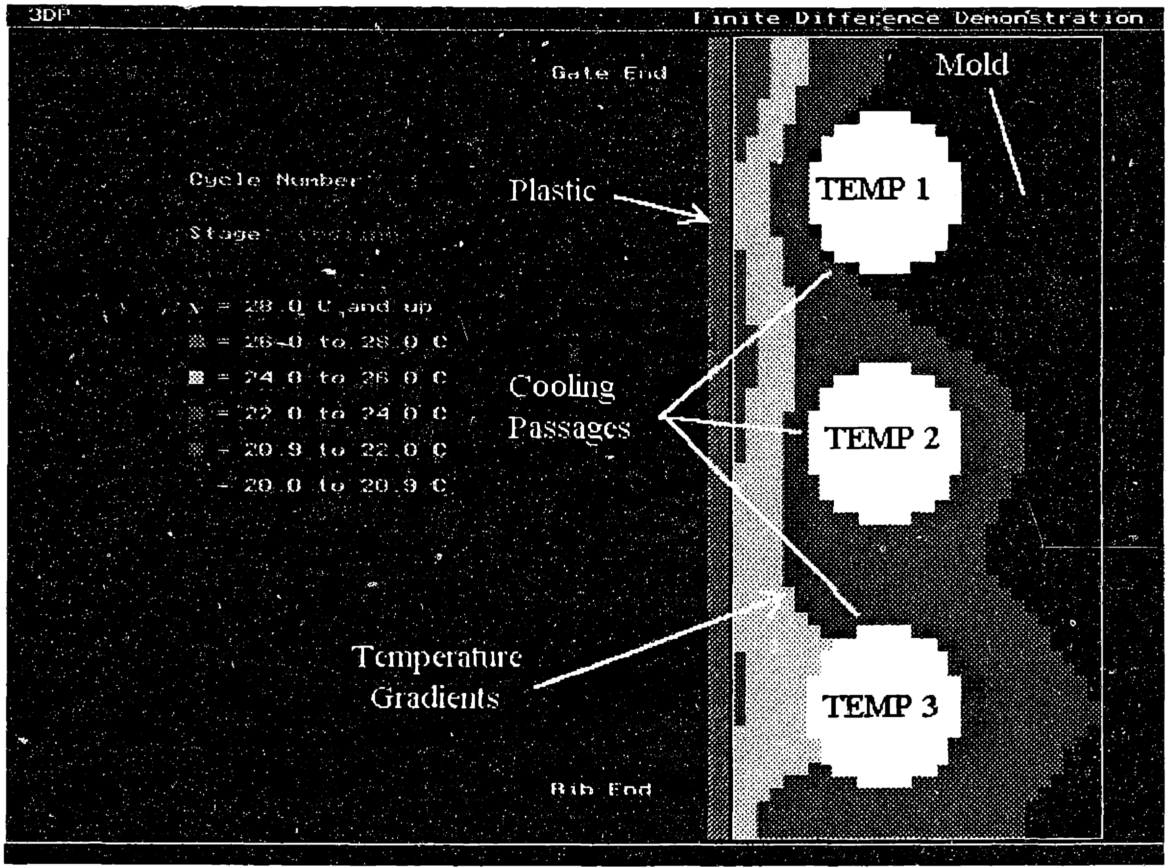

Figure 6.8: Snap-shot of the graphical finite difference simulation.

The following table is a list of material properties and parameters used in the finite difference simulations.

Simulation Parameter/Properties Description	Value
Total time of Filling stage	1.0 seconds
Total time of Cooling stage	6.0 seconds
Total time of Open stage	3.0 seconds
Density of 3D Printed material, ρ_{3DP}	8000 (kg/m^3)
Specific heat of 3D Printed material, $c_{p\,(3DP)}$	400 (J/kg-°C)
Thermal conductivity of 3D Printed material, K_{3DP}	26.3 (W/m-°C)
Thermal diffusivity of 3D Printed material, α_{3DP}	0.82 (10^{-5} m^2/s)
Density of polystyrene, $\rho_{polystyrene}$	1010 (kg/m^3)
Specific heat of polystyrene, $c_{p\,(polystyrene)}$	1747 (J/kg-°C)
Thermal conductivity of polystyrene, $K_{polystyrene}$	0.15 (W/m-°C)
Thermal diffusivity of polystyrene, $\alpha_{polystyrene}$	0.0085 (10^{-5} m^2/s)
Time increment Δt	0.005 seconds
Temperature of polystyrene melt at gate	220 °C
Subvolume increment in x direction in mold and plastic melt, Δx	0.86 mm
Subvolume increment in y direction in steel mold, Δy_{steel}	0.86 mm
Subvolume increment in y direction in plastic melt, $\Delta y_{plastic}$	0.53 mm

Table 6.1: Properties and parameters used in finite difference simulation.

6.2 Results of Finite Difference Simulations

Passages were designed such that differences between the molding surface temperature of the core and the cavity inserts are minimized in the injection molding cycle. Surface temperature differences are also be minimized along the perimeter of the cavity and core molding surfaces. The encouraging results of the simulations aided in the development of the conformal cooling passages produced in the 3D Printed inserts.

6.2.1 Simulation of Conformal Cooling Channel Design

The finite difference simulation was used to determine the mold surface temperature in the injection molding cycle for the conformal channels. The conformal channels remain a fixed distance (1/8 inch ~ 4 mm) from the molding surface in both the cavity and core inserts. Figure 6.9 is a diagram of the cooling channel layout in the finite difference simulations. This diagram depicts a channel that is 4 mm from the mold surface along the entire length of the mold block. This simple design thus simulates the conformal channel design. Simulations were run using this layout to predict the surface temperature variation in the 3D Printed inserts.

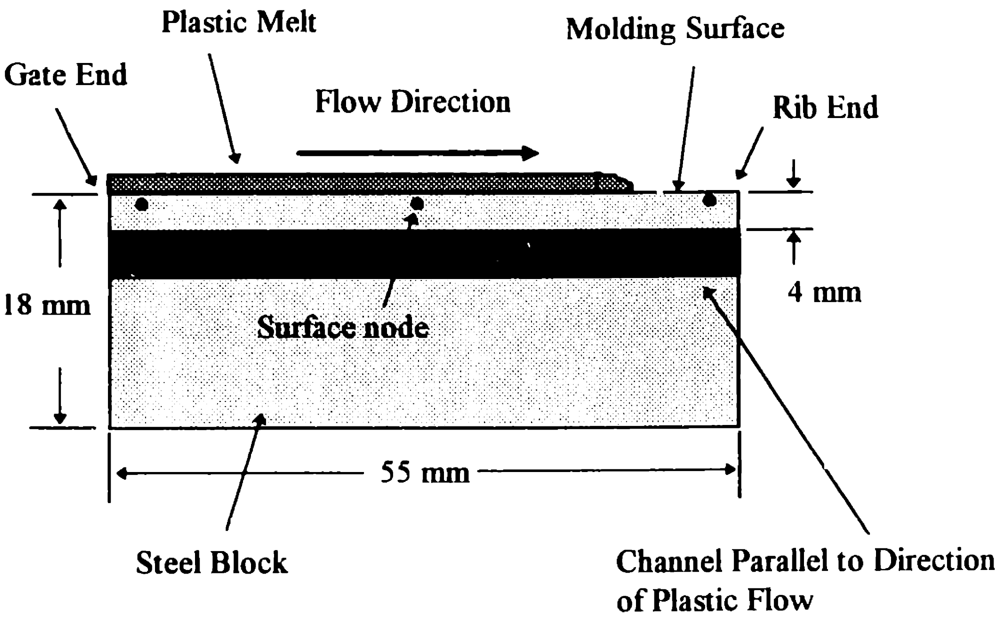

Figure 6.9: Cooling channel design diagram for 3D Printed inserts with conformal channels.

The dimensions of the mold block were chosen based on the dimensions of the core insert. The length of the mold block (55 mm) corresponds to the length of the mold surface of the core over which the plastic melt travels in the actual insert design. This is equal to approximately one half the diameter of the core. The width of the finite difference mold block is equal to the radius of the core (18 mm). The thickness of the plastic melt in the simulation was assumed to be 1/32 inch (0.79 mm) which is equal to one half of the thickness of the plastic ring.

Three points (surface nodes in figure 6.9) along the mold surface were chosen to obtain the surface temperature during an injection molding run. One node near the gate, one near the rib and one in the middle of the mold block were chosen. These points correspond to the placement of the surface thermocouple holes drilled in the cavity and core inserts. This match allows for a direct comparison with the experimental results.

Figure 6.10 shows the results of the finite difference simulation of the heat transfer in the inserts with conformal channels during and injection molding run.

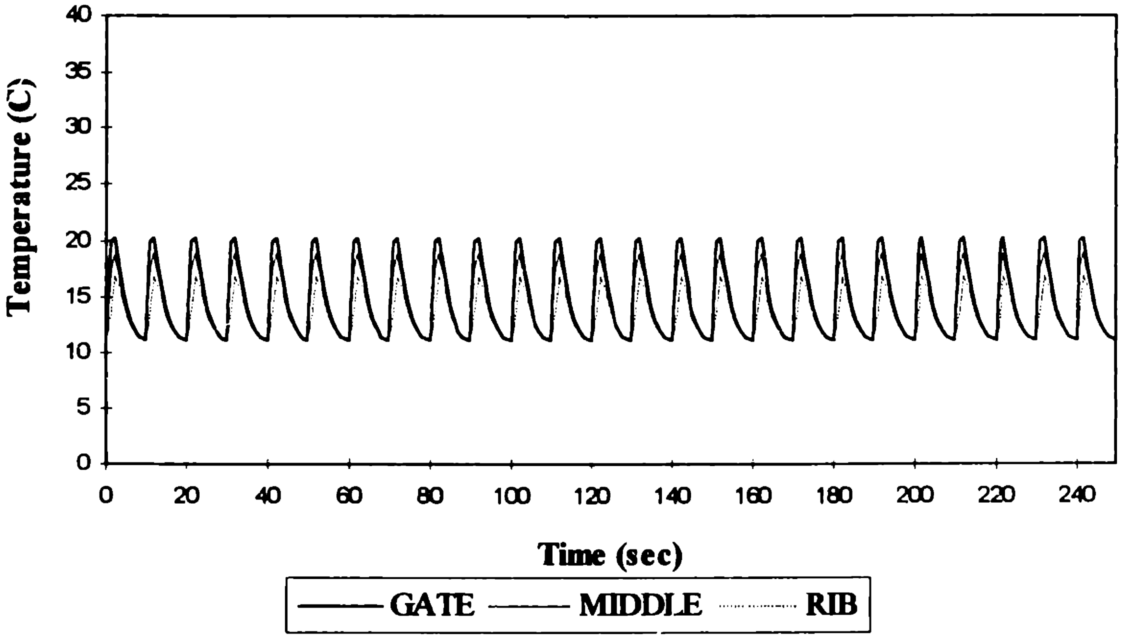

Figure 6.10: Finite difference simulation - conformal channels (3D Printed Inserts) - Coolant Temperature = 11 °C

The results of this finite difference analysis may be compared to the experimental results of the surface temperature versus time data for the 3D Printed core insert in figure 5.8. Figure 6.11 depicts one cycle of the simulation and one cycle of the experimental results. The simulation plot has been shifted on the time scale to synchronize the cycle starting time with that of the experimental data.

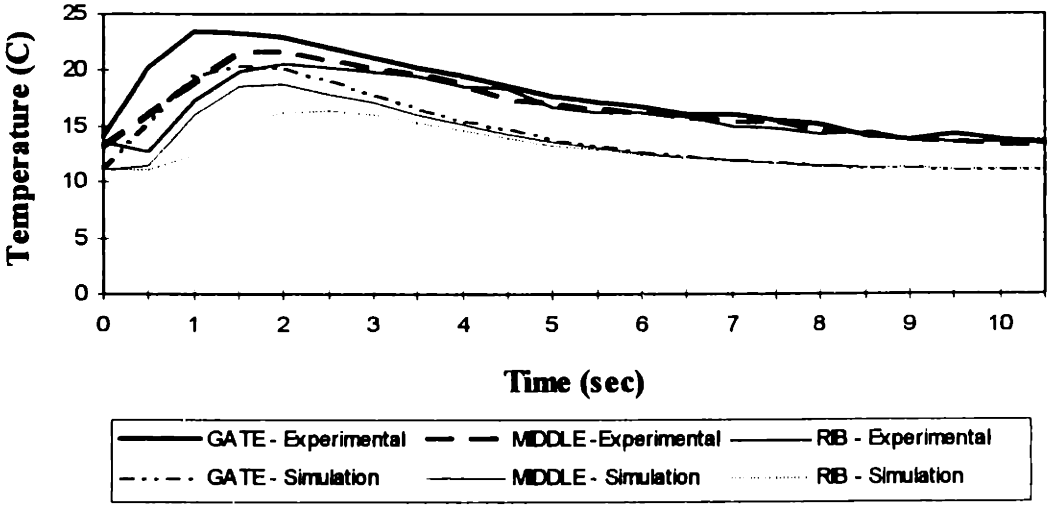

Figure 6.11: Simulation and experimental results for core insert with conformal channels. (Simulation coolant temperature = 11 °C / Experimental coolant temperature ≈13 °C)

The experimental and finite difference surface temperature plots have very similar shape. A temperature rise of the molding surface of approximately 10°C is observed in both the experimental and simulation plots. A difference in surface temperature at the beginning of the cooling cycle between the mold surface at the gate and the mold surface at the rib of approximately 4 - 5 °C is detected in both plots.

6.2.2 Effect of Wall Thickness Between Cooling Channel and Mold Surface

Several finite difference simulations were run for varying channel to mold surface distances. It was observed that the temperature rise during an injection molding cycle is approximately 10°C for distances greater than 4 mm. This fact is due to the relatively low thermal diffusivity of the 3D Printed material. (α_{3DP} = 0.82 x 10^{-5} m^2/s) In order to significantly reduce the rise in temperature the channel must be placed very close to the mold surface.

A simulation was run in which the distance between the mold surface and the cooling channel was halved to 2 mm. All other parameters remained the same as the previous simulation. Figure 6.12 depicts the results of this simulation.

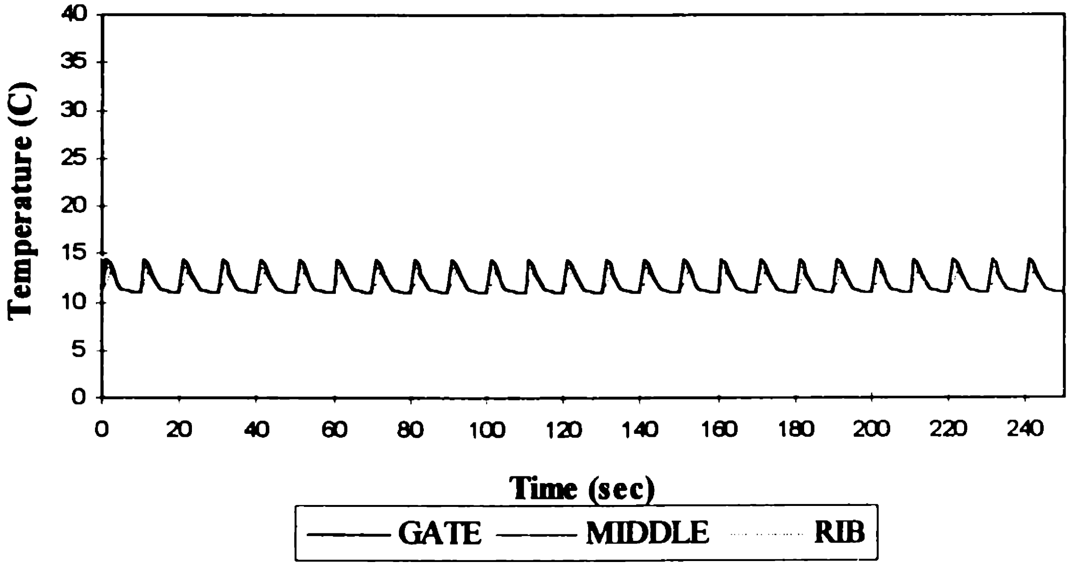

Figure 6.12: Finite difference simulation - conformal channels (3D Printed Inserts) - Coolant Temperature = 11 °C - Distance from Molding Wall to Channel Wall = 2 mm.

The rise in mold surface temperature at the gate is reduced significantly to approximately 4.5°C. This reflects the decreased distance between the cooling channel and the molding surface.

6.2.3 Effect of Mold Thermal Properties on the Performance of Conformal Channels

It is claimed that the results of the surface temperature measurements during the molding cycle for the 3D Printed inserts with conformal channels exhibit a more uniform temperature with no upward drift as compared to the results for the 303 stainless steel inserts with straight channels. This assertion does not account for the difference between the thermal properties of 303 stainless steel and the 3D Printed material. Table 6.2 compares the thermal properties of 303 stainless steel, pure bronze infiltrant and the infiltrated 316L stainless steel 3D Printed material.

Material	Density, ρ (kg/m³)	Specific Heat, c_p (J/kg-°C)	Thermal Conductivity, k (W/m-°C)	Thermal Diffusivity, α (10^{-5} m²/s)
303 Stainless Steel	8000	400	13.8	0.4
3D Printed - 10% Tin Bronze Infiltrated Stainless Steel	8000	400	26.3 (See Appendix E)	0.82
10% Tin Bronze	8780	377	50.0	1.51

Table 6.2: Thermal properties of 303 stainless steel, pure bronze infiltrant and infiltrated 316L 3D Printed material. (10% Tin Bronze values - Lyman, 1961)

A simulation of the conformal channel design using mold material thermal properties of 303 stainless steel was executed in order to determine the effect of the lower thermal conductivity value of the 303 stainless steel material. Figure 6.13 describes the results of this simulation.

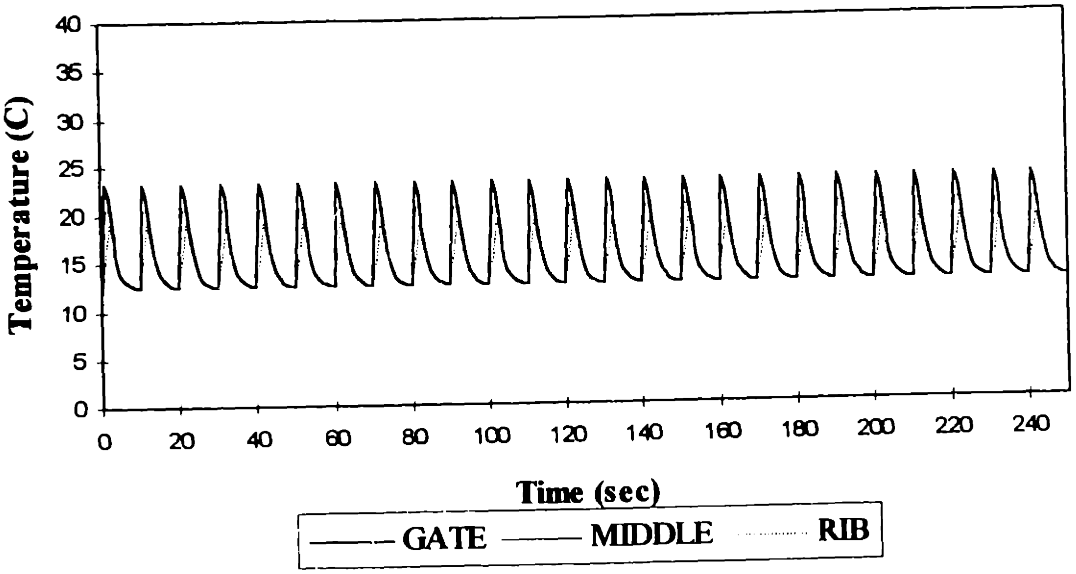

Figure 6.13: Finite difference simulation - conformal channels (Assuming thermal properties of 303 stainless steel) - Coolant Temperature = 11 °C - Distance from Molding Wall to Channel Wall = 4 mm

A comparison between the simulation of the conformal channel design using 3D Printed material thermal properties (Figure 6.10) and the simulation of the conformal channel design using the thermal properties of 303 stainless steel (Figure 6.13) may be made. The results of this simulation using the thermal properties of 303 stainless steel indicate an increased rise in mold surface temperature at the gate of approximately 2 °C as compared to the identical simulation using the thermal properties of 3D Printed material. No significant upward drift is noticed in the simulation using the thermal properties of 303 stainless steel.

These simulation results indicate that the lower thermal conductivity of the 303 stainless steel material compared to the 3D Printed material does not yield a significant impact on mold surface temperature results. Thus, it may be concluded that the conformal channel design, rather than the higher thermal diffusivity of the 3D Printed material, is the principal reason for the superior conformal channel mold surface temperature results.

The idea of creating bronze filled channels discussed in Chapter 3 spawns the question: Will the increased thermal conductivity and increased thermal diffusivity of the bronze infiltrant as compared to the bronze infiltrated 316L stainless steel material significantly effect the mold surface temperature? A simulation was run in which the thermal properties of the material were changed to that of the pure bronze infiltrant. The distance of the cooling channel to the mold surface is 4 mm. Note that this simulation assumes that the entire mold block has the thermal properties of pure 10% tin bronze. Figure 6.14 depicts the results of this simulation.

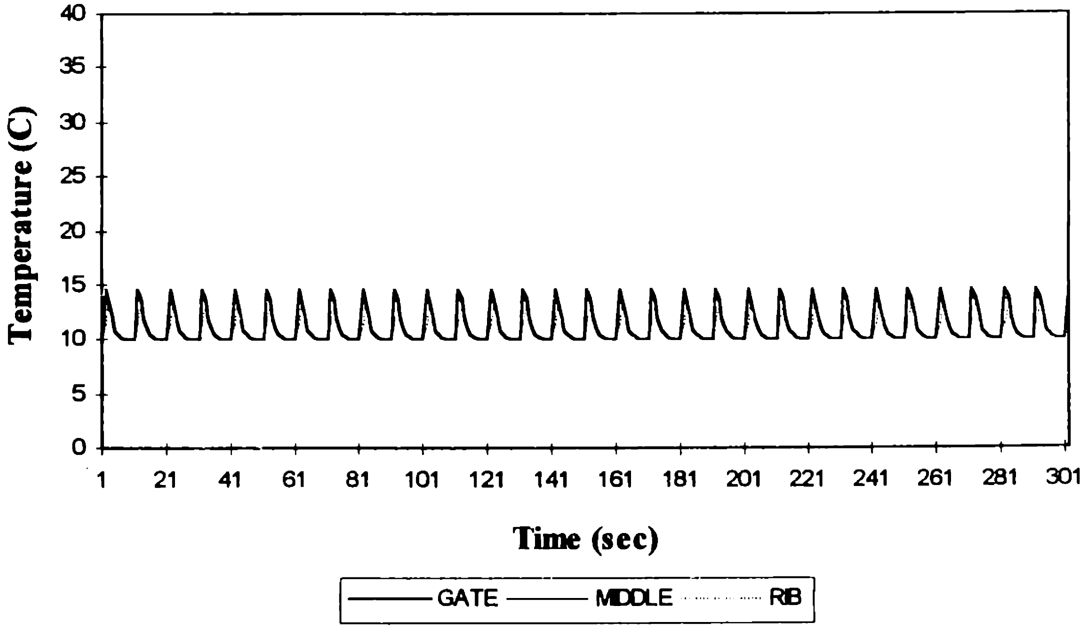

Figure 6.14: Finite difference simulation - conformal channels (Assuming thermal properties of pure bronze) - Coolant Temperature = 11 °C - Distance from Molding Wall to Channel Wall = 4 mm

The results show improvement in mold surface temperature uniformity and an overall decrease in mold surface temperature during the injection molding cycle. The results of this simulation indicate a reduced rise in mold surface temperature at the gate of 4.5°C as compared to the identical simulation with 3D Printed material. The difference in mold surface temperature between the gate end and the rib end at the beginning of the cooling cycle is also decreased by as much as 2°C. The ability to create channels filled with bronze utilizing the technology discussed in Chapter 3 improves heat transfer in the mold. The degree of improvement is probably not great enough to demonstrate significant improvement in part quality for the simple geometry studied in this research. However, one may envision complicated cavity geometries in which this improved heat transfer may have a significant impact.

7. Simulations of Various Cooling Channel Designs

As discussed previously, the cooling channel size, number, placement, cross-sectional shape and coolant temperature can easily be altered in the finite difference simulation. This is done by altering the colors and shapes of the cooling channels in the two-dimensional set-up bitmap. This chapter describes observations made in using the finite difference simulation of a mold with cooling channels.

Figure 7.1 describes the cooling channel diagram that is used in this chapter to depict various cooling channel designs. This diagram is a simple two-dimensional model of the injection molding process. Only one side of the mold (or insert) is used in analyzing the performance of each cooling channel design. The mold is modeled as a simple block of steel with plastic flowing from the gate end to the rib end on the molding surface. The two ends of the block are designated the gate end and the rib end to be consistent with the terminology used for the model of the 3D Printed molds.

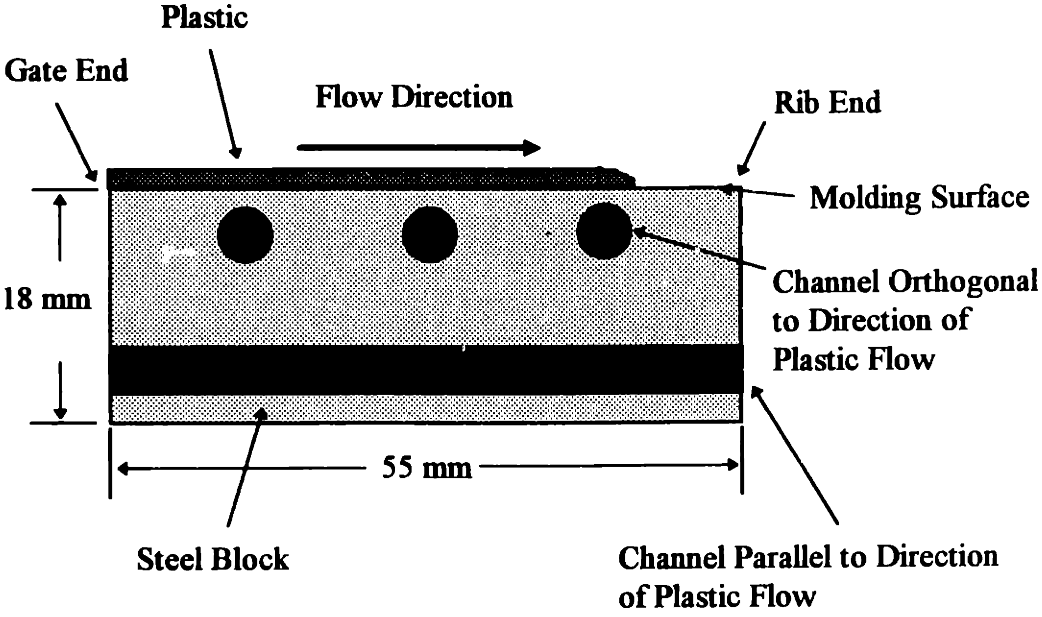

Figure 7.1: Cooling channel design diagram of finite difference simulations.

Simulations were run for various configurations of channel diameter, number of channels and distance from the surface. The molding surface temperature just after completion of the filling stage was captured for the entire length of the mold block. The beginning of the cooling stage was chosen due to the fact that it signifies the onset of solidification and the beginning of the buildup of residual stress in the molded part. The filling and cooling phase of the molding process are the crucial stages for maintaining uniform temperature control from cycle to cycle. A coolant temperature of 10 °C was set for each channel in the block. In all cases the finite difference algorithm simulated shots of plastic until the mold surface temperature cycle reached a plateau. Figure 7.2 shows several cooling channel configurations and the surface temperature output for each design.

7.1 Channels Parallel to Direction of Plastic Flow

This section describes the results of the finite difference simulations for designs in which the cooling channels are parallel to the direction of plastic flow. The conformal channels in the 3D Printed inserts described earlier were designed with channels parallel to the direction of plastic flow. The following results of simulations of channels parallel to the direction of plastic flow aided in the original design of the conformal channels in the 3D Printed inserts.

Each of these simulations contain channels that remain a fixed distance away from the molding surface along the entire length of the mold. Three different mold surface to cooling channel distances were simulated, 2mm, 4mm and 16mm. Figure 7.2 shows the mold surface temperature results for the three designs.

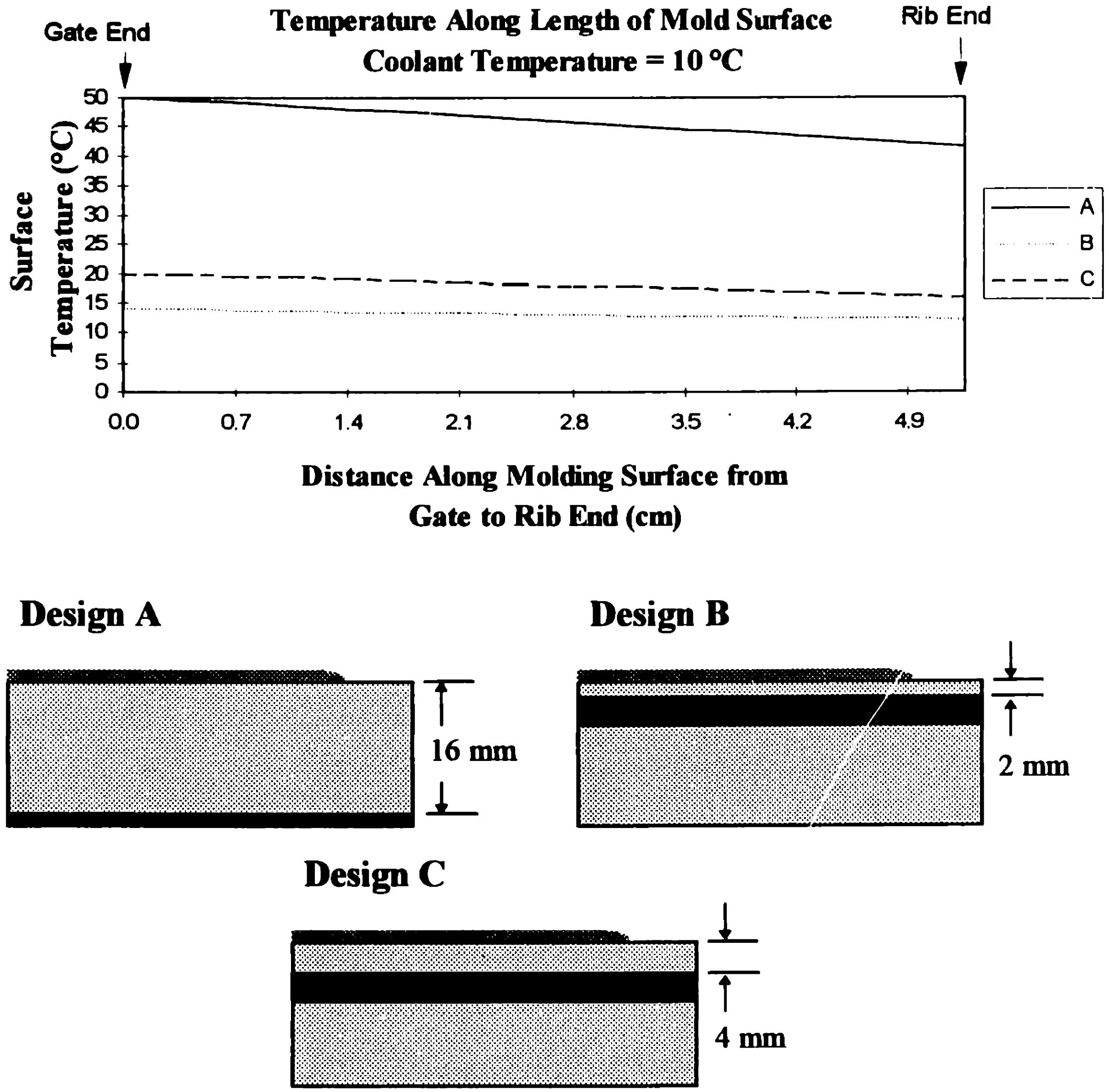

Figure 7.2: Mold surface temperature along length of mold for three channel designs.

Several observations may be made from the surface temperature results for the three channel designs, A, B and C. The first observation is that the surface temperature is higher at the gate end than at the rib end in all designs. This is due to the length of time that the plastic is in contact with the molding surface and the fact that the plastic cools as it moves along the molding surface. The molding surface near the rib end is in contact with the plastic melt for a shorter period of time and the plastic has cooled somewhat as it flowed from the gate end. The gate end surface temperature is consistently higher than the rib end surface temperature.

Another observation is that the overall surface temperature increases as the channel is moved farther form the molding surface. This is evidenced by the results for designs A and B.

Surface temperature uniformity along the length of the mold surface is the most important performance measure of a particular cooling channel design. The results for design A indicate a temperature variance (highest temperature on surface - lowest temperature on surface) of 10 °C. The variance for design C is 5 °C and the variance for design B is 2 °C. Thus, as the parallel channels move closer to the mold surface the variance decreases and we find improved mold surface temperature uniformity. These results may also be explained by the fact that the model of the mold is two-dimensional and the parallel channels essentially act as a cooling wall. Therefore, there is no heat transfer beneath the channels. In the extreme case in which the channel is placed just beneath (less than 0.1 mm) the mold surface, the mold surface temperature would become perfectly uniform at the temperature of the coolant. Of course this would not be a structurally sound design.

Design C describes the model of the 3D Printed inserts. At the gate end after the filling stage the temperature rises to a temperature of 20 °C. The ~10 °C rise in mold surface temperature is consistent with the experimental results shown previously in figure 5.7.

7.2 Channels Orthogonal to Direction of Plastic Flow

This section describes the results of the finite difference simulations for designs in which the cooling channels are orthogonal to the direction of plastic flow. Several characteristics of the cooling channels are varied in these simulations. The characteristics discussed are: channel distance from molding surface, distance between channels, number and cross-sectional size of channels and cross-sectional shape of channels.

7.2.1 Channel distance from molding surface

Both designs D and E are composed of three separate parallel channels orthogonal to the direction of plastic flow. Figure 7.3 depicts the two designs and their associated mold surface temperature profiles.

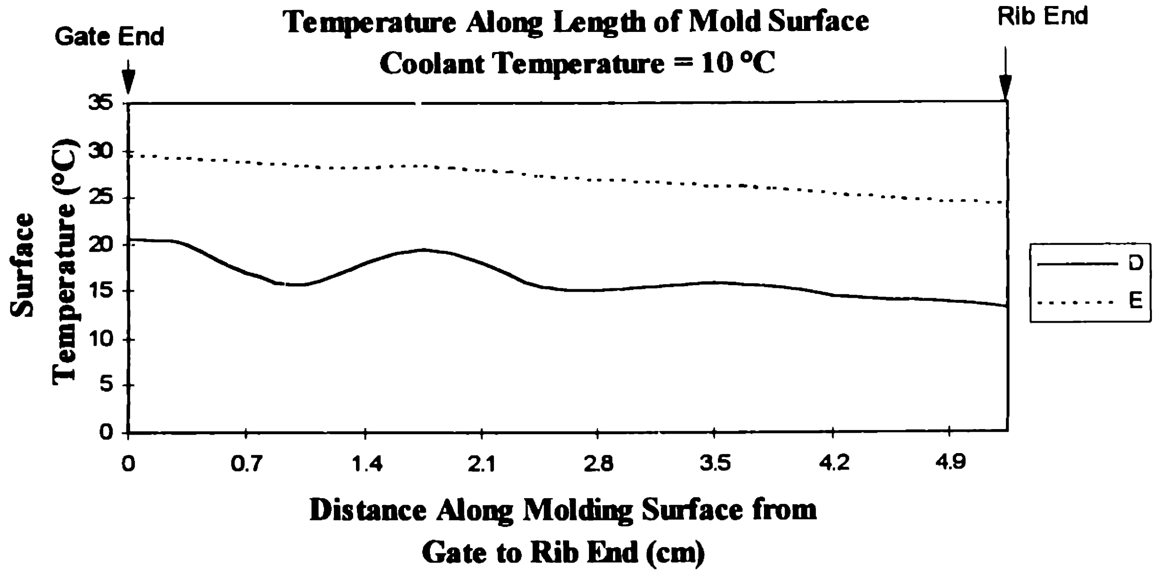

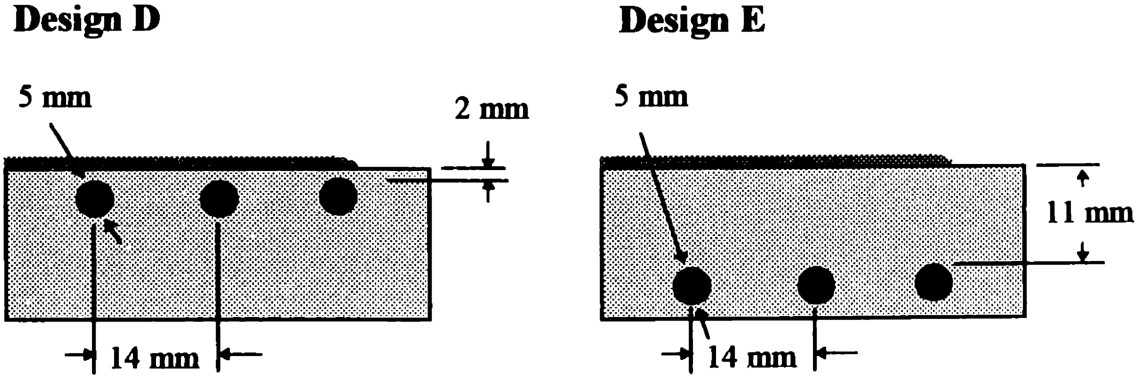

Figure 7.3: Comparison of mold surface temperature along length of mold for two channel designs having different distances from mold surface.

In each design the passages are circular in cross-section, 5 mm. in diameter and spaced 14 mm apart. In design D the channels are 2 mm. from the mold surface and in design E the channels are 11 mm. from the mold surface.

Studying the mold surface temperature of design D one easily notices the large undulations. Figure 7.4 describes the position on the molding surface where the "hills" and "valleys" in surface temperature occur.

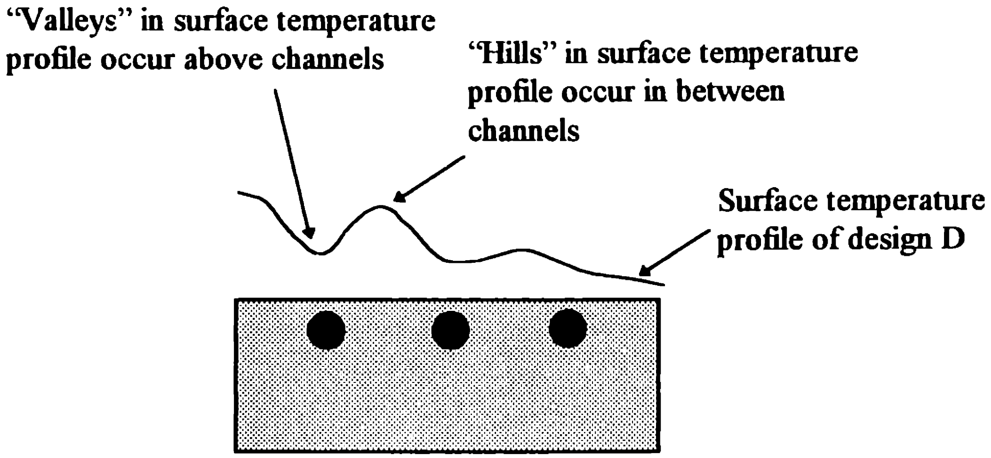

Figure 7.4: Explanation of "hills" and "valleys" found in surface temperature profile of design D.

One notices that the surface temperature is much lower just above the channels and higher in between them. The large difference between the surface temperature above the channels and in between the channels is due to the low thermal diffusivity of the 3D Printed material. Heat is trapped in the area between the channels and is dissipated quickly in the area just above the channels.

In design E the three channels are placed well below the mold surface. An overall rise in temperature may be noticed. The oscillation in surface temperature may be observed in the surface temperature profile in design E. However, the oscillation is much lower in magnitude. The mold surface temperature profile for design D depicts a surface temperature variance of 11 °C. Design E has a surface temperature variance of only 6 °C.

In comparing the two designs several conclusions can be made. The overall surface temperature may be decreased by moving the cooling channels closer to the surface. This is beneficial in that it decreases the necessary cooling time, increasing throughput. However, a price is paid in surface temperature uniformity. A mold surface with large surface temperature variations causes residual stresses in the molded parts.

By moving the channels farther from the surface of the mold as in design D, surface temperature uniformity is improved. The undulations in the surface temperature diminish significantly for channel to mold surface distances greater than 12 mm. However, the overall temperature of the surface increases. Thus, a trade-off between the two characteristics is necessary. A channel to mold surface distance of approximately 4 - 8 mm provides a reasonably good compromise.

The drift in the initial surface temperature in the molding cycle increases as the conformal channels are positioned farther from the mold surface. When the channels are close to the mold surface (approximately less than 10 mm) the drift is small. When this distance is large (greater than 10 mm) there is a significant upward drift in the initial surface temperature of the molding cycle during an injection molding run. An energy balance relation be employed to explain this occurrence.

We may consider a situation in which a simple one-dimensional steel mold block, initially at T_i, is suddenly heated at its boundary to a new temperature, T_∞. The temperature difference ΔT across the thickness of the block x, is equal to (T_∞ - T_i). An energy balance may be performed relating the energy conducted through the block to the change in internal energy. Equation 7.1 describes this relation:

$$kA\frac{\Delta T}{x}t = \rho c_p A x \Delta T \tag{7.1}$$

where k is the thermal conductivity of the mold material, A is the cross sectional area of the mold block (area through which heat is conducted), t is time, ρ is the density of the mold material and c_p is the specific heat of the mold material. This relation may be reduced to find the thickness in terms the thermal diffusivity of the mold material, α, and the time.

$$x = \sqrt{\alpha t} \tag{7.2}$$

This equation indicates that at a mold thickness in excess of $\sqrt{\alpha t}$, for a sudden boundary temperature rise, energy cannot be conducted fast enough to dissipate the energy buildup in the mold material.

We may consider the thickness, x to be the distance between a conformal cooling channel and the mold surface. The coolant in the channel provides the initial mold temperature and the plastic melt provides the sudden boundary temperature rise on the opposite side of the mold block. Equation 7.2 may be used to approximately determine a distance from the molding cavity within which conformal channels will have a significant impact on mold surface temperature.

We may use equation 7.2 to determine the distance from the mold surface at which the change in internal energy is equal to the energy conducted through the mold block. This distance evaluated over the filling time (1.0 sec), using the thermal diffusivity of 3D Printed material (0.82×10^{-5} m^2/s), is equal to 2.8 mm. This distance evaluated over the entire cycle time (~10 sec) is equal to 9.0 mm.

The calculated distance from the mold surface at which the energy conducted is equal to the change in internal energy (evaluated over just the filling time) is concurrent with the distance at which the mold surface temperature swing within the cycle (approximately 10 °C) remains unchanged. In other words, at a distance less than this value (2.8 mm) the temperature swing at the mold surface decreases significantly. At a distance greater than this value the temperature swing remains constant at ~ 10 °C. This observation was obtained from the finite difference simulations.

The calculated distance from the mold surface at which conduction is equal to the change in internal energy (evaluated over the entire cycle time) is concurrent with the distance at which upward mold surface temperature drift (from one cycle to the next) increases significantly. This distance (9.0 mm) is also approximately equal to the distance at which the mold surface temperature undulations significantly diminish (simulations for channels orthogonal to direction of plastic flow). These observations indicate that equation 7.2 is a useful approximation for the distance from the molding cavity within which conformal channels will have a significant impact on mold surface temperature.

7.2.2 Number of channels, distance between channels and channel diameter

Design F proposes a design in which the channel diameters and the distance between the channels are decreased. Design F contains five channels as opposed to design D that contains three. A comparison is made in this section of the two designs. Figure 7.5 depicts the two designs and their associated mold surface temperature profiles.

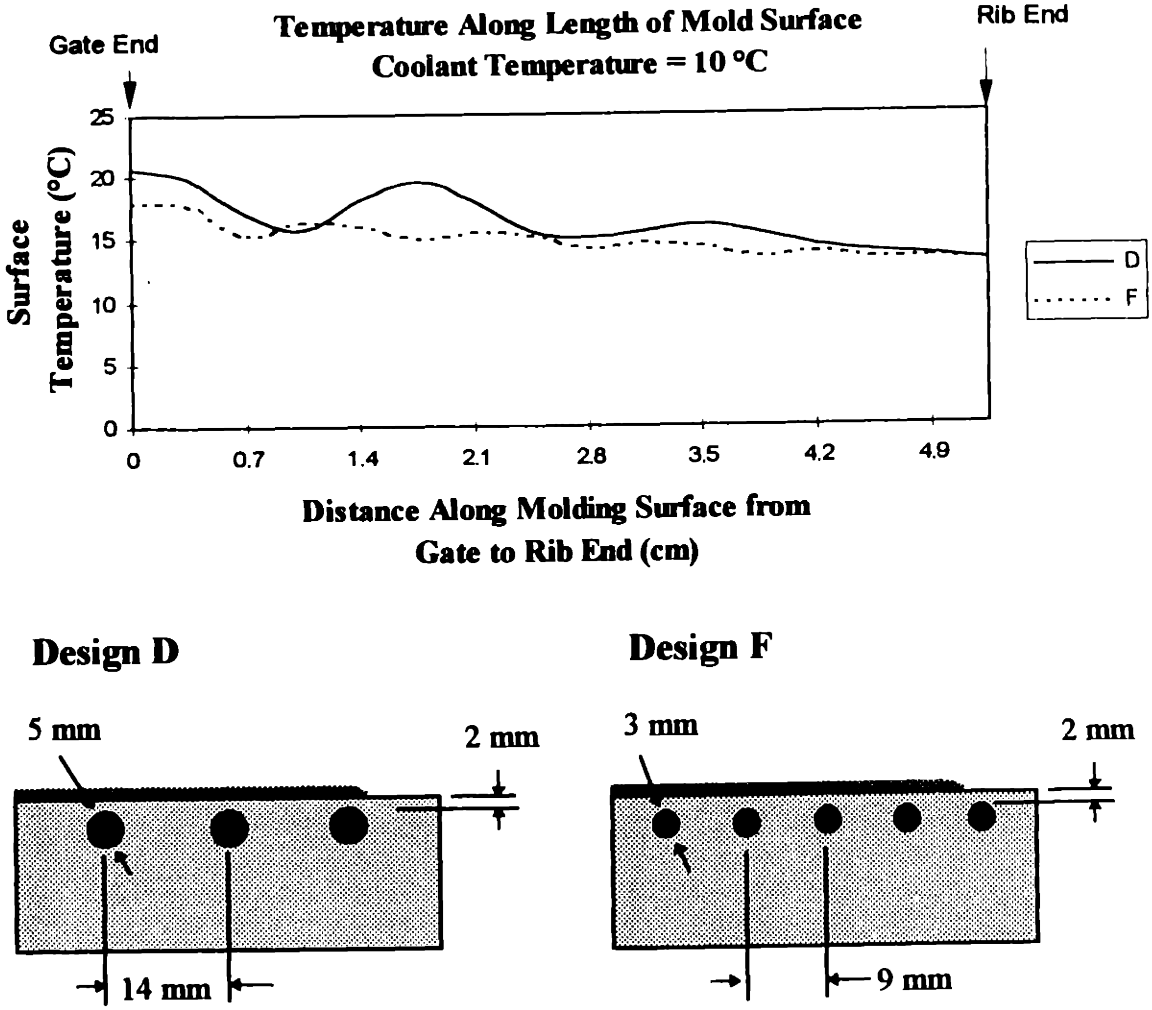

Figure 7.5: Comparison of two channel designs having different size and number of channels.

Both design D and design F contain cooling channels that are 2 mm away from the molding surface. The channel cross-sections in design D are 5 mm in diameter while those in design F are 3 mm. in diameter. The channels in design F are spaced closer together than design D (9 mm apart compared to 14 mm apart). The surface temperature profile for design F depicts "hills" and "valleys" as seen in design D. The surface temperature profile of design F indicates more undulations having smaller magnitudes. Again, the "hills" occur in between the channels and the "valleys" occur just above the cooling channels.

A definite advantage can be seen in design F. The surface temperature variance in design F is only 5.5 °C as compared to 11 °C for design D. The decreased surface temperature variance is due to the increased number of channels. The magnitude of the first "hill" in the surface temperature profile of design D is approximately 4.0 °C. The magnitude of the first undulation in the surface temperature profile of design F is 1.5 °C. Thus, uniformity of surface temperature may be improved without having to place the channels farther from the mold surface. This allows for a lower overall surface temperature.

7.2.3 Cross-sectional shape of channels

Design G proposes a design in which the cross-sectional shape of the channels are square. The surface temperature profile for this design is compared to the profile for design D containing channels that are circular in cross-section. Figure 7.6 describes the two designs and their associated mold surface temperature profiles.

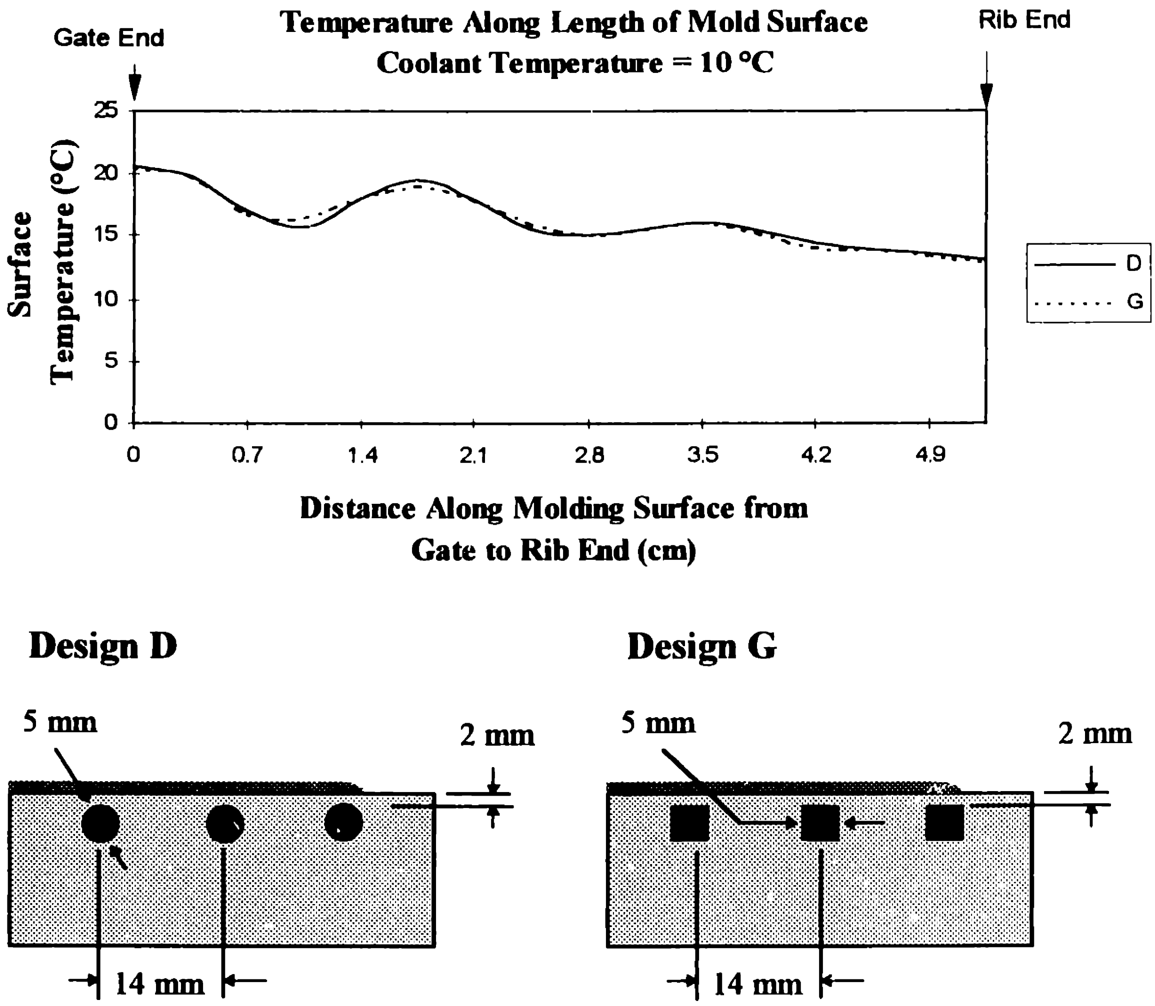

Figure 7.6: Comparison of two channel designs having different cross-sectional shapes.

In design G the length of one side of the square channel is equal to the diameter of the circular channels of design D. All other parameters in both simulations were set to the same values. Although design G does offer a surface temperature profile that undulates with a slightly lower magnitude as evidenced by the surface temperature profiles shown in figure 7.6, there is very little difference in performance between the two designs. Several other cross-sectional shapes with the same general cross-sectional area yielded similar results.

The simulation operates on the assumption of conduction at the cooling channel wall rather than convection. This may be an over - simplification. It is possible that cooling channel cross-section may significantly impact flow in the channel and thus, heat transfer in the mold.

8. Conclusions

A framework has been provided for the creation of injection molding tooling with conformal cooling channels. A preliminary investigation was established analyzing the effects of conformal cooling channels on mold surface uniformity and control. This chapter provides a brief review of the results obtained in this investigation and discusses areas where potential opportunities may lie.

8.1 Creating Injection Molding Tooling with Conformal Cooling Channels

Three Dimensional Printing is a desktop manufacturing process in which powdered materials are deposited in layers and selectively joined with binder from an ink-jet style printhead. Stainless steel (316L) powder is selectively bound with a latex emulsion binder using the 3DP process resulting in a green part. Unbound powder is removed upon process completion and a series of post-processing steps similar to those found in powder metallurgy processing is used to obtain all-metal injection molding tooling with conformal cooling passages. These post - processing steps consist of debinding, sintering and infiltration.

A new method of infiltration (stilt infiltration) was born out of the need for an infiltration process that may be used to reliably infiltrate tooling with small cooling channels. This stilt infiltration method consists of placing the porous sintered metal part on sintered metal blocks or cylindrical stilts in a crucible. Bronze shot is placed in the crucible and the arrangement heated in a furnace to the appropriate infiltration temperature. The stilt infiltration process relies on capillary forces to draw the molten bronze infiltrant up the stilts and into the sintered part.

A summary of observations obtained from the stilt infiltration results follows:

- Utilizing the stilt infiltration process, parts with small channels may be successfully infiltrated without danger of filling the channels with infiltrant.

The equation for the maximum capillary rise between two flat plates is as follows:

$$h = \frac{2\gamma \cos\theta}{\rho g w} \tag{8.1}$$

where,

w is width of the channel. (distance between the two walls), $\gamma\cos\theta$ = surface tension force per unit length of liquid bronze infiltrant, θ is the wetting angle between the surface and the plane of contact, (for perfectly wetting; $\theta = 0$ degrees), ρ is the density of the molten infiltrant, g is gravity and h is the height of infiltrant rise.

This equation is fairly accurate for predicting necessary stilt height for infiltration of parts with small channels.

- The stilt infiltration process offers a significantly reduced risk of under-infiltration due to the fact that the pool of molten bronze on the bottom of the crucible feeds the open porosity in the part.

- Reduced erosion of the part may be possible using the stilt infiltration method.

- High channel surface roughness significantly effects the prediction of the maximum capillary rise. The surface roughness effectively decreases the width of the channel. This decrease in width increases the predicted maximum capillary rise. Thus, for channels with a high surface roughness the channel width should be measured as the distance between the highest points on each wall surface.

8.2 Straight versus Conformal Channels

A direct comparison was obtained of the mold surface temperature during the injection cycle of a 3D Printed mold (core and cavity inserts) with conformal channels and an identical mold machined of 303 stainless steel with conventional straight channels. Figure 8.1 depicts the molding cavity surface temperature of the 303 stainless steel core insert with straight channels and the surface temperature of the 3D Printed core insert with conformal channels. The surface temperature was tracked throughout an injection molding run by using three thermocouples embedded near the molding surface. Figure 8.1 illustrates the core insert and channel geometries.

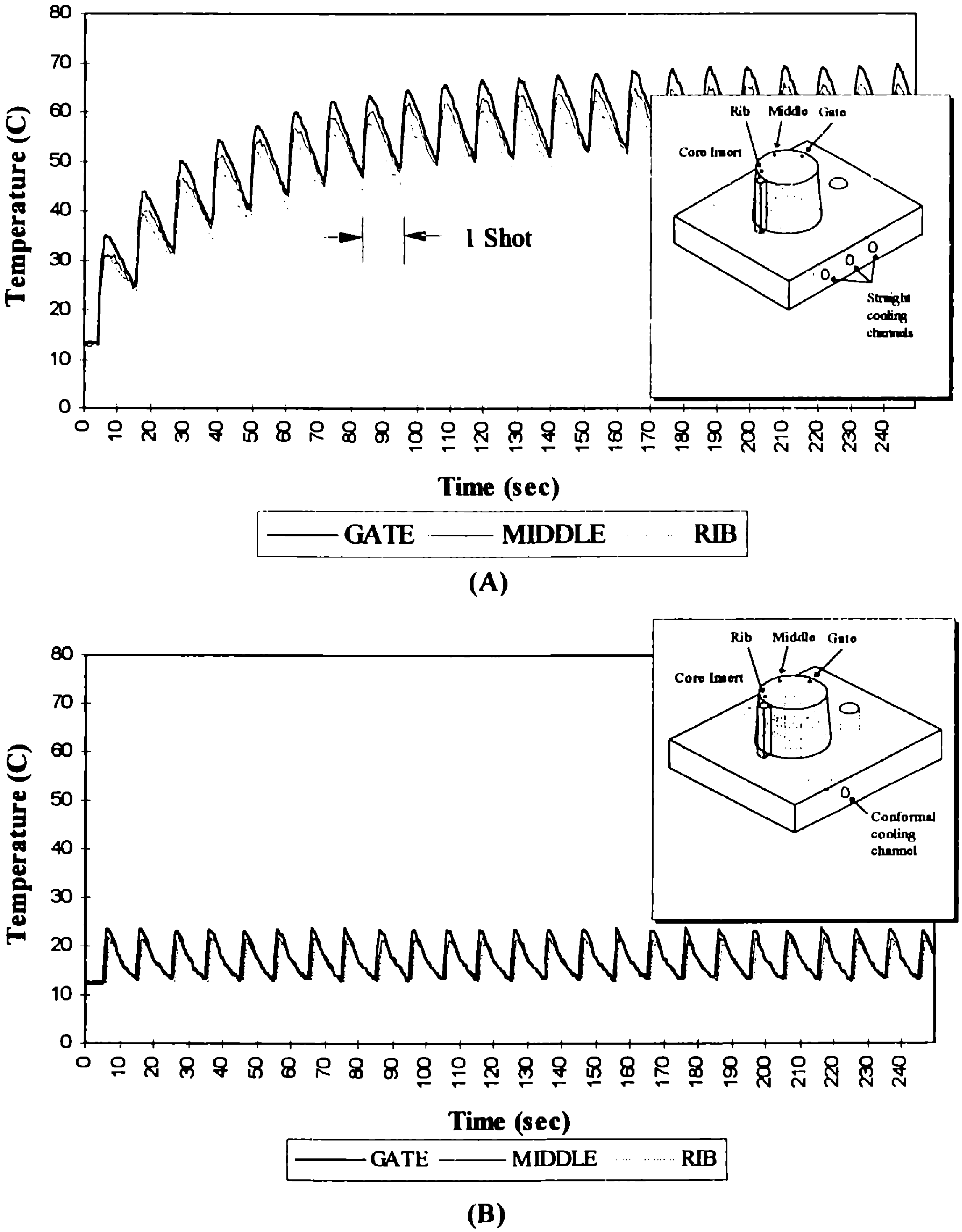

Figure 8.1: Core insert surface temperature - coolant temperature ≈ 11 °C, (A) 303 stainless steel inserts with straight channels (B) 3D Printed inserts with conformal cooling channels.

The conformal passages produced with the 3DP process provide the ability to accurately control the temperature of the molding cavity throughout the process cycle. Surface temperature measurements demonstrated that the inserts with conformal cooling channels exhibited a more uniform surface temperature than the inserts machined with straight channels.

A summary of observations obtained from the mold surface temperature results follows:

- A significant upward drift in surface temperature (approximately 30 °C) is observed using the stainless steel inserts with straight channels.

- No noticeable drift in surface temperature is observed throughout the injection molding run using the 3D Printed inserts with conformal channels.

- The magnitude of the mold surface temperature swing during the injection molding cycle is approximately 4 - 5 °C smaller for the inserts with conformal channels than the inserts with straight channels.

- The difference in temperature along the perimeter of the core or cavity molding surface (difference in temperature at gate end vs. rib end) is lower in magnitude when using the inserts with conformal channels than when using the inserts with straight channels. This difference in magnitude is measured at the beginning of the cooling stage in the molding cycle. At the beginning of the cooling stage of the cycle there is a 4 °C variation in temperature along the mold surface of the 3D Printed core insert. This compares to a 7 °C temperature variation for the core insert machined with conventional straight channels.

The insert pair was designed to mold a cylindrical polystyrene test "ring". A thin gap was designed in the ring to exhibit distortion in the form of the ring gap widening or closing. The gap width remains constant from the first shot to the next throughout the injection molding run when using the 3D Printed inserts with conformal cooling channels. The gap width drifts to a lower steady state dimension during the injection molding run when using the stainless steel inserts with straight channels. The drift in dimension is consistent with that of the mold surface temperature. This indicates the strong relationship between mold surface temperature and part distortion and warpage.

8.3 Future Research

Injection molds must act as uniformly functioning heat exchangers in order to operate economically and produce high quality parts. To produce high-grade moldings at low costs, the heat provided by the plastic material to the mold must be removed from the mold surface as fast and as uniformly as possible. Thus, the cooling system design has a definite impact on the economics of the process and the quality of the manufactured parts. [Menges, 1993] 3D Printing allows for the creation of complicated conformal cooling channel designs. A method of determining the optimal conformal channel design is necessary. A simulation of the cooling system in a mold early in the design stage is essential. The use of finite element software is a viable solution.

The simple two-dimensional finite difference simulation described in this thesis was surprisingly useful for modeling cooling in the 3D Printed core and cavity inserts. The relative simplicity of the part geometry explains the conformity between the simulation and the experimental results. Molds with complicated cavity geometries require heat transfer simulation of an injection molding process in three dimensions.

Several finite element software packages designed to analyze heat transfer in injection molding tooling are available on the market today. An interesting avenue of future research would be the development of an injection molding finite element software package specifically geared towards analyzing mold surface temperature and heat transfer in 3D Printed molds with conformal cooling channels. This tool could potentially aid in cooling system design in molds having complicated cavity geometries making full use of the benefits that conformal channels provide.

Creation of bronze infiltrant filled channels using the 3DP process opens a new avenue of exploration for the mold designer. This technology allows for regions of increased thermal diffusivity and thus heat transfer in mold geometries difficult to cool or where it may be structurally unwise to place a cooling channel. Potential certainly lies in the combination of this technology with conformal cooling channels and other new mold cooling technologies.

References

Acrysol WS - 24 Colloidal Dispersion, Rohm and Haas, Philadelphia, PA. Company literature.

Anval, 316L stainless steel powder -140 / +325 mesh, Rutherford, NJ. Company literature.

Brancazio, David, "Development of a Robust Electrostatically Deflecting Printhead for Three Dimensional Printing," M.I.T. Masters Thesis, May 1991.

Burke and Newcome, "Essential Parameters for Molding Modified PET Resins: An Assessment of Their Influence on Molded Part Quality," presented at the Society of Plastics Engineers 40th Annual Technical Conference, San Francisco, 1982.

Fritch, L.W., "How Mold Temperature and Other Molding Variables Affect ABA Falling Part and Izod Impact," presented at the Society of Plastics Engineers 40th Annual Technical Conference, San Francisco, 1982.

Gordon, M.J., Total Quality Process Control for Injection Molding, Hanser Publishers, New York, NY, 1993.

Grodzinsky, Mark, "Development of a Powder Removal System for Three Dimensionally Printed Parts," M.I.T. Bachelors Thesis, May, 1994.

Han, C.D. and C.A. Villamizar, "Measurement of Pressure and Stress Birefringence Patterns During the Mold Filling and Cooling Operation," presented at the Society of Plastics Engineers 35th Annual Technical Conference, Montreal, 1977.

Incropera, F., Fundamentals of Heat and Mass Transfer, John Wiley & Sons, New York, NY, 1990.

Kim, Byung Hoon, "Low Thermal Inertia Injection Molding," M.I.T. PHD Thesis, July, 1983.

Lienhard, J.H., A Heat Transfer Textbook, Prentice-Hall, Inc., Englewood Cliffs, NJ, 1987.

Lyman, T., Metals Handbook Eighth Edition, Powder Metallurgy, vol. 1, American Society for Metals, Metals Park, OH, 1961.

Menges, G., How to Make Injection Molds, Hanser Publishers, Munich, 1993.

Michaels, Steven, "Production of Metal Parts Using the Three Dimensional Printing Process," M.I.T. Masters Thesis, November, 1993.

Rubin, Irvin, Injection Molding Theory and Practice, John Wiley & Sons, New York, NY, 1972.

Sachs, E., Cima, M., Williams, P., Brancazio, D., and Cornie, J., "Three Dimensional Printing: Rapid Tooling and Prototypes Directly From a CAD Model", Accepted for publication in the Journal of Engineering for Industry.

School, Rudy, "Markets for Thermoplastic Elastomers," presented at the Society of Plastics Engineers 52nd Annual Technical Conference, San Francisco, 1994.

Semenchenko, V.K., Surface Phenomena in Metals and Alloys, Pergamon Press LTD., Oxford, 1962.

Shutts, Christopher, "Development of a Reliable Electrostatic Multijet Printhead for Three Dimensional Printing," M.I.T. Masters Thesis, May, 1995.

Thomas, L. C., Fundamentals of Heat Transfer, Prentice-Hall, Inc., Englewood Cliffs, NJ, 1980.

A. Powder Coatings

A salt coating is applied to the 316L stainless steel powder before printing. The salt coating acts as a coagulating agent for the binder and helps prevent ballistic ejection of powder in the powder bed. This appendix describes the procedure used to coat the powder.

[The following powder coating procedure courtesy Steven Michaels, 1993]

<u>Sodium Carbonate Coated Powder</u>

When developing the procedure for coating powder with sodium carbonate, mass quantities were used instead of molar quantities for easier formulation. First, an aqueous solution of sodium carbonate was prepared in the following proportions:

1.25g sodium carbonate
100g deionized water

The powder to be coated was placed in a beaker. The above solution was then added to the powder in the proportion of 1.0g of solution per 100g of powder. Additional deionized water was added and stirred in to make a thin paste. This served to evenly distribute the salt.

The above materials are stirred and then placed in an oven at 150°C until the powder is very dry. The hot powder should be stirred about once every hour while drying to prevent salt migration to the top of the powder pile.

Once the dry powder is cooled, it should be sieved to the finest degree possible, depending on the original size distribution of the powder. Large clumps should be ground and resieved and then added to the remaining powder. This procedure will deposit 0.0125g of sodium carbonate per 100g of powder.

B. Shrinkage of Cavity and Core Inserts

The following is a schematic and a table describing the shrinkage of the 3D Printed cavity insert.

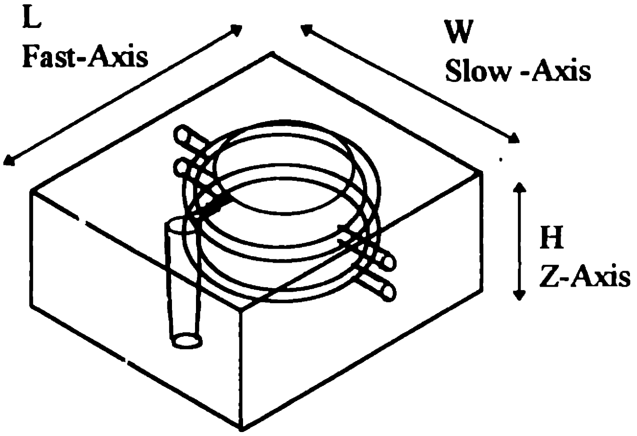

Figure B.1: Schematic of cavity insert.

Dimensions (inches)	L	W	H
Green	3.73	3.20	1.39
Sintered	3.56	3.08	1.33
Infiltrated	3.59	3.10	1.34
Target (CAD Dimensions)	3.63	3.13	1.38
Dimensional Change (%)			
Green -> Sintered	-4.40	-3.63	-4.17
Sintered -> Infiltrated	0.73	0.62	0.68
Overall	-3.70	-3.03	-3.53

Table B.1: Shrinkage values for cavity insert.

The following is a schematic and a table describing the shrinkage of the 3D Printed core insert.

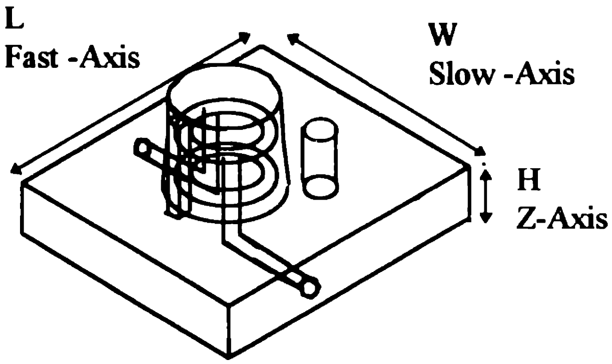

Figure B.2: Schematic of core insert.

Dimensions (inches)	L	W	H
Green	3.64	3.13	0.63
Sintered	3.57	3.10	0.62
Infiltrated	3.58	3.10	0.62
Target (CAD Dimensions)	3.63	3.13	0.63
Dimensional Change (%)			
Green -> Sintered	-1.76	-1.12	-1.60
Sintered -> Infiltrated	0.22	0.23	0.49
Overall	-1.54	-0.89	-1.12

Table B.2: Shrinkage values for core insert.

C. Machine Drawings of Inserts

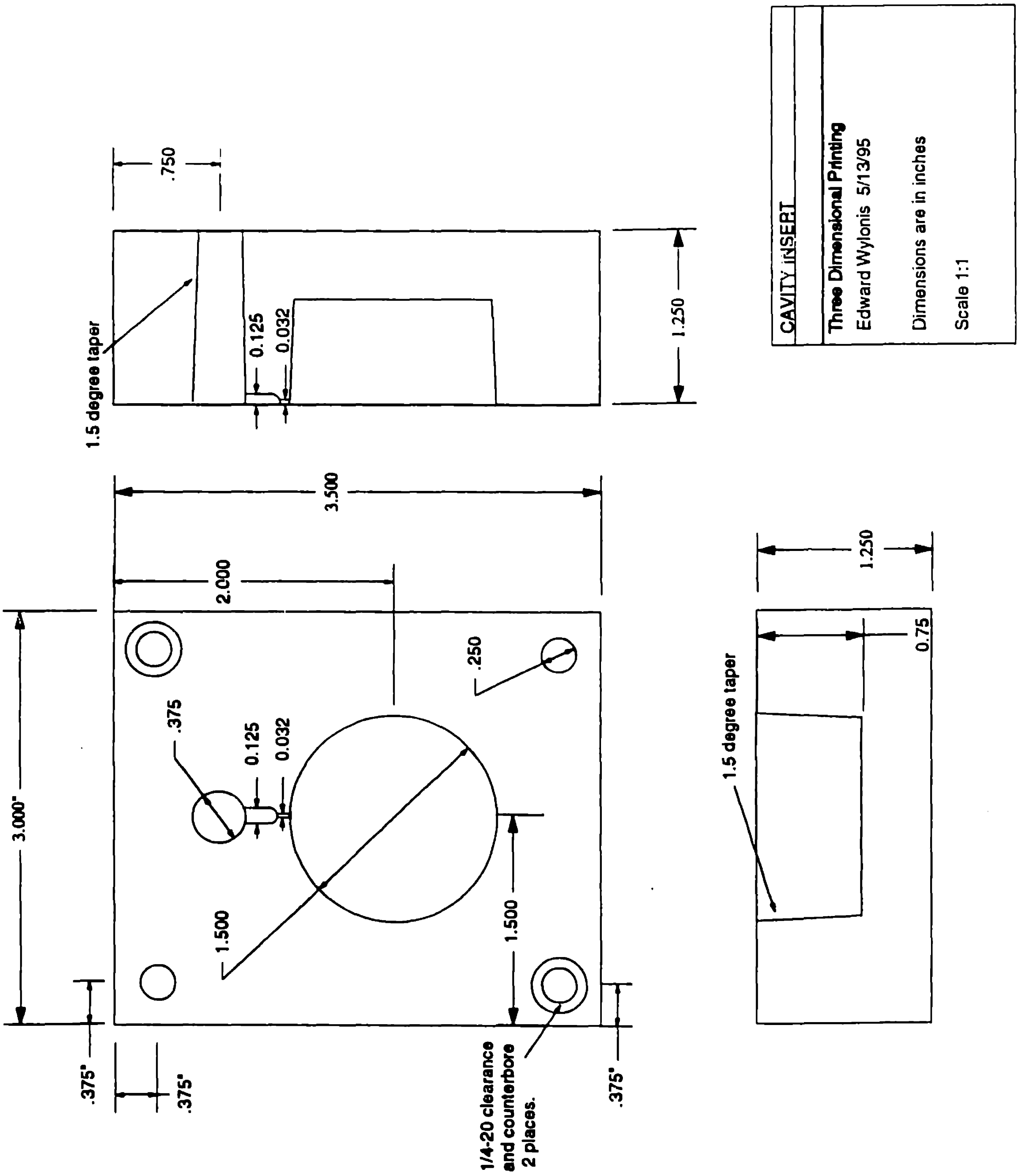

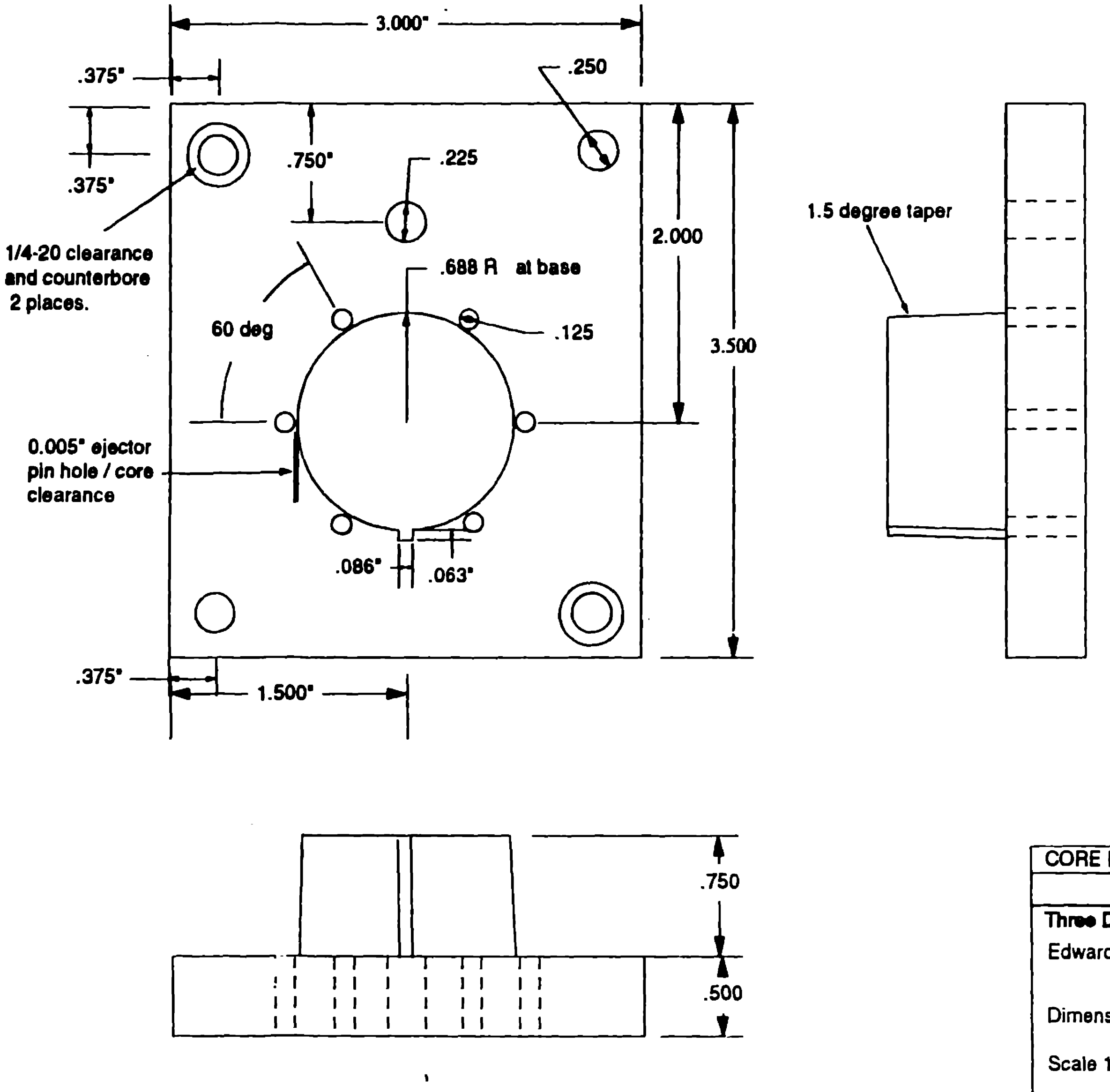

CORE INSERT

Three Dimensional Printing
Edward Wylonis 5/13/95

Dimensions are in inches

Scale 1:1

D. Machine Drawings of Straight and Conformal Channels

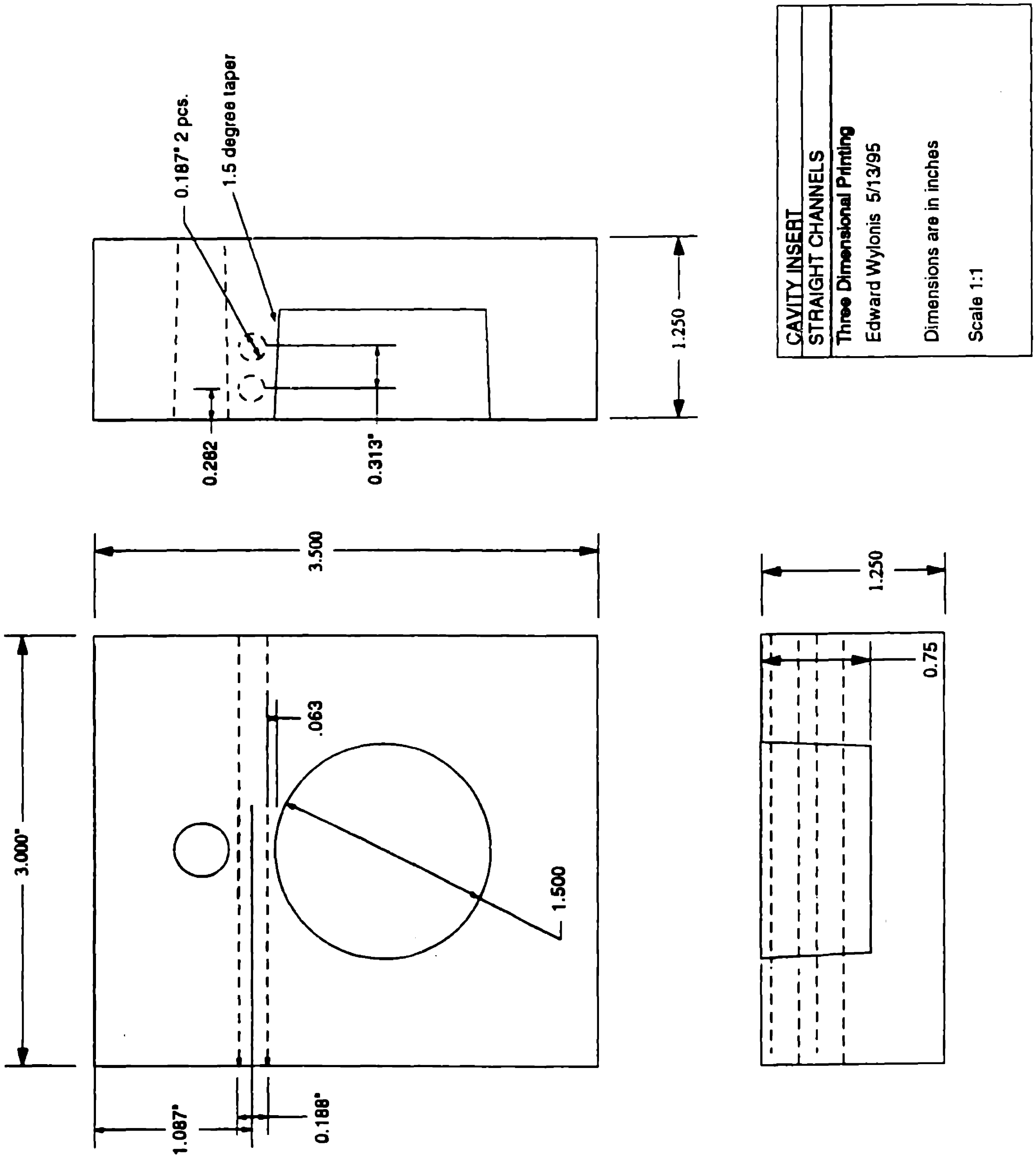

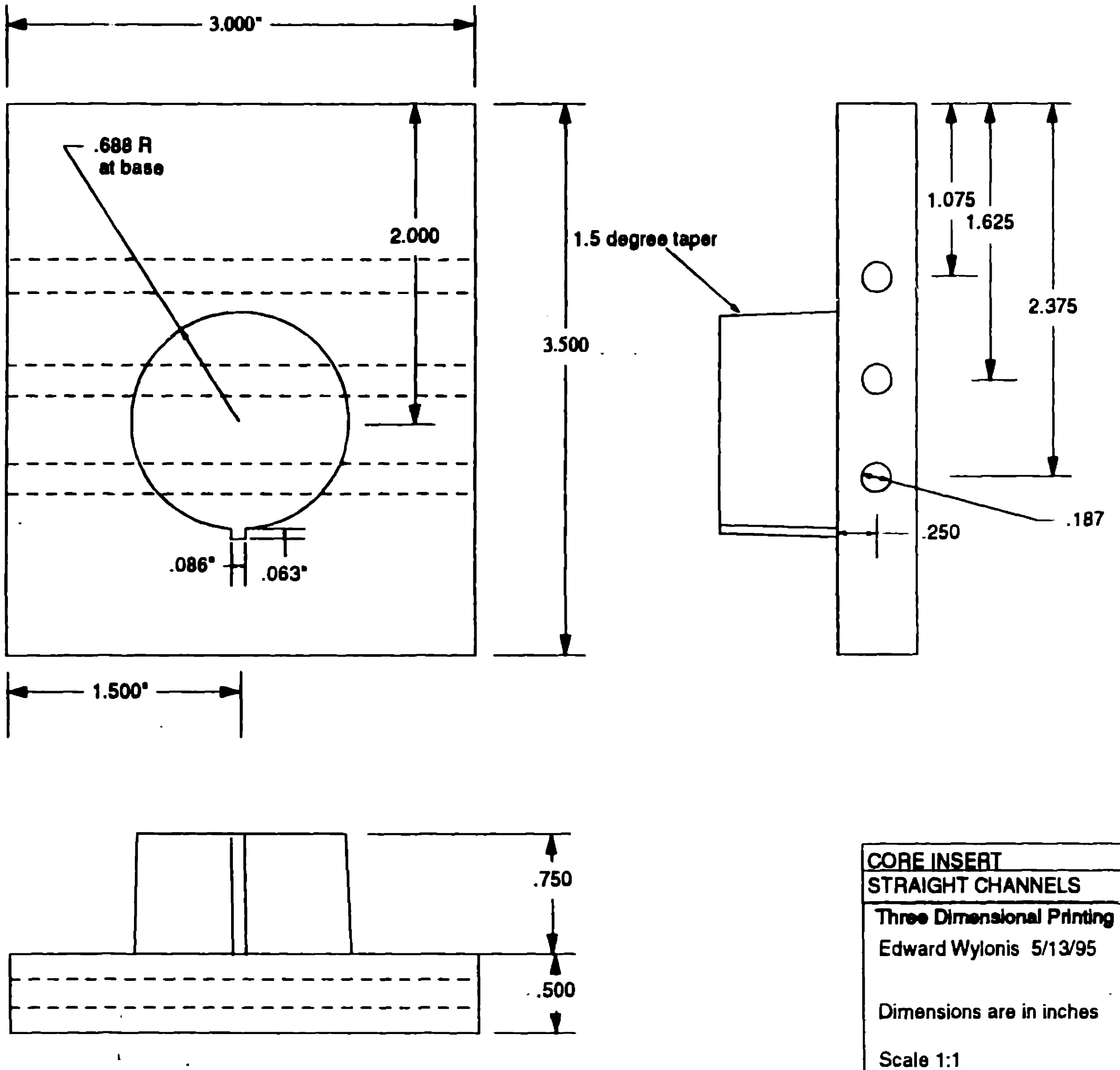

CORE INSERT
STRAIGHT CHANNELS

Three Dimensional Printing
Edward Wylonis 5/13/95

Dimensions are in inches

Scale 1:1

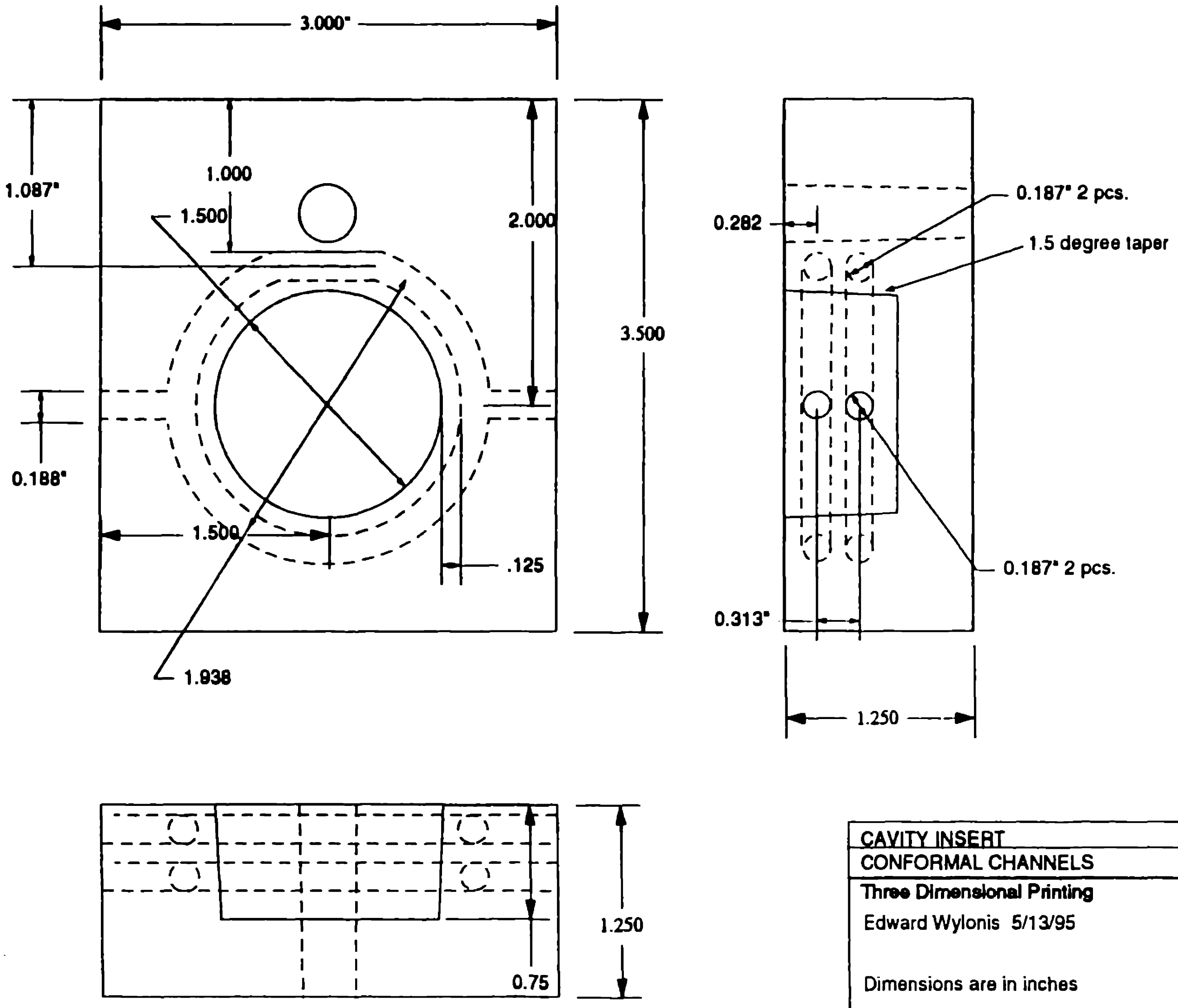

CAVITY INSERT
CONFORMAL CHANNELS
Three Dimensional Printing
Edward Wylonis 5/13/95

Dimensions are in inches

Scale 1:1

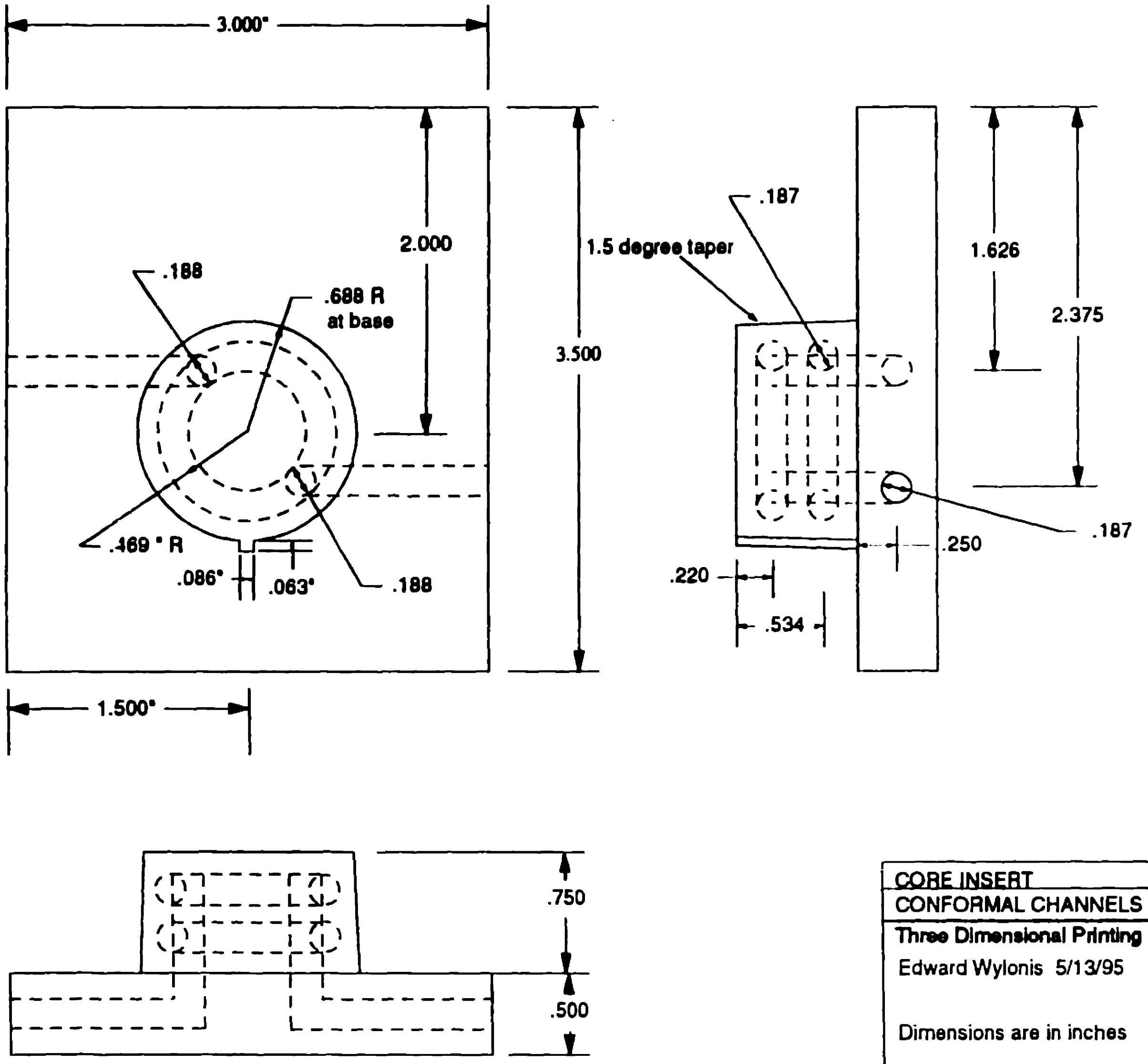

CORE INSERT
CONFORMAL CHANNELS
Three Dimensional Printing
Edward Wylonis 5/13/95

Dimensions are in inches

Scale 1:1

E. Determination of Thermal Conductivity of 3D Printed Material, Bronze Infiltrated 316L Stainless Steel

The value of the thermal conductivity for 3D Printed 316L stainless steel infiltrated with 10% tin - bronze was experimentally determined. This value was ascertained for use in analytical and finite element studies of the thermal control in injection molds created using the Three Dimensional Printing manufacturing process.

A simple test to determine the thermal conductivity of 3D Printed material was performed. A block of cast and sintered 316L powder infiltrated with bronze was machined into a rectangular test bar. Figure E.1 shows a schematic of the test bar sample used to perform the thermal conductivity experiment.

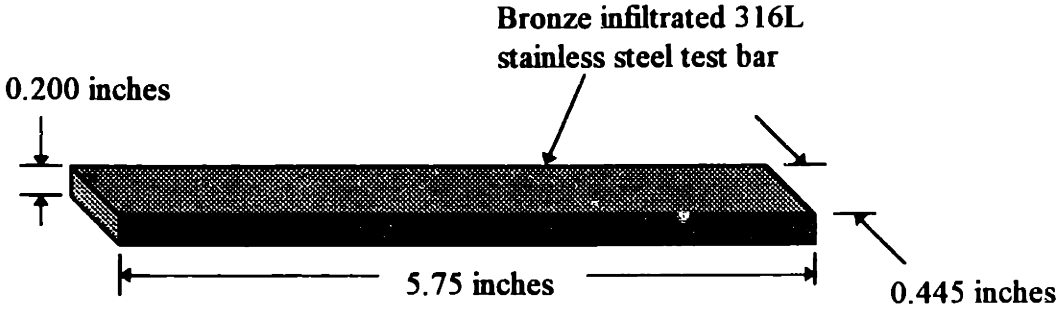

Figure E.1: Bronze infiltrated 316L stainless steel test bar.

The Fourier heat equation in one dimension was employed:

$$Q = K \cdot A \cdot \frac{dT}{dx}, \tag{E.1}$$

where Q is the rate of heat flow, K is the thermal conductivity, A is the cross sectional area and dT/dx is the temperature gradient along the direction of heat flow.

A specific heat rate was applied at one end of the bronze infiltrated stainless steel test bar using a small strip heater. The other end was subjected to a constant temperature (12 °C) water bath. Thermistors were placed a distance, dx (0.021m) apart on the surface of the test bar with highly thermally conductive paste. Insulation was placed around the bar and the thermistors. The setup was allowed to achieve steady state over a period of a couple hours. The temperature of the bar and the insulation was periodically examined to determine when the system had reached steady state. Figure E.2 depicts a schematic of the experimental setup.

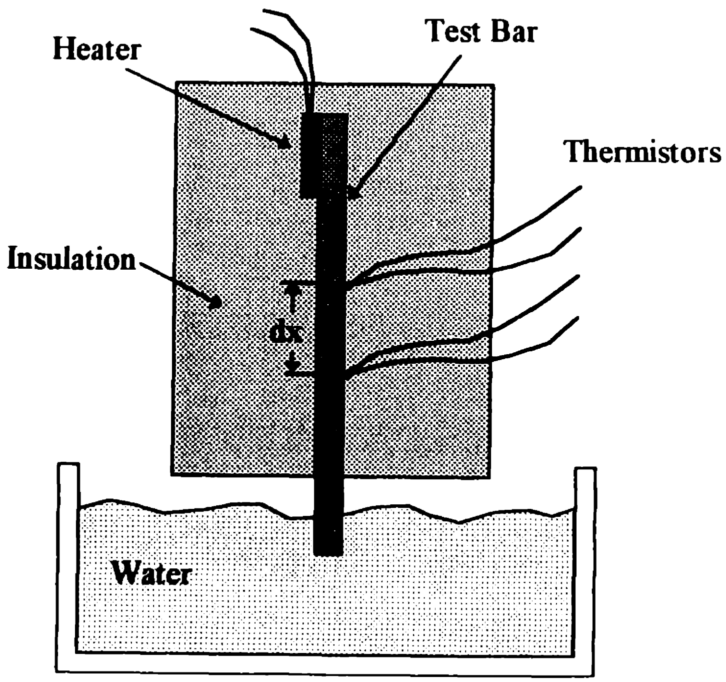

Figure E.2: Experimental setup.

By fixing the voltage across the electric heater, and measuring its resistance at the operating temperature, the applied heat rate was determined. Measuring the temperature across the distance, dx, a value for the thermal conductivity, K may be found. The temperature of the top insulating surface was a few degrees hotter than the ambient air. This heat loss must be quantified and considered in determining the thermal conductivity using equation E.1.

The lateral and bottom insulating surfaces did not reach a temperature higher than ambient air. Therefore, no heat loss through these surfaces was considered. The Nusselt number for a horizontal flat plate in natural convection was used to determine the heat loss through the top insulating surface. The Nusselt number is the dimensionless thermal gradient at the solid/fluid interface. The following correlations for the Nusselt number were used [Incropera, 1990]

$$\begin{aligned} Nu_l &= 0.54 \cdot Ra_l^{1/4};\ 10^4 < Ra_l < 10^7 \\ Nu_l &= 0.15 \cdot Ra_l^{1/3};\ 10^7 < Ra_l < 10^{11} \\ Nu_l &= \frac{h \cdot L}{K} \end{aligned} \qquad \text{E.2}$$

where Ra is the Rayleigh number, which is the ratio of buoyancy to thermal and momentum diffusivities. It can be defined as the product of the Grashof number (ratio of buoyancy to viscous forces) and the Prandtl number (ratio of momentum to thermal diffusivities):

$$Ra_l = Gr_l \cdot \Pr = \frac{g \cdot \beta \cdot (T_s - T_\infty) \cdot L^3}{\nu \cdot \alpha} \qquad \text{E.3}$$

where g is the value of gravity, β is the coefficient of volumetric thermal expansion, T_s is the temperature at the surface, T_∞ is the ambient temperature, L is a characteristic length, ν is the air kinematic viscosity , and α is the air thermal diffusivity. At this point, the film temperature is defined as:

$$T_{film} = \frac{T_s + T_\infty}{2}, \qquad \text{E.4}$$

This is the temperature at which the air thermophysical properties are evaluated.

The following is a representative sample of data and an example of the steps followed to obtain the thermal conductivity value. The voltage applied across the electric heater was 35 V and the measured resistance of the heater at steady state was 1372 Ohms. The temperatures at the two thermistors were 35.9 and 25.5 °C. The ambient air temperature was 22 °C, and the measured surface temperature at the top surface was 24 °C.

Power dissipation in a resistor is calculated as $P = V^2 / R = 0.893$ W. The film temperature is 23 °C. The thermal conductivity, thermal diffusivity, kinematic viscosity and the coefficient of volumetric thermal expansion of air are evaluated at this film temperature. ($\nu = 15.89 \text{x} 10\text{-}6$ m2/s, $\alpha = 22.5 \text{x} 10\text{-}6$ m2/s, $\beta = 1 / 296$ K, $K = 26.3 \text{x} 10\text{-}3$ W/ m K) [Incropera, 1990]

The Rayleigh number (equation E.3) is determined to be 1210. Thus, the first correlation for the Nusselt number given in equation E.2 is used to evaluate the Nusselt number.

The Nusselt number is determined to be 3.183 and the convection coefficient h is 4.476 W / m^2K. The heat loss may then be calculated as $Q_{lost} = h\ A\ \Delta T = 0.05$ W. Using the Fourier equation:

$$K = \frac{(Q_{heater} - Q_{loss}) \cdot dx}{A \cdot \Delta T} \qquad \text{E.5}$$

The thermal conductivity is determined to be 28 W/mK.

A control sample with known thermal conductivity was subjected to the experimental test to determine the accuracy of the procedure. A 302 stainless steel bar of identical dimensions and thermal conductivity of 19.8 W/mK was used. An experimental value of 21.4 W/mK was obtained following the described procedure. An 8 %

discrepancy between the known and experimentally determined values for the thermal conductivity was observed. The 8% over - estimate of the thermal conductivity of the 302 stainless steel was accounted for in the final assessment of the experimentally determined value of the thermal conductivity of the bronze infiltrated stainless steel material. This evaluation yields a final thermal conductivity value of 26 W/mK.

F. Finite Difference Nodal Equations

The nodal equations employed in the finite difference simulation are presented. Figure F.1 depicts the plastic melt and steel block divided into finite subvolumes. Representative nodes requiring unique nodal equations are numbered.

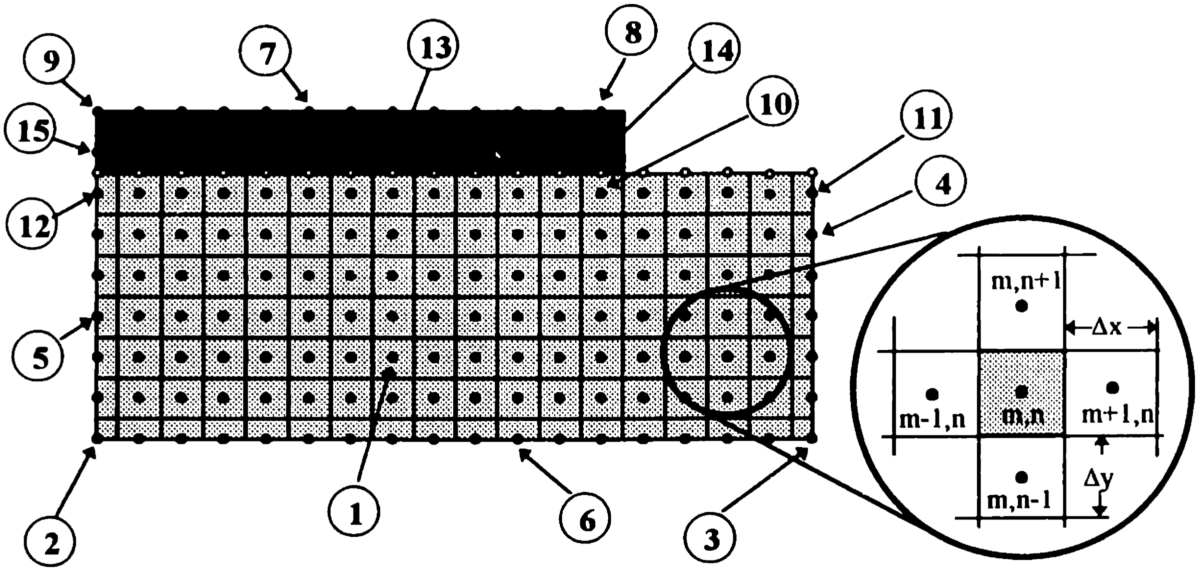

Figure F.1: Nodes of finite difference grid.

The following equations explicitly express the temperature at time (τ+1)Δt in terms of the temperature at the earlier instant of time τΔt for each unique node:

<u>Nodes of steel block</u>

(excluding molding surface nodes) ($\Delta x_{steel} = \Delta y_{steel} = \Delta x$)

$$(1)\quad T_{m,n}^{\tau+1} = \frac{\alpha_{steel}\Delta t}{\Delta x^2}\left(T_{m+1,n}^{\tau} + T_{m-1,n}^{\tau} + T_{m,n+1}^{\tau} + T_{m,n-1}^{\tau}\right) + \left(1 - \frac{4\alpha_{steel}\Delta t}{\Delta x^2}\right)T_{m,n}^{\tau}$$

$$(2)\qquad T_{M,N}^{\tau+1} = \frac{2\alpha_{steel}\Delta t}{\Delta x^2}\left(T_{M+1,N}^{\tau} + T_{M,N+1}^{\tau} - 2T_{M,N}^{\tau}\right) + T_{M,N}^{\tau}$$

(3) $$T_{M,N}^{r+1} = \frac{2\alpha_{steel}\Delta t}{\Delta x^2}\left(T_{M-1,N}^{r} + T_{M,N+1}^{r} - 2T_{M,N}^{r}\right) + T_{M,N}^{r}$$

(4) $$T_{M,n}^{r+1} = \frac{\alpha_{steel}\Delta t}{\Delta x^2}\left(2T_{M-1,n}^{r} + T_{M,n+1}^{r} + T_{M,n-1}^{r}\right) + \left(1 - \frac{4\alpha_{steel}\Delta t}{\Delta x^2}\right)T_{M,n}^{r}$$

(5) $$T_{M,n}^{r+1} = \frac{\alpha_{steel}\Delta t}{\Delta x^2}\left(2T_{M+1,n}^{r} + T_{M,n+1}^{r} + T_{M,n-1}^{r}\right) + \left(1 - \frac{4\alpha_{steel}\Delta t}{\Delta x^2}\right)T_{M,n}^{r}$$

(6) $$T_{m,N}^{r+1} = \frac{\alpha_{steel}\Delta t}{\Delta x^2}\left(2T_{m,N+1}^{r} + T_{m+1,N}^{r} + T_{m-1,N}^{r}\right) + \left(1 - \frac{4\alpha_{steel}\Delta t}{\Delta x^2}\right)T_{m,N}^{r}$$

Nodes of plastic melt

(excluding molding surface nodes) ($\Delta y_{plastic} \neq \Delta x_{plastic}$)

(7) $$T_{m,N}^{r+1} = \Delta t\left(\left(\frac{\alpha_{plastic}\left(T_{m+1,N}^{r} - T_{m,N}^{r}\right)}{\Delta x_{plastic}^{2}}\right) + \left(\frac{\alpha_{plastic}\left(T_{m-1,N}^{r} - T_{m,N}^{r}\right)}{\Delta x_{plastic}^{2}}\right) + \left(\frac{2\alpha_{plastic}\left(T_{m,N-1}^{r} - T_{m,N}^{r}\right)}{\Delta y_{plastic}^{2}}\right)\right) + T_{m,N}^{r}$$

(8) $$T_{M,N}^{r+1} = \Delta t\left(\left(\frac{2\alpha_{plastic}\left(T_{M-1,N}^{r} - T_{M,N}^{r}\right)}{\Delta x_{plastic}^{2}}\right) + \left(\frac{2\alpha_{plastic}\left(T_{M,N-1}^{r} - T_{M,N}^{r}\right)}{\Delta y_{plastic}^{2}}\right)\right) + T_{M,N}^{r}$$

(9) $$T_{M,N}^{r+1} = \Delta t\left(\left(\frac{2\alpha_{plastic}\left(T_{M+1,N}^{r} - T_{M,N}^{r}\right)}{\Delta x_{plastic}^{2}}\right) + \left(\frac{2\alpha_{plastic}\left(T_{M,N-1}^{r} - T_{M,N}^{r}\right)}{\Delta y_{plastic}^{2}}\right)\right) + T_{M,N}^{r}$$

Molding surface nodes of steel block

(Open stage - No plastic in contact - ($\Delta x_{steel} = \Delta y_{steel} = \Delta x$))

$$(10)\quad T^{r+1}_{m,N} = \frac{\alpha_{steel}\Delta t}{\Delta x^2}\left(T^r_{m+1,N} + T^r_{m-1,N} + 2T^r_{m,N-1}\right) + \left(1 - \frac{4\alpha_{steel}\Delta t}{\Delta x^2}\right)T^r_{m,N}$$

$$(11)\quad T^{r+1}_{M,N} = \frac{2\alpha_{steel}\Delta t}{\Delta x^2}\left(T^r_{M-1,N} + T^r_{M,N-1} - 2T^r_{M,N}\right) + T^r_{M,N}$$

$$(12)\quad T^{r+1}_{M,N} = \frac{2\alpha_{steel}\Delta t}{\Delta x^2}\left(T^r_{M+1,N} + T^r_{M,N-1} - 2T^r_{M,N}\right) + T^r_{M,N}$$

(Filling and cooling stages - Plastic in contact - ($\Delta x_{steel} = \Delta x_{plastic} = \Delta x$, $\Delta y_{steel} \neq \Delta y_{plastic}$))

$$(10)\quad T^{r+1}_{m,n} = \Delta t\left(\left(\frac{\alpha_{steel}\left(T^r_{m+1,n} - T^r_{m,n}\right)}{\Delta x^2}\right) + \left(\frac{\alpha_{steel}\left(T^r_{m-1,n} - T^r_{m,n}\right)}{\Delta x^2}\right)\right.$$
$$\left. + \left(\frac{\alpha_{plastic}\left(T^r_{m,n+1} - T^r_s\right)}{\left(\frac{\Delta y_{plastic}}{2}\right)^2}\right) + \left(\frac{\alpha_{steel}\left(T^r_s - T^r_{m,n}\right)}{\left(\frac{\Delta y_{steel}}{2}\right)^2}\right) + \left(\frac{\alpha_{steel}\left(T^r_{m,n-1} - T^r_{m,n}\right)}{\Delta y_{steel}^2}\right)\right) + T^r_{m,n}$$

$$(11)\quad T^{r+1}_{M,n} = \Delta t\left(\left(\frac{2\alpha_{steel}\left(T^r_{M-1,n} - T^r_{M,n}\right)}{\Delta x^2}\right)\right.$$
$$\left. + \left(\frac{\alpha_{plastic}\left(T^r_{M,n+1} - T^r_s\right)}{\left(\frac{\Delta y_{plastic}}{2}\right)^2}\right) + \left(\frac{\alpha_{steel}\left(T^r_s - T^r_{M,n}\right)}{\left(\frac{\Delta y_{steel}}{2}\right)^2}\right) + \left(\frac{\alpha_{steel}\left(T^r_{M,n-1} - T^r_{M,n}\right)}{\Delta y_{steel}^2}\right)\right) + T^r_{M,n}$$

$$(12)\quad T_{M,n}^{\tau+1} = \Delta t\left(\left(\frac{2\alpha_{steel}\left(T_{M+1,n}^{\tau} - T_{M,n}^{\tau}\right)}{\Delta x^{2}}\right)\right.$$

$$\left.+\left(\frac{\alpha_{plastic}\left(T_{M,n+1}^{\tau} - T_{s}^{\tau}\right)}{\left(\frac{\Delta y_{plastic}}{2}\right)^{2}}\right)+\left(\frac{\alpha_{steel}\left(T_{s}^{\tau} - T_{M,n}^{\tau}\right)}{\left(\frac{\Delta y_{steel}}{2}\right)^{2}}\right)+\left(\frac{\alpha_{steel}\left(T_{M,n-1}^{\tau} - T_{M,n}^{\tau}\right)}{\Delta y_{steel}^{\;2}}\right)\right)+T_{M,n}^{\tau}$$

For (10), (11) and (12) in contact with plastic melt:

$$T_{s}^{\tau} = \frac{\Delta y_{steel}k_{plastic}T_{m,n+1\,(plastic)}^{\tau} + \Delta y_{plastic}k_{steel}T_{m,n\,(steel)}^{\tau}}{\Delta y_{steel}k_{plastic} + \Delta y_{plastic}k_{steel}}$$

<u>Molding surface nodes of plastic melt:</u>

(Filling and Cooling Stages)

($\Delta x_{steel} = \Delta x_{plastic} = \Delta x,\ \Delta y_{steel} \neq \Delta y_{plastic}$)

$$(13)\quad T_{m,n}^{\tau+1} = \Delta t\left(\left(\frac{\alpha_{plastic}\left(T_{m+1,n}^{\tau} - T_{m,n}^{\tau}\right)}{\Delta x^{2}}\right)+\left(\frac{\alpha_{plastic}\left(T_{m-1,n}^{\tau} - T_{m,n}^{\tau}\right)}{\Delta x^{2}}\right)\right.$$

$$\left.+\left(\frac{\alpha_{steel}\left(T_{m,n-1}^{\tau} - T_{s}^{\tau}\right)}{\left(\frac{\Delta y_{steel}}{2}\right)^{2}}\right)+\left(\frac{\alpha_{plastic}\left(T_{s}^{\tau} - T_{m,n}^{\tau}\right)}{\left(\frac{\Delta y_{plastic}}{2}\right)^{2}}\right)+\left(\frac{\alpha_{plastic}\left(T_{m,n+1}^{\tau} - T_{m,n}^{\tau}\right)}{\Delta y_{plastic}^{\;2}}\right)\right)+T_{m,n}^{\tau}$$

$$(14)\quad T_{M,n}^{\tau+1} = \Delta t\left(\left(\frac{\alpha_{plastic}\left(T_{M-1,n}^{\tau} - T_{M,n}^{\tau}\right)}{\Delta x^{2}}\right) + \left(\frac{\alpha_{steel}\left(T_{M,n-1}^{\tau} - T_{s}^{\tau}\right)}{\left(\frac{\Delta y_{steel}}{2}\right)^{2}}\right) + \left(\frac{\alpha_{plastic}\left(T_{s}^{\tau} - T_{M,n}^{\tau}\right)}{\left(\frac{\Delta y_{plastic}}{2}\right)^{2}}\right) + \left(\frac{\alpha_{plastic}\left(T_{M,n+1}^{\tau} - T_{M,n}^{\tau}\right)}{\Delta y_{plastic}^{2}}\right)\right) + T_{M,n}^{\tau}$$

$$(15)\quad T_{M,n}^{\tau+1} = \Delta t\left(\left(\frac{\alpha_{plastic}\left(T_{M+1,n}^{\tau} - T_{M,n}^{\tau}\right)}{\Delta x^{2}}\right) + \left(\frac{\alpha_{steel}\left(T_{M,n-1}^{\tau} - T_{s}^{\tau}\right)}{\left(\frac{\Delta y_{steel}}{2}\right)^{2}}\right) + \left(\frac{\alpha_{plastic}\left(T_{s}^{\tau} - T_{M,n}^{\tau}\right)}{\left(\frac{\Delta y_{plastic}}{2}\right)^{2}}\right) + \left(\frac{\alpha_{plastic}\left(T_{M,n+1}^{\tau} - T_{M,n}^{\tau}\right)}{\Delta y_{plastic}^{2}}\right)\right) + T_{M,n}^{\tau}$$

For (13), (14) and (15) :

$$T_{s}^{\tau} = \frac{\Delta y_{plastic} k_{steel} T_{m,n-1\,(steel)}^{\tau} + \Delta y_{steel} k_{plastic} T_{m,n\,(plastic)}^{\tau}}{\Delta y_{plastic} k_{steel} + \Delta y_{steel} k_{plastic}}$$